

**Association between flow instability and rupture of
intracranial cerebral aneurysms**

脳動脈瘤に関わる流動不安定性と破裂の相関

July 2016

LIJIAN XU

Graduate School of Engineering

CHIBA UNIVERSITY

(千葉大学審査学位論文)

**Association between flow instability and rupture of
intracranial cerebral aneurysms**

脳動脈瘤に関わる流動不安定性と破裂の相関

July 2016

LIJIAN XU

Graduate School of Engineering

CHIBA UNIVERSITY

Abstract

Patients with intracranial cerebral aneurysms present a great challenge to the neurosurgeons and engineers, particularly when presenting with subarachnoid hemorrhage (SAH). Misjudgment of SAH may lead to disastrous postoperative rebleeding from the untreated but true-ruptured lesion. Recent studies report that flow instability may correlate with the rupture mechanism of cerebral aneurysms. However, how flow instability contribute to aneurysm rupture remains to be elucidated. In this study, we developed computational fluid dynamic (CFD) models of patient-specific cerebral aneurysms to investigate whether flow instability correlated with aneurysm rupture. The present thesis consists of two main parts. Part I is concerned with the effects of inflow waveform and elastic wall on the flow instabilities and hemodynamic factors of cerebral aneurysms. Part II is dedicated to exploring the possible associations between flow instabilities and aneurysm rupture through systematic simulations and analyses.

The work of part I starts with developing high-resolution CFD simulations to investigate the effects of inlet flow rate waveforms and elastic wall on the flow instabilities. The occurrence of flow instabilities mainly depend on the geometry and inflow waveform. Significant flow instabilities have been observed in many experiments and CFD simulations in vivo and vitro. We established more than eight patient-specific CFD models of aneurysms with Fourier series analysis and found obvious association between harmonics and flow instabilities: the low-frequency harmonics in inlet flow rates very likely induce and dominate WSS fluctuations associated with cerebral aneurysms, in particular during the decelerating phase at late systole, which corresponds with a steeper global and local pressure gradient. This suggests that cerebral aneurysm hemodynamics could be of some robustness, dependent mainly on the primary low-frequency harmonics initiated by heart contraction but insensitive to the unpredictable high-frequency perturbations in the inflow waveforms. Besides the inflow waveform effects, we further studied the elastic effects on the flow instability and hemodynamic factors in a cerebral aneurysm. Both CFD simulations and

particle imaging velocimetry (PIV) experiments have been carried out for more accurate prediction and validation. The simulation results of the rigid and elastic model prove to be qualitatively similar to respective PIV results. In addition, the results of simulation and PIV both show that the averaged WSS in the flexible wall model is about 10% smaller than that in the rigid wall model. The results of patient-specific aneurysms confirmed that the elasticity of the aneurysm wall could dampen the change of WSS, which suggests that the rigid model may proliferate the risk of aneurysm rupture.

The work of part II investigates the potential association between flow instability and aneurysm rupture on groups of rupture-unruptured aneurysms with high-resolution CFD simulations. Firstly, CFD simulations were performed on two matched-pairs of ruptured-unruptured cerebral aneurysms. We found highly disturbed states of the blood flows in the ruptured aneurysms of the two patients, which are characterized by remarked velocity and WSS fluctuations at late systole during flow deceleration. The ruptured aneurysms exhibit much more significant temporal intra-cycle WSS fluctuations than the unruptured aneurysms of the same patient. Moreover, cycle-to-cycle fluctuations are observed in the ruptured aneurysms when the flow turns to decelerate. Secondly, CFD simulations of thirty-five cerebral aneurysms located at the internal carotid artery (ICA) were performed to investigate whether fluctuation kinetic energy quantifying the flow instability might be an effective indicator to evaluate rupture risk of aneurysms, and whether pressure loss could be associated to such flow instability. The results demonstrated that eight ruptured aneurysms present significantly higher ratio of low WSS area and lower pressure loss coefficient, whereas two ruptured aneurysms manifests remarked flow fluctuations and higher pressure losses compared to unruptured aneurysms. Our results suggest that flow instability could be associated with aneurysm rupture, inherently correlated with the high pressure loss for cerebral aneurysms.

Acknowledgement

I would like to thank many people who have encouraged and supported me during my PhD studies. First and foremost, I am sincerely grateful to my advisor, Professor Liu for taking me as his doctor student. He directed me to the wonderful world of biomechanics and gave me the chance to study on this very interesting field. He devoted a lot of time to guide me in the research, which deeply affected my style of thinking and working. I would not be able to finish the PhD studies without his valuable guidance in research and financial support.

Special thanks to my advisor Professor Gu in Shanghai Jiaotong university who supervised my master and favored my study in Chiba university.

I want to thank the defense committee members, Professor Tsubota, Professor Haneishi and Professor Tanaka for the precious suggestions.

I appreciate Professor Yamaguchi, Dr. Saito and other colleagues from Aomori Hospital. They involved in the technical discussion, supplied the data, gave the clinical suggestions and reviewed the manuscripts.

My lab mates brought me so much help and happiness. I would like to thank Dr. Ikeda, Dr. Zhang and Dr. Fujiwara. I wish you could realize the dreams in future.

I want to thank my parents, whose understanding kept me going during the tough times. I love you more than words could express.

At last, I want to acknowledge supports from the Japanese Government Scholarship and Chiba University.

Table of Contents

1 Introduction	1
1.1 Importance of learning the mechanism of aneurysm rupture	1
1.2 Limitations of the current methods	1
1.3 Objective of this study.....	2
2 Flow instabilities in cerebral aneurysms	4
2.1 Introduction	4
2.2 Basic physical principles.....	4
2.3 Image-based patient-specific simulation of cerebral aneurysms	5
2.3.1 Geometric modeling.....	5
2.3.2 Boundary conditions	6
2.3.3 Numerical Solution	7
2.3.4 Post-processing.....	7
2.3.5 Mesh sensitivity analysis.....	8
2.4 Results	8
2.4.1 Flow description.....	8
2.4.2 Inlet waveform effects on flow fluctuations.....	9
2.5 Discussion	10
2.6 Conclusion.....	13
3 Waveform Dependence of flow instabilities in cerebral aneurysms	25
3.1 Introduction	25
3.2 Methods.....	26
3.2.1 Image-based anatomic modeling.....	26
3.2.2 Boundary conditions	26
3.2.3 Computational fluid dynamic modelling.....	27
3.3 Results	27
3.3.1 Geometry and inflow waveform effects on WSS fluctuations	27
3.3.2 Geometry and inflow waveform effects on the hemodynamic factors.....	28
3.3.3 Harmonic effects on pressure variations and WSS fluctuations.....	28
3.4 Discussion	29
3.5 Conclusions	32
4 Elastic wall influence on the hemodynamic factors in cerebral aneurysms.....	42
4.1 Introduction	42

4.2. Material and methods	43
4.2.1 Imaging and patient data	43
4.2.2 CFD simulation	43
4.2.3 Mesh independence tests	44
4.2.4 Validation tests	44
4.3 Results	44
4.4 Discussion	46
4.4.1 Summary	46
4.4.2 Limitations	46
4.5 Conclusion.....	48
5 Exploring potential associations between flow instability and rupture in patients with matched-pairs of ruptured-unruptured intracranial aneurysms	54
5.1 Introduction	54
5.2 Methods.....	55
5.2.1 Geometry and mesh.....	55
5.2.2 Boundary conditions	56
5.2.3 Computational fluid dynamic modeling.....	56
5.2.4 Shear forces and kinetic energy.....	57
5.3 Results	58
5.3.1 Flow patterns and hemodynamic factors	58
5.3.2 Flow fluctuations and fluctuating kinetic energy (FKE).....	58
5.3.3 Geometry and inflow waveform effects on flow fluctuations	59
5.4 Discussion	60
5.5 Conclusions	63
6 Statistical analysis of flow instability related to aneurysm rupture on thirty-five aneurysms at the internal carotid artery	75
6.1 Introduction	75
6.2 Methods.....	76
6.2.1 Image-based anatomic modeling.....	76
6.2.2 Boundary conditions	76
6.2.3 Computational fluid dynamics modelling	77
6.2.4 Data analysis	78
6.3 Results.....	79
6.3.1 Flow stabilities	79
6.3.2 Statistics results	80
6.4 Discussion.....	80

6.5 Conclusion	82
7 Conclusion remarks and future works	91
Bibliography	93

List of Figures

- Figure 2-1.** Computer model and mesh systems of a cerebral aneurysm (a) and relationship between element numbers of the meshes and mean WSS (b). RA1, RA2, LA2 denote the proximal part of the right anterior cerebral, the distal part of the right anterior cerebral and the distal left anterior cerebral arteries. The mean WSS show less changes with meshes increasing from 1 million up to 5 million. 14
- Figure 2-2.** The solid line represents the inflow rate waveform obtained by a 1D model of the cardiovascular system, which is approximated by Fourier series decomposition (the dotted line) with eight harmonics. The green point means the peak systole. 15
- Figure 2-3.** Distributions of hemodynamic factors at peak systole from two viewing angles. Upper: Anterior view, Lower: Posterior View. (a) Streamlines: The blood flowed into the aneurysm from the parent vessel directly, leading to a large vortex inside. (b) Pressures: When a region with adverse pressure gradient appeared in the aneurysm, the fluid particles could not penetrate too far into the region of increased pressure. (c) WSS: The low WSS at the large bleb was surrounded by a region of locally elevated WSS. (d) OSI: Most of the aneurysm was exposed to low OSI, while the large bleb was subjected to higher OSI. 16
- Figure 2-4.** Time-varying velocities in a complete heart beat at five points in the cerebral aneurysm model. No velocity fluctuation was observed in Point 1 and 2, but the time trace of Point 3, 4 and 5 clearly demonstrates the existence of velocity fluctuation in the aneurysm. 17
- Figure 2-5.** WSS fluctuations and respective PSD at the aneurysm. From top to bottom: observation points in the OSI image (a), time traces of the magnitude of WSS (b) and respective PSD (c) at two points. The WSS fluctuations were obvious in the deceleration phase at the aneurysm. The frequency spectrum of Point 6 showed some peaks ranged 23-105Hz, while Point 7 had higher temporal fluctuation and strong peaks around 25-190Hz. 18
- Figure 2-6.** WSS fluctuations and respective PSD at the aneurysm with different average Reynolds numbers. From top to bottom: time traces of the magnitude of WSS (a) and respective PSD (b) at two points. 19

- Figure 2-7.** Fourier series decomposition of the inlet waveform. The coefficients for Fourier series expansions were indicated. The inlet waveform is represented by a dominant power located at about 1.1Hz in frequency domain, corresponding to 66 beats/min, with several harmonic peaks in the higher frequency ranges (2.2, 3.3, 4.4, 5.5, 6.6, 7.7 and 8.8 Hz). The constant term (1.86 ml/s) from the Fourier series expansion was the average flow rate of the original inlet wave. 20
- Figure 2-8.** WSS fluctuations and respective PSD at the aneurysm with the inlet of the first harmonic. From top to bottom: time traces of the magnitude of WSS (a), respective PSD (b) and enlarged view of PSD (c) at two points. Significant WSS fluctuations were already present around 128Hz with the inlet of first harmonic ($N=1$). 21
- Figure 2-9.** (a) The inflow waveform and Fourier series synthesis of the harmonics ($N=1,2,3$). (b) The maximum dominant frequencies observed at the aneurysm with the inlet of summated harmonics ($N=1-8$). Higher peaks at 144, 149, 166, 175, 183, 185 and 187Hz with the inlet of the first 2, 3, 4 5, 6, 7 and 8 harmonics ($N=2-8$). 22
- Figure 2-10.** WSS fluctuations of the aneurysm with the inlet of the first, second, fourth and eighth harmonic ($n=1, 2, 4, 8$). The WSS fluctuations were obvious during the deceleration phase with the inlet of first harmonic ($n=1$), but became less significant with inlet of the higher harmonic ($n=2-8$). 23
- Figure 2-11.** Pressure drop over the cerebral aneurysm versus the harmonics at peak systole. Clearly, the first harmonic leads to steeper pressure drop, which enhances the flow instability. 24
- Figure 3-1.** Eight patient-specific terminal cerebral aneurysm models used in simulations (ruptured aneurysms A-D, unruptured aneurysms E-H). 33
- Figure 3-2.** The inlet velocity waveforms in a cardiac cycle at three average velocities: 0.4m/s, green line; 0.5m/s, red line; 0.6m/s, black line. 34
- Figure 3-3.** Visualization of WSS fluctuations associated with cerebral aneurysm models A-C. Two snapshots of instantaneous WSSs (a) and OSIs (b) at peak systole; time-varying WSSs (c) at two feature points (point a, black line; point b, red line) with the inflow rate of the first harmonic ($n=1$). The average Reynolds numbers of models A-C are 203, 257 and 208 respectively. 35
- Figure 3-4.** Visualization of streamline and pressure distribution at different inlet velocities: 0.4, 0.5 and 0.6 m/s with a heart rate of 66 bpm (ruptured aneurysms A&B, unruptured aneurysms E&F). Two snapshots of

instantaneous streamlines (a) and pressures (b) at peak systole; centerline analysis for peak systolic (PK1, PK2, PK3) and averaged (AV1, AV2, AV3) velocities (c) and pressures (d), which show the pressure differences compared with that at inlet.

36

Figure 3-5. Visualization of WSS (a), pressure (b) and pressure gradient distribution (c) at peak systole for three different heart rates: 66, 100 and 125bpm with an average velocity of 0.5m/s (cerebral aneurysm model H, $Re=291$). The arrow shows the local high-pressure island identical to some stagnation point inside the aneurysm, which leads to an adverse local pressure gradient against the flow into the aneurysm.

37

Figure 3-6. Centerline analysis for pressure drop versus harmonics inside the cerebral aneurysm models A-C at peak systole. Obviously, the low-frequency harmonic ($n=1$) leads to steeper pressure drops compared to the high-frequency harmonics ($n=2-8$).

38

Figure 3-7. Visualization of WSS (a), pressure (b) and pressure gradient distribution (c) at peak systole with the inflow rate of the three harmonics ($n=1, 2$ and 4) (cerebral aneurysm model B, $Re=257$).

39

Figure 3-8. Visualization of WSS fluctuations associated with cerebral aneurysm models A-C. Instantaneous OSIs (a) at peak systole and time-varying WSSs at feature points (b)-(c) with the inflow rate of the four harmonics ($n=1$, 64black line; $n=2$, red line; $n=4$, green line; $n=8$, blue line). For models A-C, the average Reynolds numbers are 203, 257 and 208 respectively. WSS fluctuations are evident during the deceleration phase at the first harmonic ($n=1$), but dramatically become invisible at the higher harmonics ($n=2-8$).

40

Figure 4-1 Boundary conditions the model. Pressure (Red line) and flow rate (Green line) waveforms at the inlet and outlet are based on our multi-scale modeling of the human cardiovascular system, and then adjusted to fit the mean value measured by MRI.

49

Figure 4-2. (a) The Velocity vector and in the middle plane within the aneurysm ($Re_m=435$, $\alpha=4.0$). Top row shows CFD and PIV results at peak systole, and bottom row shows CFD and PIV results at peak diastolic. (b) Wall shear stress along wall inside elastic aneurysm. The red and black lines indicate the CFD and PIV results respectively.

50

Figure 4-3. Visualization of WSS of the Rigid (Upper) and Elastic model (Lower) in Cerebral Aneurysm Model A. (a) instantaneous Streamline. (b) Pressure. (c) WSS. (d) Deformation at peak systole, respectively.

51

Figure 4-4. Visualization of WSS of the Rigid (Upper) and Elastic model (Lower) in Cerebral Aneurysm Model B. (a) instantaneous Streamline. (b) Pressure. (c) WSS. (d) Deformation at peak systole, respectively. 52

Figure 4-5. WSS vectors of the Rigid (Upper) and Elastic (Lower) model at four phases: (a)peak systole, (b)middle deceleration phase, (c)the second peak systole, (d)diastole. 53

Figure 5-1. Four patient-specific cerebral aneurysm models in two pairs employed in simulations (unruptured aneurysms A1&B1, ruptured aneurysms A2&B2). Black and red arrows point to single inlets and multiple outlets, respectively. 64

Figure 5-2. The inlet flow rate waveform over a cardiac cycle of model A with a mean velocity of 0.31 m/s. 65

Figure 5-3. Visualized flow patterns at peak systole in two cutting planes for each aneurysm model. The black circles correspond to vortex cores and the red arrows point to the recirculating zones with slow flow due to flow separation at the blebs. Models A2&B2 present a more complex feature of unstable flow patterns with multiple vortices compared to models A1&B1. 66

Figure 5-4. Distributions of pressures (a), WSSs (b) and OSIs (c) at peak systole for model A (upper) and model B (lower). Red and black arrows point to the recirculating zones at the blebs and the stagnation regions, respectively. There obviously exists a featured distribution of high OSIs and low WSSs at the blebs, with high pressures and WSS gradients in the two ruptured aneurysms A2&B2. 67

Figure 5-5. Velocity distributions aligning with centerlines at peak systole (a-b) and time-varying velocities at feature points for model A (c-d). Complicated velocity profiles with multiple inflection points are found at the bends of ICA siphon (Points 1-5). Velocity fluctuations are observed in the upstream arteries and aneurysm sacs. Note that the rupture aneurysm A2 (Points 11-12) exhibit more significant velocity fluctuations than unruptured aneurysm A1 (Points 7-8). The peak Reynolds numbers of the upstream parent arteries of aneurysms are calculated to be 627 and 554 for models A1 and A2, respectively. 68

Figure 5-6. Velocity distributions aligning with centerlines at peak systole (a-b) and time-varying velocities at feature points for model B (c-d). Few inflection points and no velocity fluctuations are observed at the ICA siphon. The flow is very likely laminar and stable at ICA but does exhibit significant fluctuations in the aneurysms. Note that the rupture aneurysm B2 (Points

11-12) exhibit more significant velocity fluctuations than unruptured aneurysm B1 (Points 7-8). The peak Reynolds numbers of the upstream parent arteries of aneurysms are calculated to be 718 and 746 for models B1 and B2, respectively.

69

Figure 5-7. Time-varying WSSs at six feature points inside the cerebral aneurysms of model A (a) and model B (b). The ruptured aneurysms A2&B2 apparently present more significant WSS fluctuations rather with the unruptured aneurysms A1&B1 do.

70

Figure 5-8. WSS distributions (a) and velocity fields in two cutting planes (b) at an instant of deceleration phase for three consecutive heart cycles (model B2). Black arrows point to the cycle-to-cycle differences of the flow patterns and WSS distributions during the deceleration phase.

71

Figure 5-9. Average fluctuating kinetic energy (FKE) in model A2 (a) and model B2 (b). The blue solid and dashed lines show the time varying velocities at feature points inside aneurysms and inlets as reference, respectively. An obvious FKE peak is observed when flow turns to decelerate at late systole.

72

Figure 5-10. Time-varying velocities at feature points for model A (a) and model B (b). A constant inflow velocity of 0.31 m/s with no fluctuating component was imposed at the inlets to identify the possibility of flow instabilities independent of pulsatile flow dynamics. The rupture aneurysms A2&B2 (Points 11-12) exhibit consistent velocity fluctuations whereas unruptured aneurysms A1&B1 (Points 7-8) converge to a single solution.

73

Figure 6-1. The typical patient-specific internal carotid aneurysm model. The aneurysm area is marked as red color.

83

Figure 6-2. Aspect ratio distributions of aneurysms.

84

Figure 6-3. Normalized WSS distribution for ruptured-unruptured ICA aneurysms. The top two rows are ruptured aneurysms. There are no significant differences between aneurysms. Both low and high WSS are observed at the aneurysm.

85

Figure 6-4. Volumetric rendering of energy fluctuations (FKE) of thirty-five ruptured-unruptured aneurysms. The cases without fluctuations appear empty.

86

Figure 6-5. Time-varying velocities at feature points inside the ruptured (a) and unruptured (b) cerebral aneurysm models.

87

Figure 6-6. Scatter plot of Normalized Mean WSS (NMWSS) versus pressure loss coefficient (PLC) for ruptured and unruptured ICA aneurysms. The red solid open squares represent the unstable and stable ruptured aneurysms, whereas the black solid open circles represent the unstable and stable unruptured

aneurysms, respectively.

List of Tables

Table 3-1. Demographic, morphologic parameters and flow characteristics of the eight cerebral aneurysms.	41
Table 5-1. Demographic, morphologic parameters and flow characteristics of the four cerebral aneurysms.	74
Table 6-1. Statistics of the demographic, morphologic parameters for the thirty-five cerebral aneurysms	89
Table 6-2. Statistics of the hemodynamic variables for the thirty-five cerebral aneurysms	90

1 Introduction

1.1 Importance of learning the mechanism of aneurysm rupture

Cerebral aneurysms are cerebrovascular protruding sacs that develop in specific cerebrovascular sites. The most severe consequence of cerebral aneurysms is the rupture and intracranial hemorrhage (SAH), causing a high mortality rate. For SAH patients with multiple aneurysms, it is very important for the medical team to determine which one causes SAH. The misdiagnosis of SAH is quite dangerous since the untreated but ruptured aneurysms might rupture again soon (Suarez et al. 2008). For patients without SAH, it is also vital to predict which aneurysms are prone to rupture and whether an operation is necessary or not. However, prediction of rupture risk in patients with cerebral aneurysms remains challenging for clinicians and engineers. Hemodynamic factors, particularly Wall Shear Stress (WSS), play a key role in understanding the onset, progress and rupture of aneurysms. Understanding the mechanisms associated with these events could contribute to making a more accurate assessment of rupture risk, and therefore avoid unnecessary surgical operations. The WSS-relative hemodynamic factors have been presented as key indicator for the rupture risk. Xiang et al. (2011) analyzed 38 ruptured and 81 unruptured aneurysms using CFD-based models and proposed that low WSS and high OSI correlated with aneurysm rupture. Cebal et al. (2011) studied 210 aneurysms with CFD models and correlated the maximum WSS with aneurysm rupture. Qian et al. (2011) performed CFD on four ruptured and 26 unruptured cerebral aneurysms and proposed that greater energy loss occurs when flow passes through ruptured aneurysms, compared with unruptured aneurysms. Takao et al. (2012) studied 50 sidewall aneurysms at internal carotid posterior communicating artery and 50 terminal aneurysms at middle cerebral artery with CFD and demonstrated that pressure loss coefficient may be associated with aneurysm rupture. Recently, flow instability-related studies in vessels and aneurysms have been carried out experimentally and numerically and may also correlate to aneurysm rupture (Ferguson, 1970; Steiger and Rulen, 1986; Valen-Stenstad et al., 2011; Varble et al., 2016; Yagi et al., 2013). The rupture mechanism of cerebral aneurysm is still not completely defined.

1.2 Limitations of the current methods

The blood flow in the aneurysm is always assumed to be laminar flow in the most numerical simulations since the Reynolds number in the artery is much lower than the threshold of $Re =$

2300, where turbulence occurs in a straight pipe flow. However, the lowest Reynolds number where high-frequency flow instabilities occurred was reported less than 500, which is the Reynolds number for major cerebral arteries. The flow pattern is more likely a disturbed laminar flow. Most numerical simulation in this field assumed laminar flow and employed stabilized schemes with dissipation to ensure convergence at coarser resolution. The simplified assumption of treating the hemodynamics as a fully laminar flow needs to be carefully considered especially in the impingement of the aneurysm. Here high spatial and temporal resolutions were performed to ensure the Navier-Stokes equations properly resolved with little dissipation. As a result, the small structures involved in transitional flow could be captured with high-resolution schemes.

Another important simplified assumption is that rigid wall is always assumed in current studies. Most researches focus on the CFD simulations assuming the rigid geometry from medical images neglecting the elastic wall of the vascular geometry. Intra-operations have already observed that the cerebral aneurysms are exposed to different wall structures and wall elasticity could provide essential information towards understanding the elastic influence of blood fluid on the vascular wall. The wall elasticity could to some extent influence the flow patterns in the cerebral aneurysm models, which also need to be carefully considered.

The blood flow is usually assumed as the Newtonian fluid in cerebral aneurysm researches since the Reynolds numbers in cerebral arteries are relatively low compared to the large arteries. This simplified assumption may to some extent influence the simulation results especially in the high disturbed flows in the highly stenosis arteries and aneurysms with complex geometries. The non-Newtonian effects on the flow patterns need to be carefully considered especially in the complex flows.

1.3 Objective of this study

In the present study, we developed CFD models of anatomically realistic cerebral aneurysms to investigate whether the flow instability correlated with aneurysm rupture. Firstly, high-resolution temporal and spatial CFD studies were performed on a patient-specific aneurysm model to observe the highly disturbed flow with high-frequency flow instability. Secondly, we studied the effects of the inlet flow rate waveforms on the flow instabilities and hemodynamic factors. More than eight patient-specific CFD models of cerebral aneurysms were established to investigate the association between inflow waveform and flow fluctuations in cerebral aneurysms. To further understand the wall elasticity effects on the flow instability and hemodynamics, we used fluid-structure interaction method to investigate the hemodynamics in two cerebral aneurysms. Thirdly, systematic simulations and analyses were performed to explore the possible associations between flow instabilities and aneurysm rupture. CFD

simulations were performed on two matched-pairs of ruptured-unruptured cerebral aneurysms. Thirty-five cerebral aneurysms located at the internal carotid artery were finally employed to investigate whether the flow instability could be an effective indicator to evaluate the rupture risk of aneurysms.

2 Flow instabilities in cerebral aneurysms

2.1 Introduction

Flow fluctuations have been shown to exist in aneurysms in vitro and in vivo. [Ferguson \(1970\)](#) recorded the presence of bruits with a phonocatheter from the aneurysm sacs of 10 of 17 cerebral aneurysms during operation. The author postulated the disturbed blood flow in the aneurysm might cause the degeneration of the aneurysm wall leading to continuing progression and eventual rupture. [Steiger and Rulen \(1986\)](#) then found distinct flow instabilities on cerebral saccular aneurysms in six of 12 patients with intra-operative Doppler recordings. The low frequency vibrations ranged between 5 and 20 Hz. Concomitant studies on glass model aneurysms also showed the presence of flow instabilities in terminal aneurysms at a Reynolds number of 300. [Yagi et al. \(2013\)](#) carried out an experimental PIV study in a patient-specific cerebral aneurysm model and observed the low- and high-frequency flow instabilities co-existed in the cerebral aneurysm model. They implied that the simplified assumption of taking the aneurysmal hemodynamics as a laminar flow needs to be attentively considered. [Baek et al. \(2010\)](#) investigated the flow instabilities and oscillatory behavior of WSS on three patient-specific saccular aneurysms at the internal carotid artery with high-resolution numerical simulations. They proposed that the oscillatory behavior of WSS vectors might play a key role in the initiation of a cerebral aneurysm. [Ford and Piomelli \(2012\)](#) studied the flow instabilities using four idealized basilar aneurysm models and four patient specific terminal basilar tip aneurysms. The authors postulated that the disturbed flow existed in the basilar aneurysms and the high-frequency oscillations of WSS vectors might greatly affect the life cycle of the aneurysm. [Valen-Sendstad et al. \(2011\)](#) studied the high-frequency flow instability in a middle cerebral aneurysm with direct numerical simulations. The authors proposed the observed non-laminar behavior was due to the large volume of the aneurysm dome and breakdown of the inflow jet.

2.2 Basic physical principles

Blood flow must obey the basic physical principles of mass, momentum, and energy. The fluid is regarded as a continuum. According to the mass conservation principle, we get

$$\frac{\partial \rho}{\partial t} + \frac{\partial(\rho u_i)}{\partial x_i} = 0 \quad (2-1)$$

As an incompressible fluid, the density ρ is a constant value and the above equation becomes

$$\frac{\partial u_i}{\partial x_i} = 0 \quad (2-2)$$

Newton's second law states that *Force = Mass \times acceleration*

-pressure gradient + shear stress + gravitational force = Mass \times (transient acceleration + convective acceleration)

$$\rho \left(\frac{\partial u_i}{\partial t} + u_j \frac{\partial u_i}{\partial x_j} \right) = -\frac{\partial p}{\partial x_i} + \mu \frac{\partial^2 u_i}{\partial x_j^2} \quad (2-3)$$

Now we get the governing equations for the fluid are unsteady and incompressible three-dimensional Navier-Stokes equations.

$$\frac{\partial u}{\partial x} + \frac{\partial v}{\partial y} + \frac{\partial w}{\partial z} = 0 \quad (2-4)$$

$$\frac{\partial u}{\partial t} + u \frac{\partial u}{\partial x} + v \frac{\partial u}{\partial y} + w \frac{\partial u}{\partial z} = -\frac{1}{\rho} \frac{\partial P}{\partial x} + \frac{\mu}{\rho} \nabla^2 u \quad (2-5)$$

$$\frac{\partial v}{\partial t} + u \frac{\partial v}{\partial x} + v \frac{\partial v}{\partial y} + w \frac{\partial v}{\partial z} = -\frac{1}{\rho} \frac{\partial P}{\partial y} + \frac{\mu}{\rho} \nabla^2 v \quad (2-6)$$

$$\frac{\partial w}{\partial t} + u \frac{\partial w}{\partial x} + v \frac{\partial w}{\partial y} + w \frac{\partial w}{\partial z} = -\frac{1}{\rho} \frac{\partial P}{\partial z} + \frac{\mu}{\rho} \nabla^2 w \quad (2-7)$$

The three components of transient acceleration are

$$\frac{\partial u}{\partial t}, \frac{\partial v}{\partial t}, \frac{\partial w}{\partial t}$$

The three components of convective acceleration are

$$u \frac{\partial u}{\partial x} + v \frac{\partial u}{\partial y} + w \frac{\partial u}{\partial z}, \quad u \frac{\partial v}{\partial x} + v \frac{\partial v}{\partial y} + w \frac{\partial v}{\partial z}, \quad u \frac{\partial w}{\partial x} + v \frac{\partial w}{\partial y} + w \frac{\partial w}{\partial z}$$

2.3 Image-based patient-specific simulation of cerebral aneurysms

2.3.1 Geometric modeling

The target cerebral aneurysm is placed in the anterior communicating artery (AcoA), which

usually receives blood from the anterior cerebral arteries. Three-dimensional images of the arteries and aneurysms were picked up by three-dimensional digital subtraction angiography (3D-DSA). DSA images with a slice thickness of 0.2mm were used for geometry reconstruction. As depicted in [Figure 2-1](#) the cerebral aneurysm models consist of the right anterior cerebral artery and the distal left anterior cerebral artery. We included the important vessel geometry features and created realistic inlet and outlet condition because they influence on the hemodynamics and flow instabilities in cerebral aneurysms. The patient-specific vessels that are not extended pipes are included as much as possible so to reduce the effects of boundary artifacts. Sensitivity examinations were also carried out to guarantee the simulated results are independent of the lengths of inlet and outlet. The vessel geometries were firstly extracted semi-automatically using 3DSlicer, which enables a user to employ region growing and manual segmentation. The reconstructed model was then smoothened by blurring and morphological operations. After that, the smoothened model was imported into ANSYS ICEM 15.0 for meshing. Unstructured grids were produced with the minimum element size of 0.015 mm and maximum number of 5 million finite volume elements.

2.3.2 Boundary conditions

At the inlet, physiologically realistic boundary condition was obtained from the human cardiovascular system ([Liang et al. 2009](#)). At inlet a flow rate with a peak of 3.5 ml/s was imposed as shown in [Figure 2-2](#). At two outlets the traction-free boundary conditions were imposed. The flow division through the two outlets was according to the time-averaged flow rate. Based on the computed inlet flow rate, the blood density (1025 kg/m^3) and kinematic viscosity ($3.5 \times 10^{-6} \text{ m}^2/\text{s}$), the diameter-based Reynolds numbers are calculated to be approximately 250 and 485, with the mean and peak flow rate-based flow velocities as representative flow velocity, respectively, whereas the Womersley number is 2.07. On vessel surfaces we assumed that the compliant wall-induced deformation is negligible and hereby employed the non-slip conditions.

The inlet flow rate waveform was defined by using a 1D model of the human cardiovascular system, which is capable to represent the realistic inlet flow rates in the cerebral arteries. The 1D-based waveform was further decomposed into Fourier series with a constant term and 8 harmonics. Although patient-specific flow rates were unavailable in this study, the employed boundary conditions were acceptable considering the following reasons. Firstly, the 1D hemodynamic model described the systemic arterial tree of the entire cardiovascular including the cerebral arteries and had been validated to be a good option without patient-specific boundary conditions ([Marzo et al. 2009](#)). Secondly, [Xiang et al. 2014](#) tested the sensitivity of the inflow rate waveforms on CFD-based results of cerebral aneurysm hemodynamics and

reported that distinct inflow waveforms with the similar mean flow rate led to almost identical WSS and OSI distributions.

2.3.3 Numerical Solution

With consideration of the moderate Reynolds numbers in the cerebral aneurysms, the blood was considered as an incompressible Newtonian fluid controlled by the 3D transient and incompressible Navier-Stokes equations. Transient flow simulations were performed using CFX 15 (ANSYS). The convergence criteria for iterative errors were set to be of 10^{-4} . No turbulence model was applied due to the relatively low Reynolds number in this study. The simulations required approximately 8 hours of CPU time on a PC with an Intel Xeon (2.9GHz); parallel computation with a cluster on 32 nodes was carried out with Platform Computing. All the simulations were conducted up to five cardiac cycles when the flows were confirmed to reach a stable stage with a clear periodic feature and the computed results of last four cycles were used for further analysis.

2.3.4 Post-processing

Based on the computed spatiotemporal WSS distributions, the OSI was further calculated to describe the oscillatory feature of the WSS vectors, which is defined by:

$$OSI = 0.5 \left(1 - \frac{\left| \int_0^T \overline{WSS} dt \right|}{\int_0^T |\overline{WSS}| dt} \right) \quad (2-8)$$

Where $0 < OSI < 0.5$ with a value of 0 being no variation of the WSS vector, and of 0.5 being 180° deflection of the WSS direction. To investigate the effects of harmonic frequencies on flow instability in cerebral aneurysms, the inlet waveform was further decomposed into Fourier series based on Equation (2-8)

$$Q(t) = Q_0 + \sum_{n=1}^N (A_n \cos(n\omega t) + B_n \sin(n\omega t)) \quad (2-9)$$

Where Q_0 represents the constant term, N the number of harmonics, and ω the angular frequency. Note that the inlet waveform is represented reasonably based on the Fourier series with a constant term and 8 harmonics (with frequencies up to about 8.8Hz).

2.3.5 Mesh sensitivity analysis

An analysis of mesh sensitivity was firstly carried out with a steady flow condition to make sure the obtained hemodynamic factors are independent of mesh systems. The mesh refinement was confirmed with several mesh systems with the element number increasing up to 5 million based on the average and the maximum WSSs. The mean WSS turns to reach a stable stage almost unchangeable when the total elements exceeds 0.5 million. The mean and maximum WSS difference in-between 1.25 ~ 2.29 million elements was less than 3%. Secondly, a mesh-dependence of the flow instability was studied together with the influence of time increment. It was observed that the WSS fluctuations were not significant with a coarse mesh but became evident as the minimum mesh size decreased. Furthermore we confirmed that a mesh system of 5.08 million elements with a minimum element size of 0.015mm and a time step = 0.1 ms could ensure sufficiently high resolution of the WSS fluctuations in the cerebral aneurysm model.

2.4 Results

2.4.1 Flow description

Figures 2-3a, 2-3b depicts the streamline and pressure distributions at peak systole. The blood flow directly flows into the aneurysm from the parent vessel, leading to a large vortex inside and then splitting into the two daughter vessels. The vortex corresponds with a strong circulation while inducing a small vortex with much slow flow inside the bleb. The pressures inside the bleb are at very high level with a high-pressure island. As a result, the main stream of the blood flow cannot penetrate into the bleb but impinges on the neck of the bleb, resulting in a large separated flow region, the vortex in the main body of the aneurysm. Figures 2-3c, 2-3d illustrates the WSS and OSI distributions at the same time instance. A much lower WSS region is detected inside the bleb where the flow is remarkably weak; several larger WSS regions are observed around the bleb neck and in front of the aneurysm, which are identical to the high velocity regions as shown in Figure 2-3a. Hence, a steep WSS gradient apparently exists at the necks of the bleb and the aneurysm. Correspondingly, most of the aneurysm, in particular the bleb is exposed to high OSIs. It is interesting to find that at the bleb there exists a combination of low OSI and high WSS with a steep WSS gradient at the neck. The result of the combination of low WSS and high OSI in cerebral aneurysms is regarded as the main characteristics of the potential rupture indicator.

With Figure 2-4 we look at whether there are flow fluctuations associated with the aneurysm and what is its nature by plotting the temporal velocities at five points located outside and inside the aneurysm. No velocity fluctuation is observed in the parent vessel (Points 1, 2). However, the time traces of points 3, 4 and 5 apparently demonstrate pronounced velocity fluctuations in the

aneurysm. The velocity fluctuations are present initially at peak systole when the flow turns to decelerate, being enhanced throughout the late systole but decaying gradually till the mid diastole. Obviously the flow instability is observed inside the cerebral aneurysm mostly during the late systole. [Figure 2-5](#) illustrates the time courses of WSSs ([Figure 2-5b](#)) and PSDs ([Figure 2-5c](#)) at two additional points (points 6 and 7) at the two blebs of the aneurysm, where higher OSI islands ([Figure 2-5a](#)) are observed. It is seen that two types of flow instabilities exist inside the aneurysm: the low-frequency (20 ~ 40 Hz) fluctuating WSS is found at all observation points 3-7 inside the aneurysm whereas the high-frequency (105 ~ 190 Hz) fluctuating WSS is merely observed at high OSI points 6, 7. Corresponding with the velocity fluctuations, the time-varying WSS also fluctuates significantly at late systole when the flow decelerates. The frequency spectrum shows a peak range over 23-105Hz at point 6 and over 25-190Hz at point 7, respectively.

2.4.2 Inlet waveform effects on flow fluctuations

To further study the influence of inlet flow rate waveform on flow fluctuations, we performed an extended study on inlet flow rate waveform dependence by merely changing the Reynolds numbers ($Re = 180, 250$ and 335) on the basis of the mean flow rate. Only the simulation result of the second period was used for analysis here because the transitional flow between different cycles can be assumed to be negligible at such moderate Reynolds numbers in cerebral aneurysms ([Poelma et al. 2015](#)). The Reynolds number dependence was illustrated in [Figure 2-6](#) with the time courses of WSSs ([Figure 2-6a](#)) and PSDs ([Figure 2-6b](#)). There obviously exist correlations between Reynolds number and flow instability: WSS fluctuations at points 6, 7 grow remarkably and become more and more evident with increasing Reynolds numbers. Correspondingly, the PSD at point 7 presents a big jump of the maximal dominant frequency to 190Hz at $Re = 250$, compared with that at $Re = 180$, and is further elevated to 250 Hz at $Re = 335$.

Here we further investigated how the harmonic frequencies of the inlet flow rate waveform affect flow instability. In order to quantify the associations between frequency harmonics and flow fluctuations, we decomposed the flow rate waveform into Fourier series with a constant term and 8 harmonics (with frequencies up to about 8.8Hz) and performed a systematic study on how each single harmonic waveform contributes to the flow instability. This was done by investigating the WSS fluctuations at $Re = 250$, where the flow instability was evident as shown in [Figure 2-6](#). The decomposed Fourier series with 8 harmonic frequencies well represents the original 1D model-based inlet waveform ([Figure 2-2](#)). Very interestingly, as illustrated in [Figure 2-8](#), the first harmonic of the inlet flow rate waveform ($N=1$) obviously resulted in pronounced WSS fluctuations at both point 6 and point 7, which all correspond to a peak frequency of 128Hz based on the PSD analysis. Comparatively, the higher harmonic frequencies seem to extend less influence on the flow instability. [Figure 2-9](#) shows a comparison of flow rates ([Figure 2-9a](#))

between the original and the first three harmonic-based ones and the PSD-based maximal frequencies (Figure 2-9b) versus summation of the harmonics ($N=1-8$). The higher peaks were calculated to be 144, 149, 166, 175, 183, 185 and 187 Hz corresponding with the harmonics of 2, 3, 4, 5, 6, 7, and 8 ($N=2-8$). In order to confirm how each single harmonic contributes differently to the flow instability we compared the time traces of the WSS fluctuations among different harmonic frequencies at point 6 and point 7, which is shown in Figure 2-10. Clearly, the WSS fluctuations owing to the first harmonic ($N=1$) are dominant compared with those of the higher harmonics ($n=2-8$), and present at late systole when flow decelerates. Therefore, the lower harmonic frequency of the inlet flow rate waveform very likely contributes primarily to the WSS fluctuations in the cerebral aneurysms compared to the higher harmonic frequencies. Moreover, to correlate the adverse pressure gradient with the flow instability, we illustrated the relationship between pressure drops over the aneurysm and eight harmonics at peak systole in Figure 2-11. It is seen that the first harmonic obviously leads to the maximum pressure drops, which corresponds with the flow instability.

2.5 Discussion

It is well known that the WSS plays an important role in onset, progress and rupture of cerebral aneurysms. The initiation of cerebral aneurysms is widely believed to be associated with the high WSS (Dolan et al. 2008). However, there is still a controversy associated with the mechanisms of the progress and ultimate rupture of aneurysms. Both high- and low-WSS mechanisms were proposed from different viewpoints. In the present study, we focused on the flow instability and WSS fluctuations in typical cerebral aneurysm models for potential rupture indicators. Our simulation results demonstrated a highly oscillatory feature of WSSs at the cerebral aneurysm in time and space. Temporal WSS fluctuations inside the aneurysm were concretely evident at late systole, which was observed over a wide frequency range (1-190Hz) of the WSS fluctuations.

Flow fluctuations may take place under certain conditions, depending significantly on geometrical configurations and Reynolds numbers. Previous studies (Valen-Stenstad et al. 2013, 2014) have reported that the high-frequency flow instability could exist in terminal aneurysms, but not in the sidewall aneurysms, pointing to the importance of the geometry-dependence of the flow instabilities. Different Reynolds numbers can further lead to different frequency range. Yagi et al. (2013) observed the low- and high-frequency flow instabilities in a bifurcation aneurysm model but did not give the predominant frequencies. Ford and Piomelli, (2010) found high-frequency-fluctuations in all four idealized bifurcation models and two of the four patient specific bifurcation models respectively. Valen-Stenstad et al. (2011) reported that the high-frequency fluctuations were merely present in middle cerebral aneurysm (MCA) bifurcation

aneurysms but not sidewall aneurysms. In this study we discovered that both low-and high-frequency fluctuations were present in the bifurcation aneurysm model.

Inlet flow rate waveforms may also influence on the flow instability associated with cerebral aneurysms. This can be investigated either with the mean flow rate in terms of Reynolds number effects or with the time-varying flow rate in terms of harmonic frequency effects. A conclusion reached in our previous study by [Liu and Yamaguchi \(2001\)](#) is that the WSS might significant depend upon the waveform of the dynamic pulsation and this feature could be associated to the local adverse pressure gradient. With consideration of that the harmonic frequencies in inlet flow rate waveforms may correlate with the flow instability of cerebral aneurysms, we came out the idea to investigate whether and how the harmonic frequencies contribute to the flow instability with an ultimate goal to unveil its correlations with the rupture mechanisms. In this study, we utilized Fourier series expansion for the inlet flow rate waveforms to quantify the frequency-harmonic effects on the flow fluctuations. Fourier series analysis has been proven to be valid for investigation of the oscillatory components in the cardiovascular and respiratory systems ([Njemanze et al., 1991](#); [Attinger et al., 1966](#)). Our computed results indicate that the low-frequency harmonic ($N=1$) of the inlet flow rate waveform can cause a maximal dominant frequency around 128Hz, which is consistent with [Ford and Piomelli, \(2010\)](#). The maximal dominant frequency then increases from 144, 149 to 166Hz corresponding with the first 2, 3 and 4 harmonics respectively, up to the highest frequency of 190Hz with summation of all the harmonics. On one hand, we found that the WSS fluctuations become more evident with increasing Reynolds numbers ([Figure 2-6](#)). This implies that a rapidly ascending heart rate during intense physical activities will intensify the flow instability of cerebral aneurysms, which may ultimately trigger the aneurysm rupture ([Jiang et al., 2009](#)). On the other hand, we discovered that the low-frequency harmonics in the inlet flow rate waveform played a more important role in enhancing the high-frequency WSS fluctuations than the high-frequency harmonics. There are two considerably possible reasons. Firstly, the low-frequency harmonic components of the inflow likely dominate the flow instability in particular during the decelerating phase in late systole, resulting in a steeper pressure gradient, which can enhance the flow instabilities. Secondly, the flow instabilities take time to fully develop and the high frequency harmonic components may not be able to give the flow sufficient time to grow into chaotic structures. This implies that cerebral aneurysms may have good robustness against any perturbations owing to flow rate waveforms.

There are potential limitations with this CFD simulation. Firstly, The Reynolds number in the artery is much lower than the threshold of $Re=2300$, where turbulence occurs in a straight pipe flow. However, the lowest Reynolds number where high-frequency flow instabilities occurred was reported less than 500 ([Valen-Stenstad et al. 2011](#)), which is the Reynolds number for major cerebral arteries. [Ford and Piomelli, \(2010\)](#) reported a predominant frequency at approximately

120Hz at a mean Reynolds number 384. [Valen-Stenstad et al. \(2011\)](#) also found the high-frequency flow instability ranged 0-900Hz with Reynolds number varying in the range of 201-398. These previous studies on flow instability suggested a transitional model in the impingement region at a fairly low Reynolds number, but fully developed turbulence has not been observed. Numerically accurate and physically robust simulations may be significantly influenced by the uncertain factors such as modeling assumptions, boundary conditions, geometry reconstruction, mesh system, which need further extensive studies.

2.6 Conclusion

We performed a CFD study on a typical cerebral aneurysm combining with Fourier series decomposition and PSD analysis on inlet flow rate waveforms and observed significant high-frequency WSS fluctuations during flow deceleration. Moreover, we found a profound association between harmonic frequencies and flow instabilities: low-frequency in inlet flow rate harmonics likely dominate WSS fluctuations in the aneurysm, which could be associated with the primary global and local adverse pressure gradient.

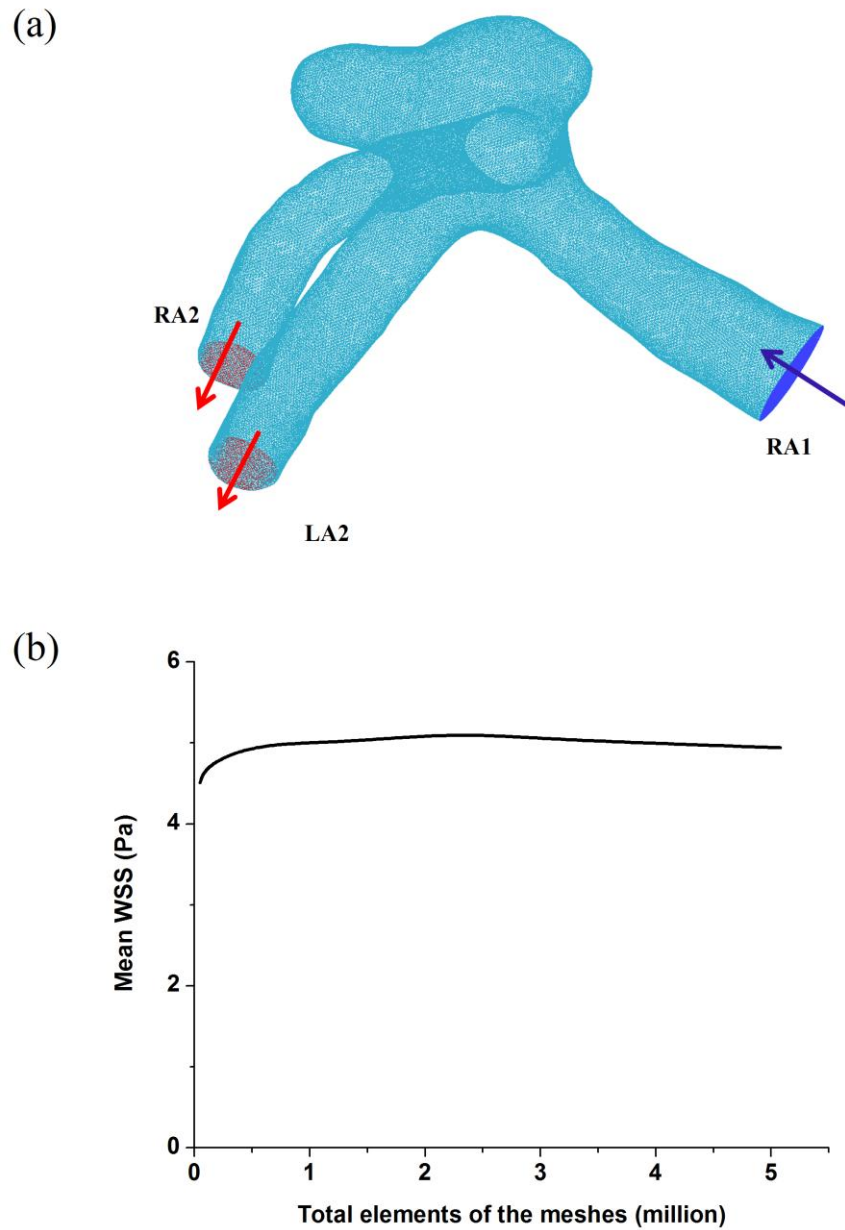


Figure 2-1. Computer model and mesh systems of a cerebral aneurysm (a) and relationship between element numbers of the meshes and mean WSS (b). RA1, RA2, LA2 denote the proximal part, the distal part of the right anterior cerebral and the distal left anterior cerebral arteries. The mean WSS show less changes with meshes increasing from 1 million up to 5 million.

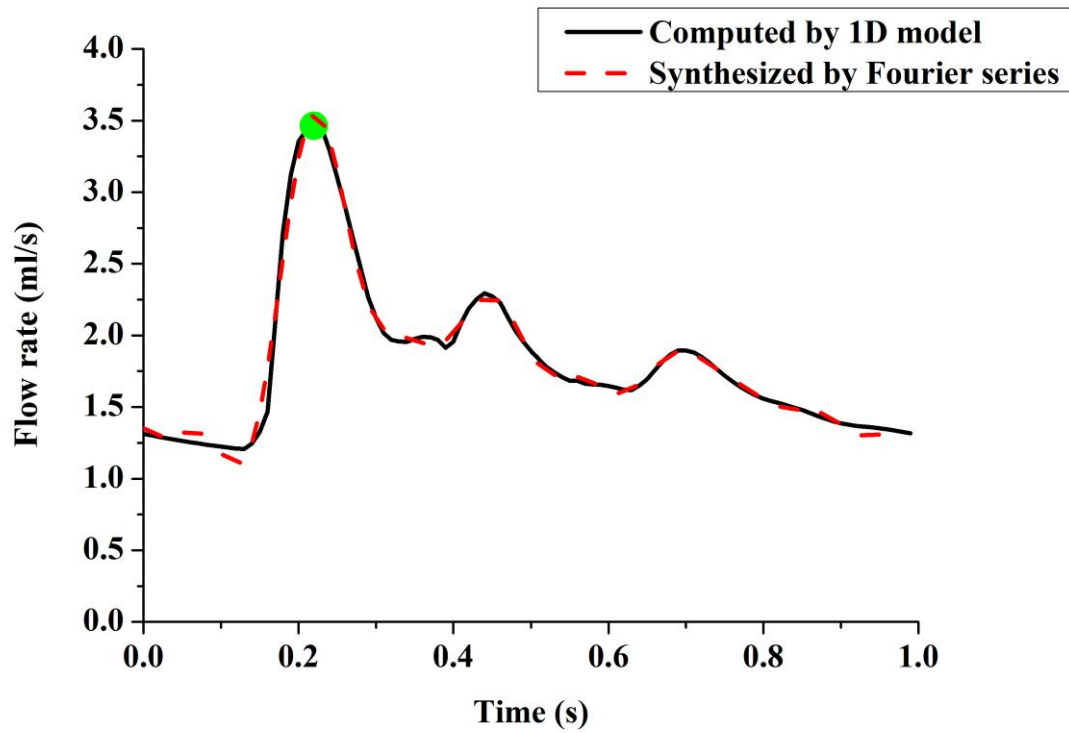


Figure 2-2. The solid line represents the inflow rate waveform obtained by a 1D model of the cardiovascular system, which is approximated by Fourier series decomposition (the dotted line) with eight harmonics. The green point means the peak systole.

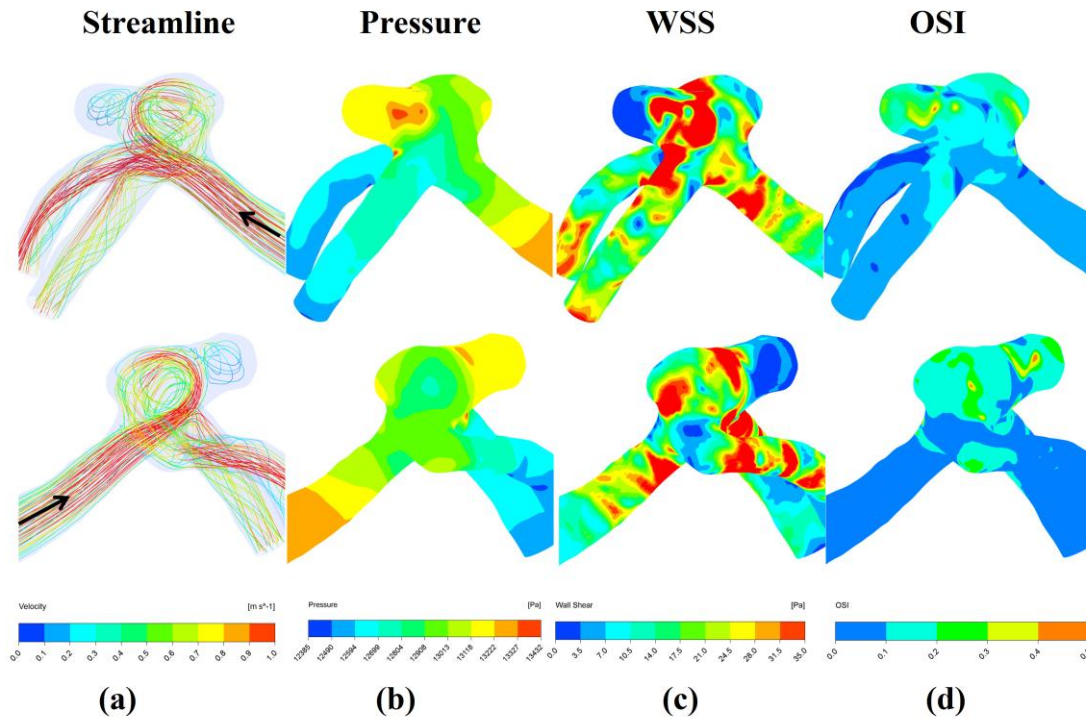


Figure 2-3. Distributions of hemodynamic factors at peak systole from two viewing angles. Upper: Anterior view, Lower: Posterior View. (a) Streamlines: The blood flowed into the aneurysm from the parent vessel directly, leading to a large vortex inside. (b) Pressures: When a region with adverse pressure gradient appeared in the aneurysm, the fluid particles could not penetrate too far into the region of increased pressure. (c) WSS: The low WSS at the large bleb was surrounded by a region of locally elevated WSS. (d) OSI: Most of the aneurysm was exposed to low OSI, while the large bleb was subjected to higher OSI.

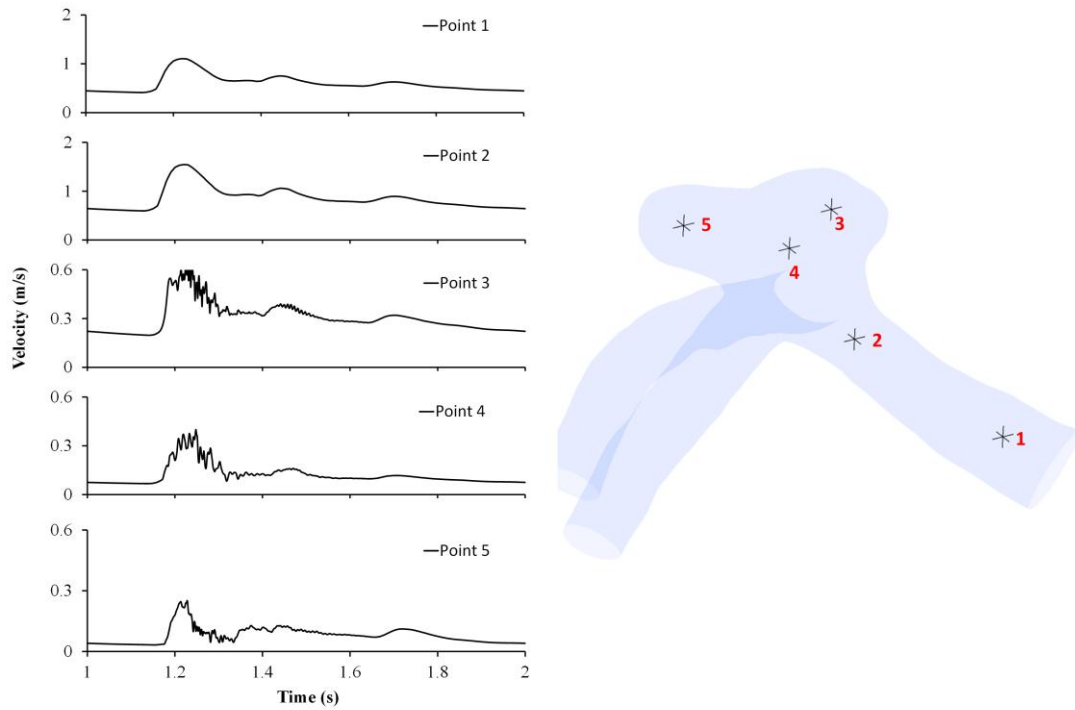


Figure 2-4. Time-varying velocities in a complete heart beat at five points in the cerebral aneurysm model. No velocity fluctuation was observed in Point 1 and 2, but the time trace of Point 3, 4 and 5 clearly demonstrates the existence of velocity fluctuation in the aneurysm.

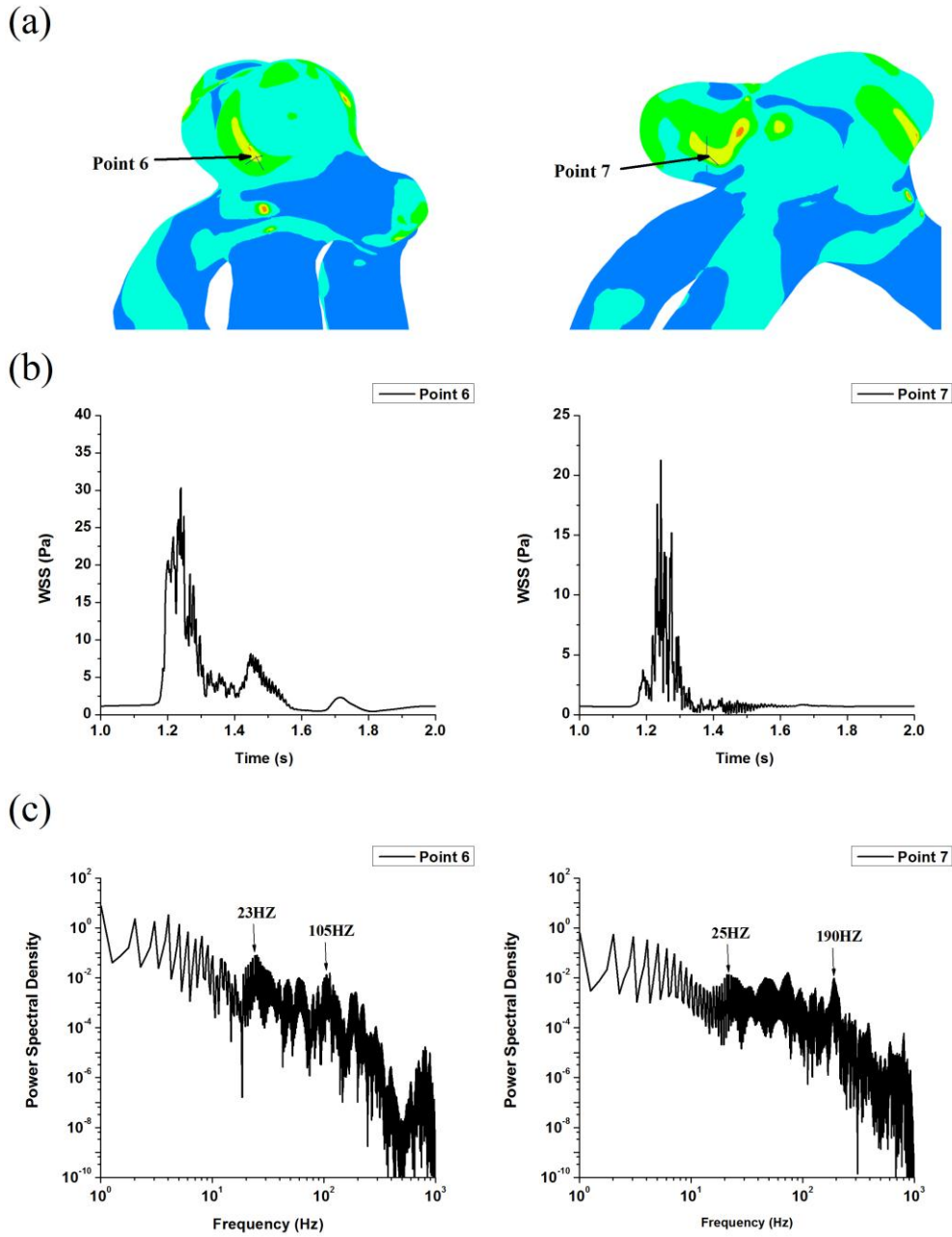


Figure 2-5. WSS fluctuations and respective PSD at the aneurysm. From top to bottom: observation points in the OSI image (a), time traces of the magnitude of WSS (b) and respective PSD (c) at two points. The WSS fluctuations were obvious in the deceleration phase at the aneurysm. The frequency spectrum of Point 6 showed some peaks ranged 23-105Hz, while Point 7 had higher temporal fluctuation and strong peaks around 25-190Hz.

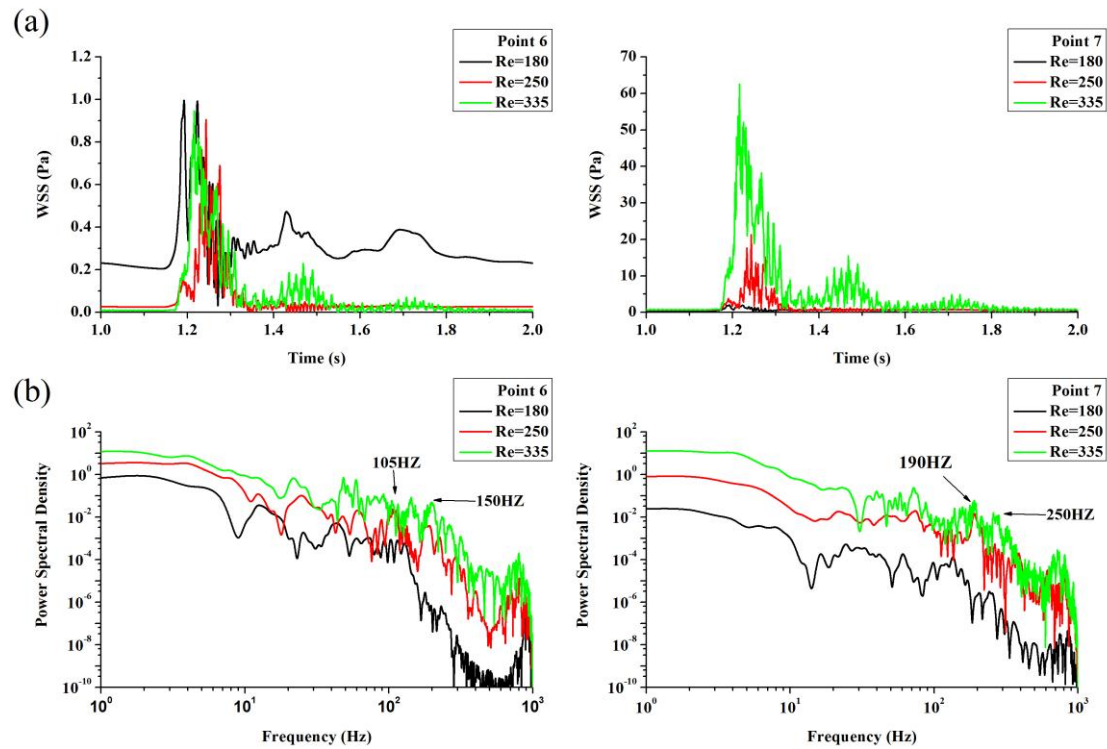


Figure 2-6. WSS fluctuations and respective PSD at the aneurysm with different average Reynolds numbers. From top to bottom: time traces of the magnitude of WSS (a) and respective PSD (b) at two points.

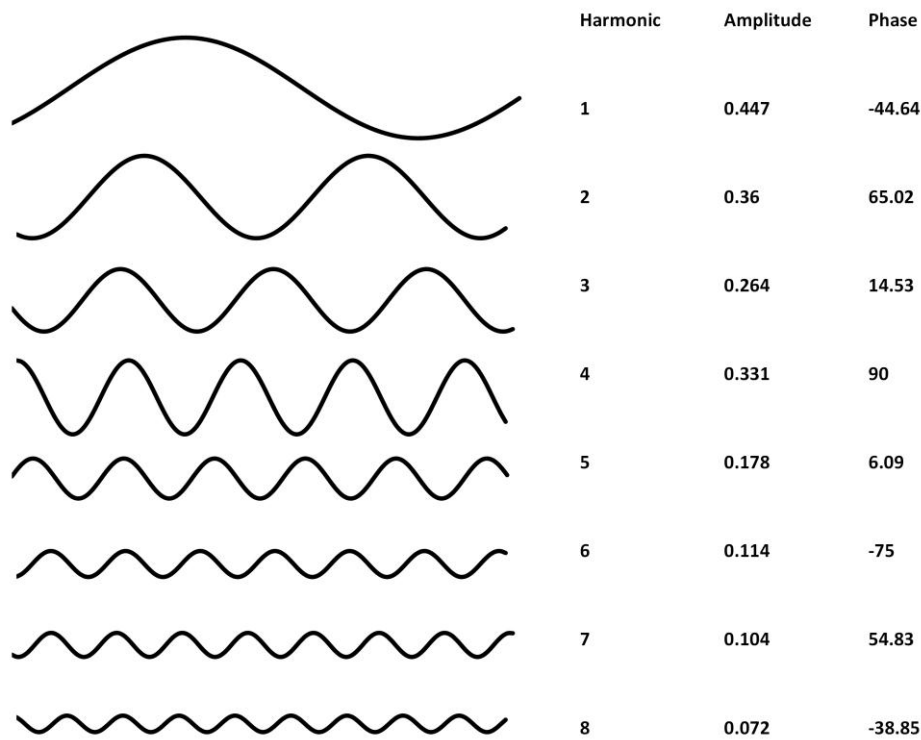


Figure 2-7. Fourier series decomposition of the inlet waveform. The coefficients for Fourier series expansions were indicated. The inlet waveform is represented by a dominant power located at about 1.1Hz in frequency domain, corresponding to 66 beats/min, with several harmonic peaks in the higher frequency ranges (2.2, 3.3, 4.4, 5.5, 6.6, 7.7 and 8.8 Hz). The constant term (1.86 ml/s) from the Fourier series expansion was the average flow rate of the original inlet wave.

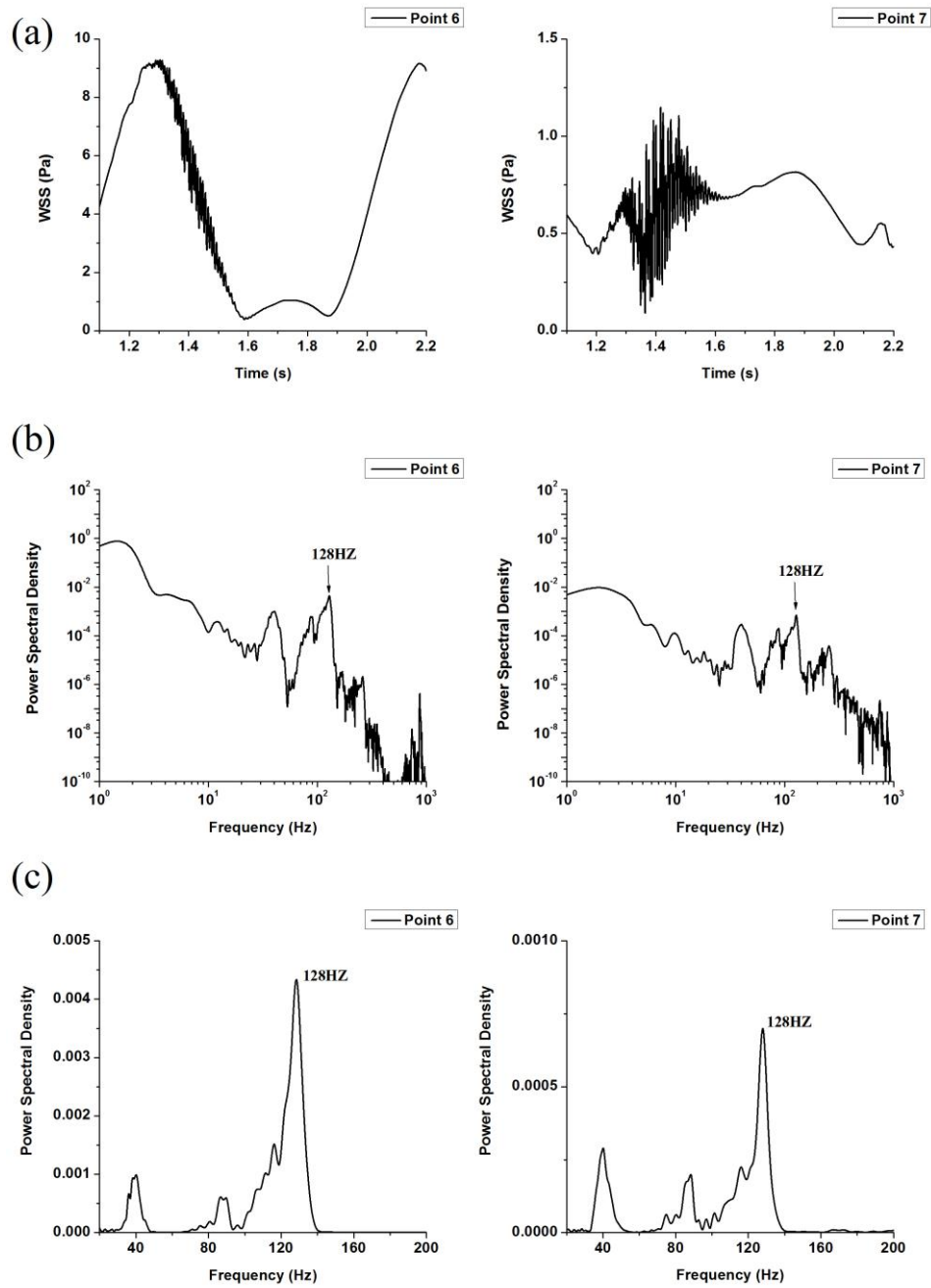


Figure 2-8. WSS fluctuations and respective PSD at the aneurysm with the inlet of the first harmonic. From top to bottom: time traces of the magnitude of WSS (a), respective PSD (b) and enlarged view of PSD (c) at two points. Significant WSS fluctuations were already present around 128Hz with the inlet of first harmonic ($N=1$).

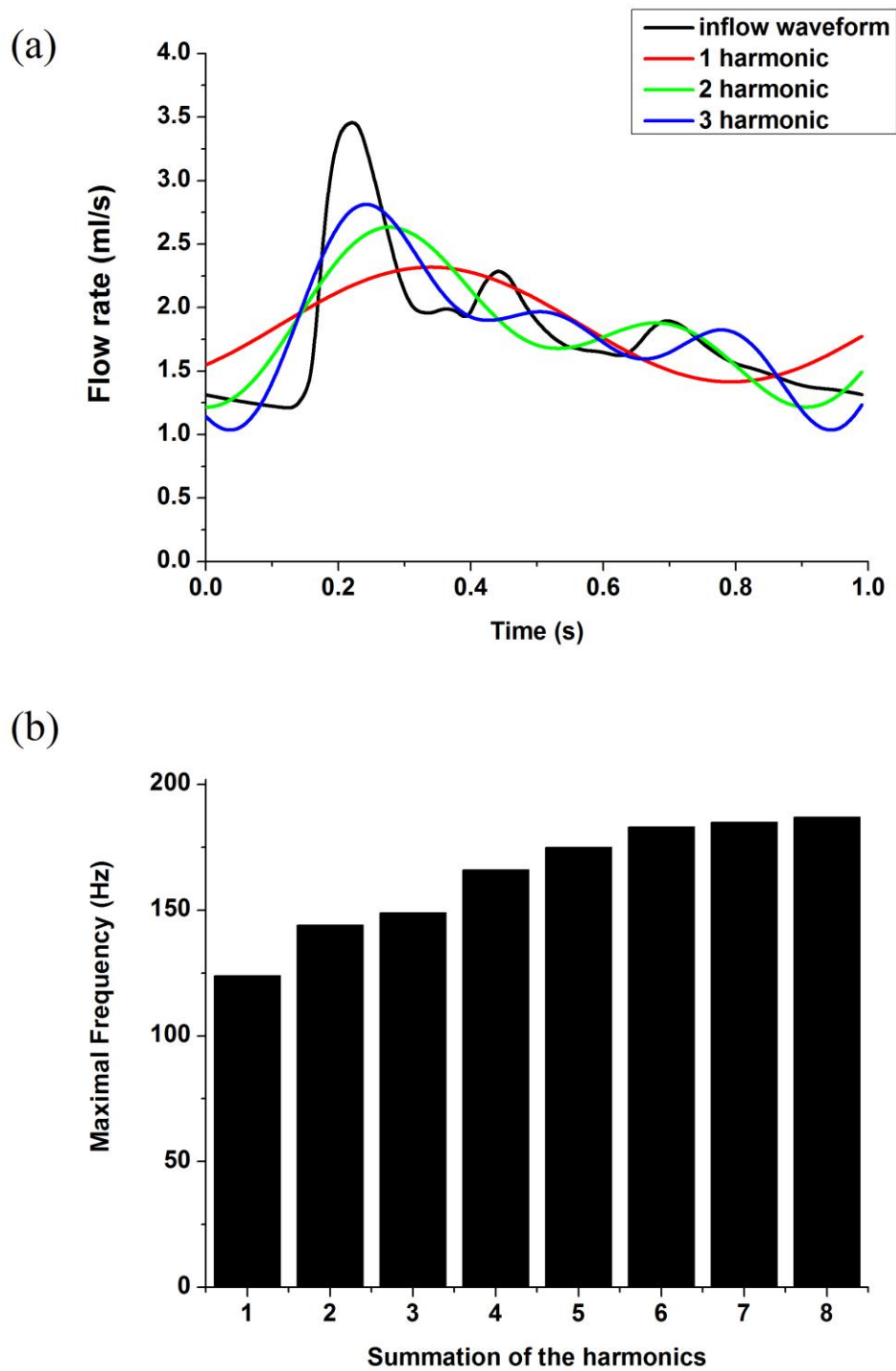


Figure 2-9. (a) The inflow waveform and Fourier series synthesis of the harmonics ($N=1,2,3$). (b) The maximum dominant frequencies observed at the aneurysm with the inlet of summated harmonics ($N=1-8$). Higher peaks at 144, 149, 166, 175, 183, 185 and 187 Hz with the inlet of the first 2, 3, 4, 5, 6, 7 and 8 harmonics ($N=2-8$).

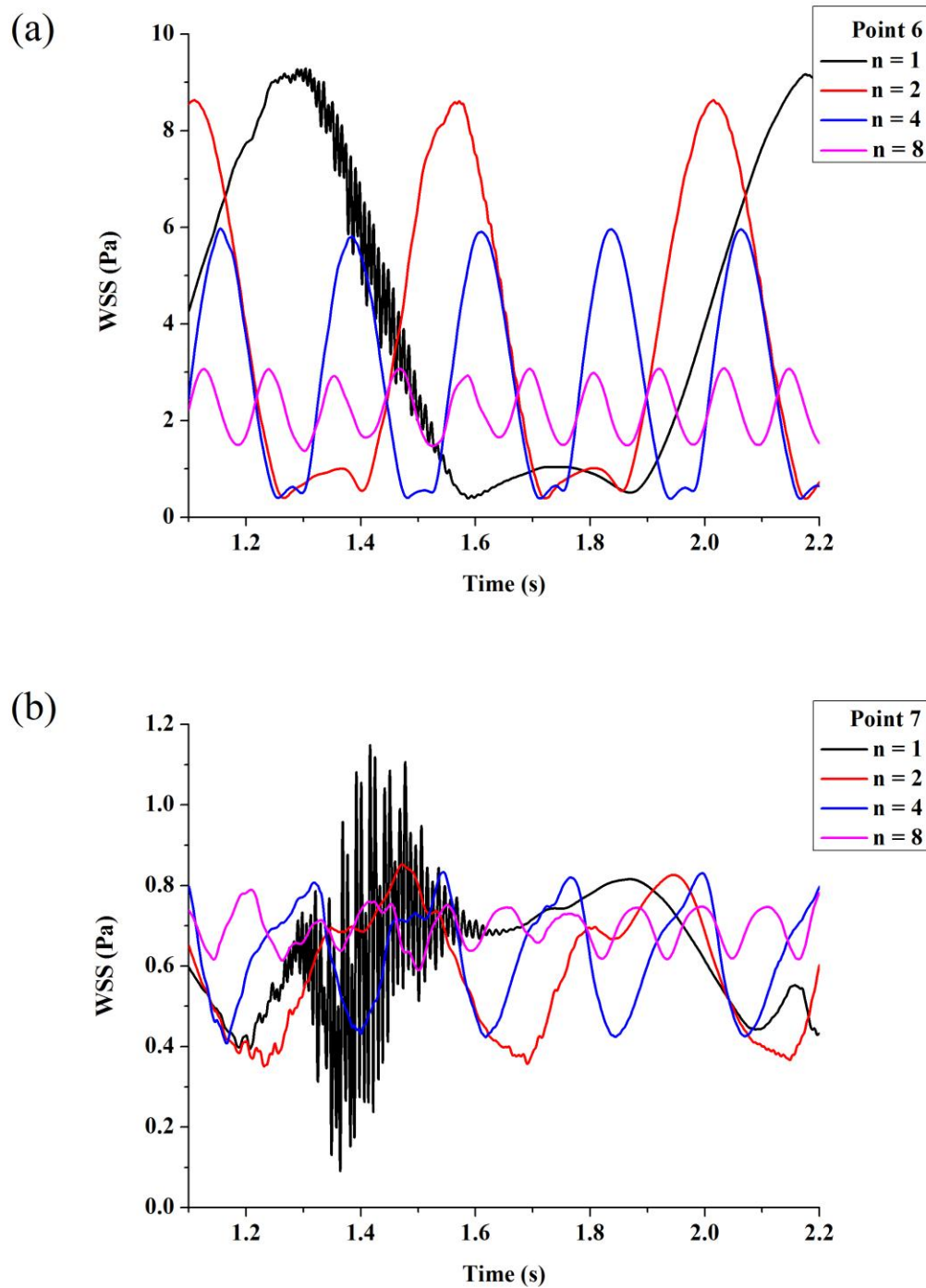


Figure 2-10. WSS fluctuations of the aneurysm with the inlet of the first, second, fourth and eighth harmonic ($n=1, 2, 4, 8$). The WSS fluctuations were obvious during the deceleration phase with the inlet of first harmonic ($n=1$), but became less significant with inlet of the higher harmonic ($n=2-8$).

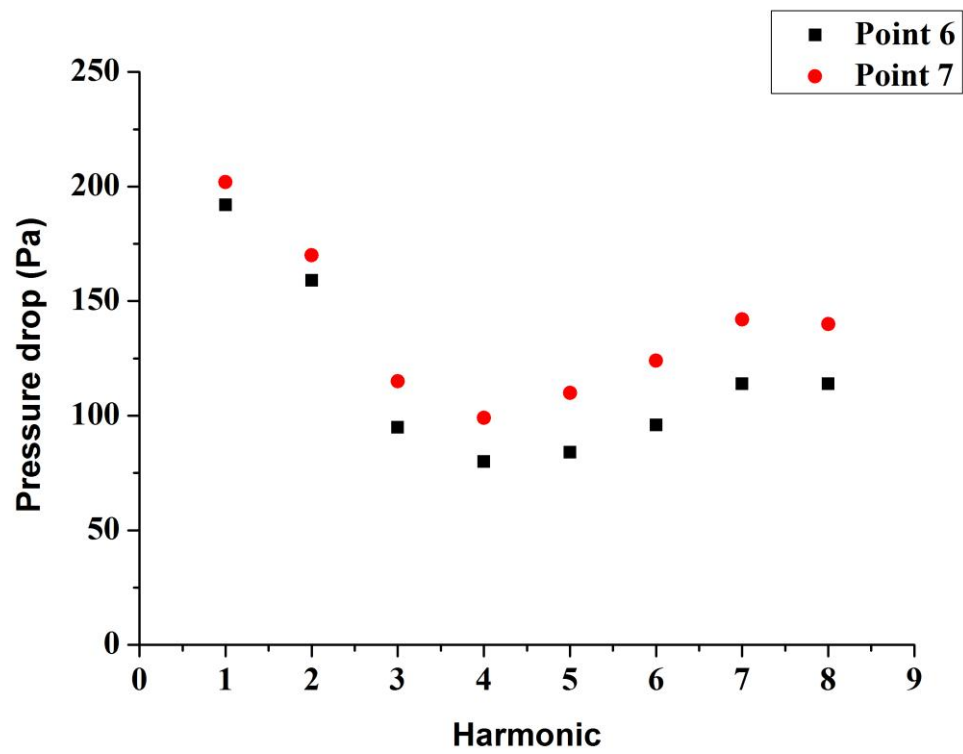


Figure 2-11. Pressure drop over the cerebral aneurysm versus the harmonics at peak systole. Clearly, the first harmonic leads to steeper pressure drop, which enhances the flow instability.

3 Waveform Dependence of flow instabilities in cerebral aneurysms

3.1 Introduction

The rupture mechanisms of cerebral aneurysms have been correlated with the hemodynamic factors. Better understanding the mechanisms associated with these events can improve diagnosis and surgery. However, the most important rupture indicator (wall shear stress, WSS) is controversially discussed: both high- and low-WSS mechanisms were proposed to explain the rupture of cerebral aneurysms (Cebal et al., 2011; Xiang et al., 2011). Estimation of rupture status in cerebral aneurysms remains challenging for clinicians and engineers.

Recently, flow instability-related studies in vessels and aneurysms have been carried out experimentally and numerically to improve the diagnosis of rupture risk (Ferguson, 1970; Steiger and Rulen, 1986; Valen-Stenstad et al., 2011; Varble et al., 2016; Yagi et al., 2013). Flow instabilities may occur under certain constraints, relying significantly on geometrical configurations and inlet flow rate waveforms. The geometric effect of blood vessel on blood flow has been a major subject till now. Beak et al. (2010) investigated the flow instabilities and oscillatory behavior of WSS on three patient specific aneurysms of the internal carotid artery (ICA) with high-resolution numerical simulations and demonstrated the presence of low-frequency-fluctuations during the decelerating systolic phase in all three ICA models. Ford and Piomelli, (2010) studied the flow instabilities using four idealized basilar aneurysm models and four patient specific terminal basilar tip aneurysms. High-frequency-fluctuations were found in all four idealized models and two of the four patient specific models respectively. On the other hand, unveiling the correlations of the flow instabilities with inlet flow rate waveforms has been another main subject since inlet flow rate waveforms also lead to the flow instability associated with cerebral aneurysms. This can be studied either by investigating the mean-flow-rate-based Reynolds number effect or by changing the time-varying flow rate in terms of Strouhal number effect or harmonic frequency effect. Several studies have already investigated the Reynolds number effects on flow instabilities in cerebral aneurysms (Baek et al., 2010; Ford and Piomelli, 2010). However, it is still not completely known how frequency harmonics in inlet flow rate waveforms influence the flow instabilities and hence WSS fluctuations in aneurysms. In this study, we aim at quantifying and unveiling the correlations between frequency harmonics in inlet flow rate waveforms and flow instabilities associated with typical terminal cerebral aneurysms, using a CFD-based model of eight cerebral aneurysms combining with Fourier series analysis on inlet flow rate waveforms.

3.2 Methods

3.2.1 Image-based anatomic modeling

We analyze six terminal cerebral aneurysms obtained from the open Aneurisk database and three from Aomori Prefecture Hospital as shown in [Figure 3-1](#). Of the nine aneurysms, one could not be reliably segmented, leaving eight (four ruptured, four unruptured) for hemodynamic analysis. Five target cerebral aneurysms are located in the anterior communicating artery, while the other three are located in the middle cerebral artery. Demographic and geometric parameters of the aneurysm models are shown in [Table 3-1](#). The register was certified by the local ethics committee and the consent was achieved for the use of diagnosis and clinical purpose from the involved patients. The geometries of the cerebral aneurysm and vessels were extracted with the set segmentation algorithm from the Vascular Modeling Toolkit (VMTK). The reconstructed surface model was then smoothened by VMTK's Taubin filter. We included the vessel geometry features as much as possible and extended the inlet and outlet by five diameters to reduce the boundary artifacts. Unstructured grids consisted of tetrahedral and prism elements were produced with the minimum element size of 0.015 mm and maximum element size of 0.06 mm in ANSYS ICEM 15.0. The total numbers of elements were ranged between 1.5 and 10 million elements in the meshes. Three prism layers were used to solve near-wall regions. Mesh-dependence was studied together with the time increment effect and confirmed that a mesh system with a minimum element size of 0.015mm and a time step = 0.5ms could be capable to provide sufficiently high resolution of the WSS fluctuations in the present cerebral aneurysms models and were substantially employed in all the simulations.

3.2.2 Boundary conditions

We imposed a Womersley velocity waveform at the inlet, which is achieved from a flow rate given with a 1D hemodynamic model of the human cardiovascular system ([Liang et al. 2009](#)) as shown in [Figure 3-2](#). The inlet waveform is represented reasonably based on the Fourier series with a dominant power located at about 1.1Hz in the frequency domain, corresponding to 66 beat/min, with seven harmonic peaks over a higher frequency range from 2.2, 3.3, 4.4, 5.5, 6.6, 7.7 up to 8.8 Hz, such as

$$V(r, t) = V_0 \left[1 - \left(\frac{r}{R} \right)^2 \right] \left\{ 1 + A \sum_{n=1}^N (a_k \cos(n\omega t) + b_k \sin(n\omega t)) \right\}$$

where the constant term V_0 represents the average velocity, A the amplitude factor ($A=1$), N the number of harmonics ($N=8$), and ω the angular frequency. The pairs of a_n and b_n normalized by V_0 are $(-0.169, 0.172)$, $(-0.179, -0.083)$, $(-0.037, -0.145)$, $(0.177, 0)$, $(0.010, 0.095)$, $(-0.060, 0.016)$, $(-0.047, -0.033)$, $(0.031, -0.023)$. A total of six simulations were conducted for each model to study the effects of heart rate and pulsation amplitude, three under pulsatile conditions corresponding to inlet average velocity of 0.4, 0.5 and 0.6 m/s with a heart rate of 66 bpm, and the other three matched to heart rates of 66, 100 and 125 bpm with a mean velocity of 0.5 m/s. The Reynolds number is computed as $Re = uD/\nu$, where V denotes the mean velocity of the inlet, D the vessel's diameter, and ν the kinematic viscosity of the fluid. The Womersley number is computed by $\sqrt{\omega R^2/\nu}$, where R represents the radius and ω the angular frequency. The Strouhal number is another dimensionless parameter computed as $St = fD/V$ with f the frequency of vortex shedding. The blood density and kinematic viscosity is 1025 kg/m^3 and $3.5 \times 10^{-6} \text{ m}^2/\text{s}$, respectively. On vessel surfaces we assumed that the compliant wall-induced deformation is negligible and hereby employed the non-slip conditions.

3.2.3 Computational fluid dynamic modelling

The blood flow is managed by the 3D transient and incompressible Navier-Stokes equations. Transient flow simulations were performed using ANSYS CFX 15.0. The convergence criteria for iterative errors were set to be of 10^{-4} . The simulations (five cardiac cycles) required approximately 12 hours of CPU time on a PC with an Intel Xeon (2.9GHz); parallel processing on 32 nodes was carried out with Platform Computing. All the simulations were conducted up to five cardiac cycles when the flows reached a stable stage and the achieved data of the last cycle were employed for analysis.

3.3 Results

3.3.1 Geometry and inflow waveform effects on WSS fluctuations

Figure 3-3 demonstrates the highly oscillatory behavior of WSSs in time. Two feature points were picked up at the entrance of the aneurysm (point a), and WSS divergence regions (point b) where the direction of WSS was observed to be quickly altered. The time-varying WSS fluctuates significantly initially at peak systole when the flow turns to decelerate, being enhanced throughout the late systole but decaying gradually till the diastole. The occurrences of flow instabilities were geometry-specific: models A-C exhibited pronounced fluctuations when flow decelerates, and thus were classified as unstable whereas flows of models D-H were stable throughout the cardiac cycle. Interestingly, all three unstable aneurysms were ruptured, whereas

all four unruptured aneurysms were stable. For models A-C, the average Reynolds numbers are 203, 257 and 208 respectively. Actually, models D-H will also experience flow instabilities at higher flow rates since WSS fluctuations grow remarkably and become more and more evident with increasing Reynolds numbers. It is clear, however, that in the same configurations flows in models A-C are more unstable than the others.

3.3.2 Geometry and inflow waveform effects on the hemodynamic factors

Figures 3-4 shows the streamline and pressure distributions for four aneurysms (two ruptured, two unruptured). The maximum velocity drop occurred between the vertex of the parent vessel and the center of vortex, followed by a recovery and then another steep drop around the vertex of the aneurysm. Corresponding with the velocity values, the primary pressure drop occurred at the vertex of the parent vessel, followed by a wild recovery and then a much steeper pressure drop over the aneurysm sac. The local pressure minimum points to the flow separation location. Specifically, models E&F showed very mild velocity recovery with much smaller pressure gradients compared to models A&B. In addition, there exist apparent correlations between Reynolds number and pressure variation: the pressures at peak systole and cycle-average conditions were found to increase with increasing Reynolds numbers. Figure 3-5 shows the hemodynamic factors at different periods with fixed average velocity for Model H. The WSS distribution at the inlet and outlet vessels almost keep the same at different heart rates, but the local high WSS island at the neck of the aneurysm obviously decreases as the heart rate is increased. The local pressure gradient around the high-pressure island also becomes steeper with decreasing heart rates. These similar dependences of the WSS and adverse local pressure gradient on the variation of the heart rate were observed in the other models.

3.3.3 Harmonic effects on pressure variations and WSS fluctuations

Here we further investigated the frequency harmonics effects on pressure variations and temporal WSS fluctuations in cerebral aneurysms. As shown in Figure 3-6, the pressure gradient shows great dependence on the variation of the harmonics: both the global and local pressure gradient decreases with higher harmonics and the first harmonic leads to the maximum pressure gradients at peak systole. When all harmonics were adjusted to the same magnitude of the first harmonic, very similar hemodynamic features are observed in Figure 3-7 like Figure 3-5. The WSS and adverse local pressure decreases with increasing harmonic-frequency. Consider the fact that Reynolds number is hold constant here, which means that the lower harmonic-frequency resembles that with lower Strouhal number of the oscillatory inflow. This demonstrated that the adverse local pressure gradient at the aneurysm is inversely proportional to the Strouhal number

at a fixed Reynolds number. **Figure 3-8** illustrates the time traces of the WSS fluctuations among different harmonic frequencies. Different frequency harmonics obviously contribute differently to the WSS fluctuations. The first harmonic of the inlet flow rate waveform ($n=1$) apparently resulted in significant WSS fluctuations. In contrast, the higher harmonics ($n=2-8$) extend less influence on the flow instability. The WSS fluctuations owing to the first harmonic are dominant compared with those of the higher harmonics, and present at late systole during the deceleration phase.

3.4 Discussion

Although much progress has been made on unveiling the rupture indicator of aneurysms, how the WSS fluctuations associated with the rupture mechanism is still little known. However, at micro-level of the arteries and aneurysms, the reaction of endothelial cells exposed to WSS fluctuations has already been widely investigated by varying the frequency, direction and gradient (Chappell et al., 1998; Himburg et al., 2007). These studies in the field of cell biology support that the high-frequency WSS fluctuations and rapidly changing direction of WSS, not the magnitude of WSSs alone, could have a great important effect on the life-cycle of the aneurysm. In this study, we found significant WSS fluctuations in three ruptured aneurysms A-C when flow decelerates and no pronounced fluctuations in four unruptured aneurysms E-H throughout the cardiac cycle, suggesting the potential association between the flow instability and rupture mechanism. This result may help for a better understanding of the rupture mechanism although the present study with a small sample does not attempt to separate the ruptured - unruptured aneurysms. On the other hand, flow instabilities also significantly depend upon the pulsatile waveform, which is obviously correlated to the Reynolds number. For Models A-C, the flow instability became pronounced at a low Reynolds number ranged 203-257. The flow in models D-H will also become unstable when the average Reynolds numbers increase to higher Reynolds numbers.

Our computed results demonstrated that the low-frequency harmonics in the inlet flow rate waveform played a crucial role in enhancing the high-frequency WSS fluctuations compared to the high-frequency harmonics, which corresponds with a steeper global and local pressure gradient. Overall, the global and adverse local pressure gradients were dominated by the inertial force of the flow and the separation of the vortices, showing great sensitivity to the mean flow rate in terms of Reynolds number and the time-varying flow rate in terms of Strouhal number, respectively. At a fixed heart rate, an increase in inlet flow rate will lead to stronger inertia effects, enhancing flow instability. At fixed inflow rate, the effect of decreasing the heart rate is similar to increasing the inflow rate. The adverse local pressure gradient enhances or counteracts the global

pressure gradient due to the flow acceleration or deceleration, which is of great importance in the flow instabilities (Liu and Yamaguchi, 2001). Here waveform dependence on flow instabilities has been confirmed. Given the geometry of the cerebral aneurysm, the flow instability is enhanced with increasing Reynolds number and decreasing Strouhal number. Moreover, to figure out how much the low or high frequency harmonics in the inlet flow-rate waveform contribute differently to the flow instabilities, we utilized Fourier series expansion for the inlet flow rate waveforms to quantify the frequency-harmonic effects on the flow instabilities. The lower harmonics of the inlet waveform leads to higher global and adverse local pressure gradient due to the much higher Reynolds number and lower Strouhal number compared to higher harmonics. The flow instability generally takes time to be fully developed at systole, but the high frequency harmonic components with shorter systolic portion may not be able to give the flow sufficient time to grow up into the chaotic structures. As a result, the lower harmonic frequency of the inlet flow rate waveform very likely to be essential to inducing greater global and adverse local pressure gradient, and hence contributes primarily to the WSS fluctuations compared to the higher harmonic frequencies in terminal cerebral aneurysms.

Physiologically, the blood flow patterns could be highly disturbed due to intense physical and emotional excitement (Jiang and Strother, 2016). Moreover, Valen-Stenstad et al. (2013) have proposed that the flow instabilities arising in the ICA siphon could propagate into MCA bifurcation and may also propagate into the aneurysm. However, many CFD studies on anterior aneurysms did not include the ICA siphon upstream, while using truncated inlet instead. The important implication of this study is that cerebral aneurysms hemodynamics could be of some robustness, dependent mainly on the primary harmonic frequency, but against unpredictable high-frequency perturbations arising in the parent vessels.

Numerically accurate and physically robust simulations could be significantly influenced by the uncertain factors such as modeling assumptions, boundary conditions, geometry reconstruction, mesh system. There are potential limitations in this CFD simulation. Firstly, the simplified assumption of dealing the hemodynamics in aneurysm sac as a laminar flow needs to be attentively considered especially in the impingement of the aneurysm in future. The Reynolds number in the cerebral artery is much lower than the threshold of $Re=2300$, where turbulence occurs in a straight pipe flow. However, even at the low Reynolds numbers less than 500 identical to that for major cerebral arteries, the high-frequency flow instabilities have also been observed. Although these studies proposed a transitional model in the impingement region at a fairly low Reynolds number, completely developed turbulence has not been detected yet in the cerebral aneurysms. It is more natural to think that the flow fields associated with the aneurysm is more likely a disturbed laminar flow, and therefore a laminar flow is assumed here. Another limitation is due to the Newtonian fluid assumption, which may to some extent influence the simulation

results. The non-Newtonian effect is usually negligible in cerebral arteries in laminar flows due to its modest effect on flow patterns. However, there are also suggestions that non-Newtonian effects may not be negligible in turbulent or turbulent-like flows. With consideration of the moderate Reynolds numbers in the cerebral arteries with aneurysms, the blood flow was presumed as incompressible Newtonian fluid in this study. The non-Newtonian effects on flow instabilities need further extensive studies. Moreover, the wall elasticity may to some extent influence the flow patterns in the cerebral aneurysm models, which also need to be carefully considered in future.

3.5 Conclusions

This study investigated eight terminal cerebral aneurysms, in which flow instabilities were observed in three ruptured aneurysms and showed strong correlations with low-frequency harmonics in inlet flow rate waveforms. Low-frequency harmonics in inlet flow rates play an important role in causing WSS fluctuations in cerebral aneurysms, which is inherently correlated with the existence of a primary adverse pressure gradient at late systole. This observed feature of the harmonic frequency-dependence on flow fluctuations implies that cerebral aneurysm hemodynamics could be of some robustness, dependent mainly on the low-frequency harmonics initiated by heart contraction but insensitive to the unpredictable high-frequency perturbations in the inflow waveforms.

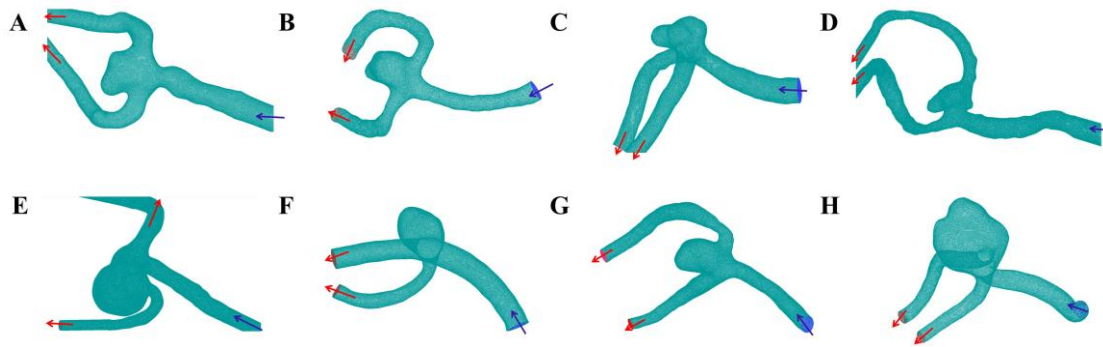


Figure 3-1. Eight patient-specific terminal cerebral aneurysm models used in simulations (ruptured aneurysms A-D, unruptured aneurysms E-H).

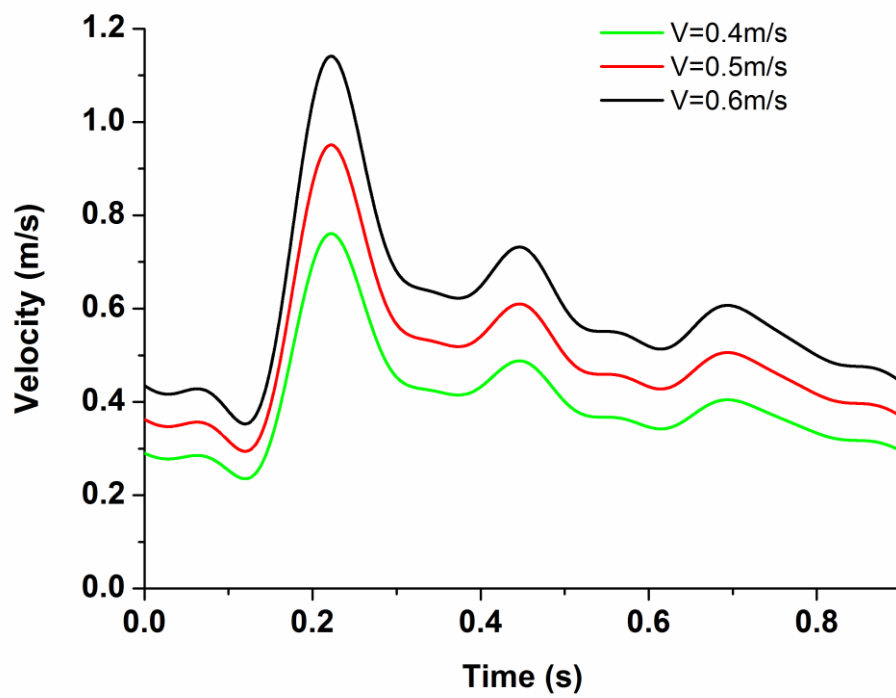


Figure 3-2. The inlet velocity waveforms in a cardiac cycle at three average velocities: 0.4m/s, green line; 0.5m/s, red line; 0.6m/s, black line.

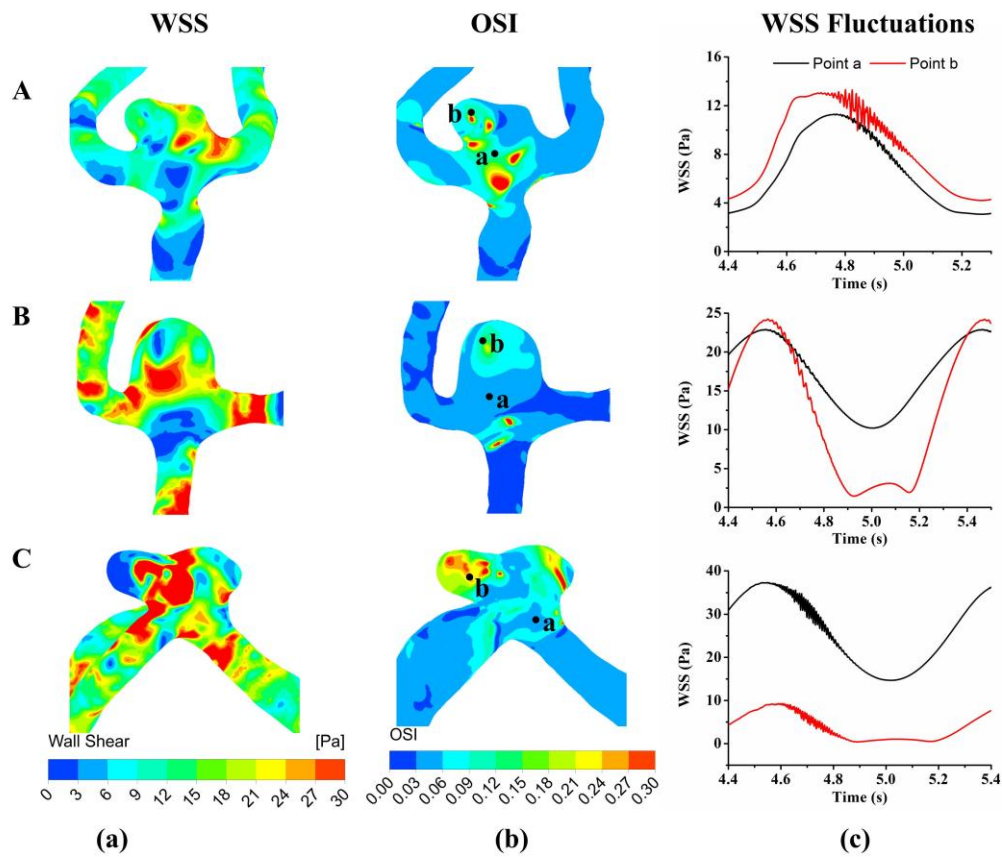


Figure 3-3. Visualization of WSS fluctuations associated with cerebral aneurysm models A-C. Two snapshots of instantaneous WSSs (a) and OSIs (b) at peak systole; time-varying WSSs (c) at two feature points (point a, black line; point b, red line) with the inflow rate of the first harmonic ($n=1$). The average Reynolds numbers of models A-C are 203, 257 and 208 respectively.

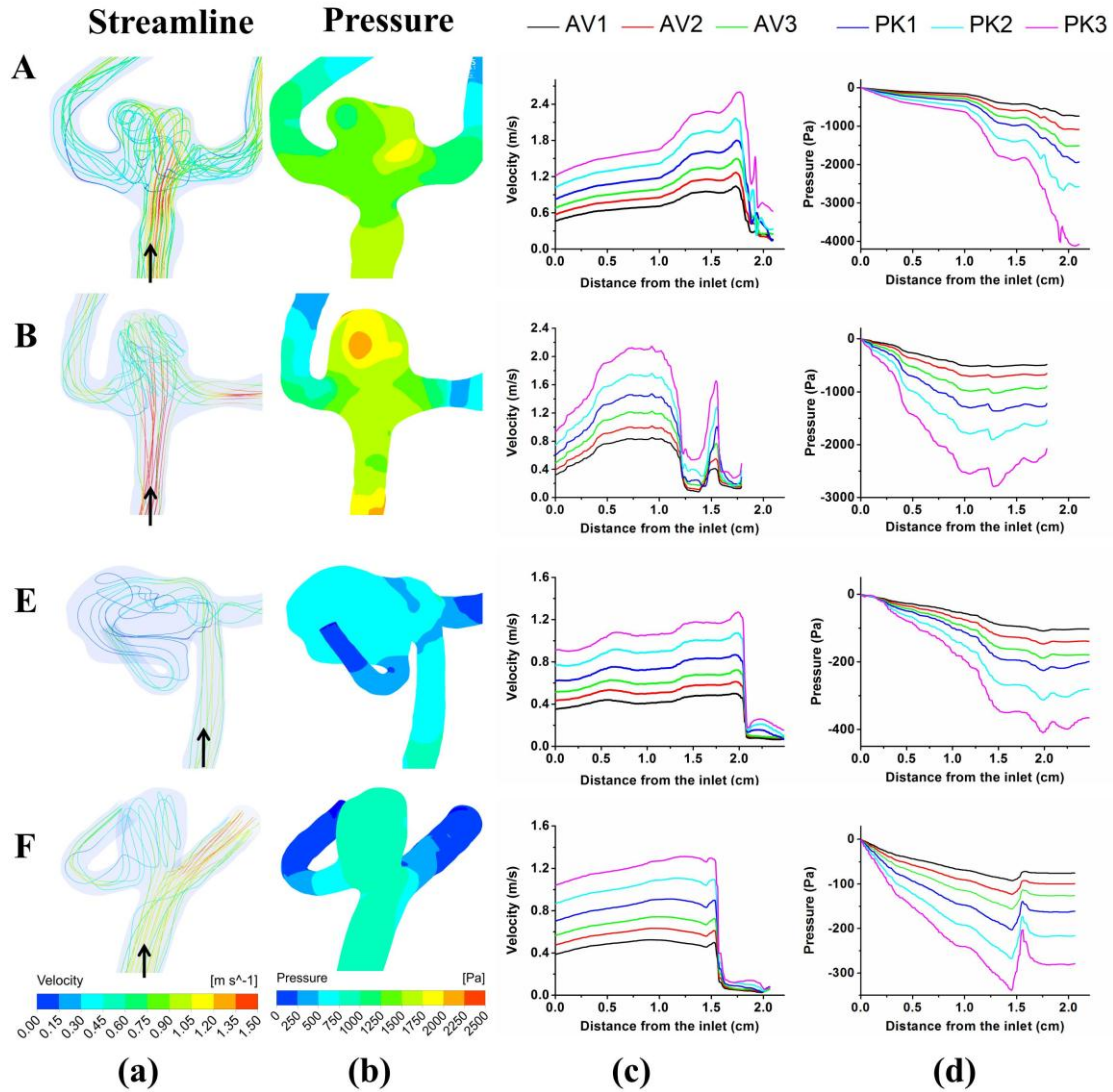


Figure 3-4. Visualization of streamline and pressure distribution at different inlet velocities: 0.4, 0.5 and 0.6 m/s with a heart rate of 66 bpm (ruptured aneurysms A&B, unruptured aneurysms E&F). Two snapshots of instantaneous streamlines (a) and pressures (b) at peak systole; centerline analysis for peak systolic (PK1, PK2, PK3) and averaged (AV1, AV2, AV3) velocities (c) and pressures (d), which show the pressure differences compared with that at inlet.

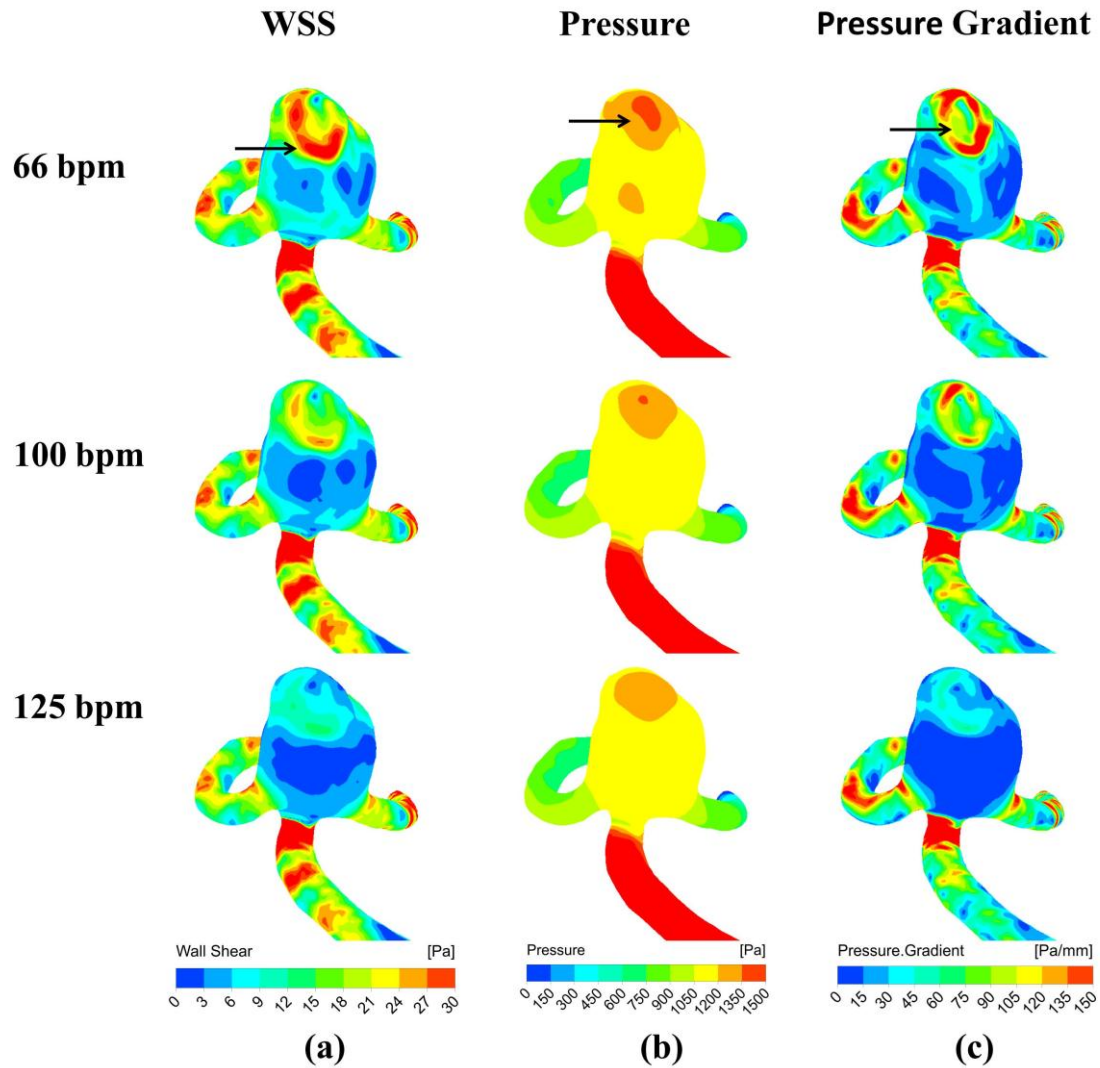


Figure 3-5. Visualization of WSS (a), pressure (b) and pressure gradient distribution (c) at peak systole for three different heart rates: 66, 100 and 125bpm with an average velocity of 0.5m/s (cerebral aneurysm model H, $Re=291$). The arrow shows the local high-pressure island identical to some stagnation point inside the aneurysm, which leads to an adverse local pressure gradient against the flow into the aneurysm.

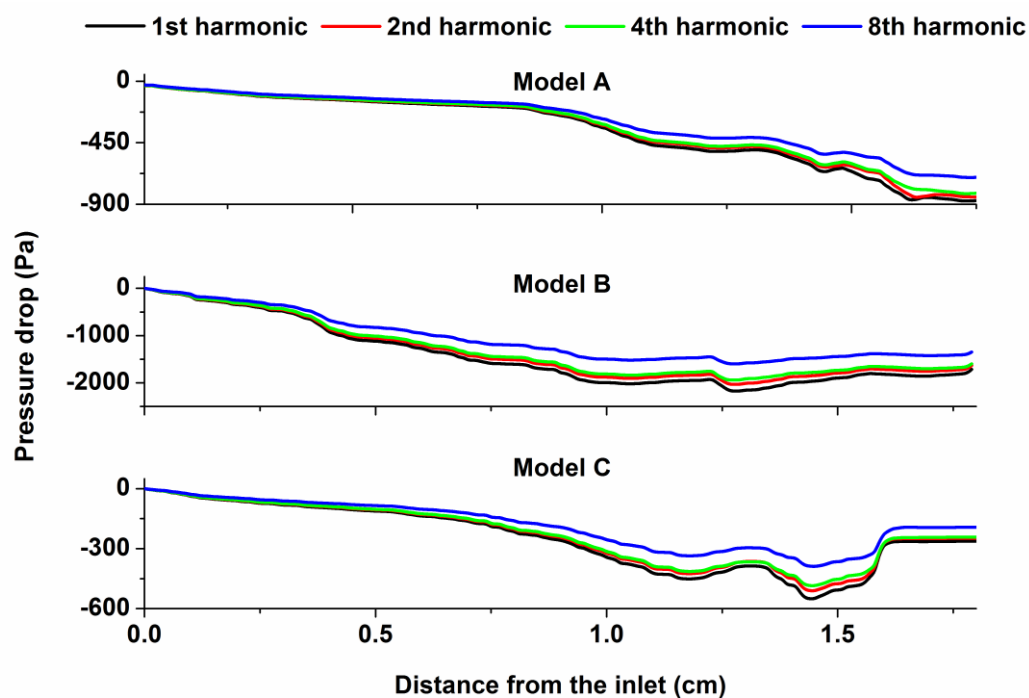


Figure 3-6. Centerline analysis for pressure drop versus harmonics inside the cerebral aneurysm models A-C at peak systole. Obviously, the low-frequency harmonic ($n=1$) leads to steeper pressure drops compared to the high-frequency harmonics ($n=2-8$).

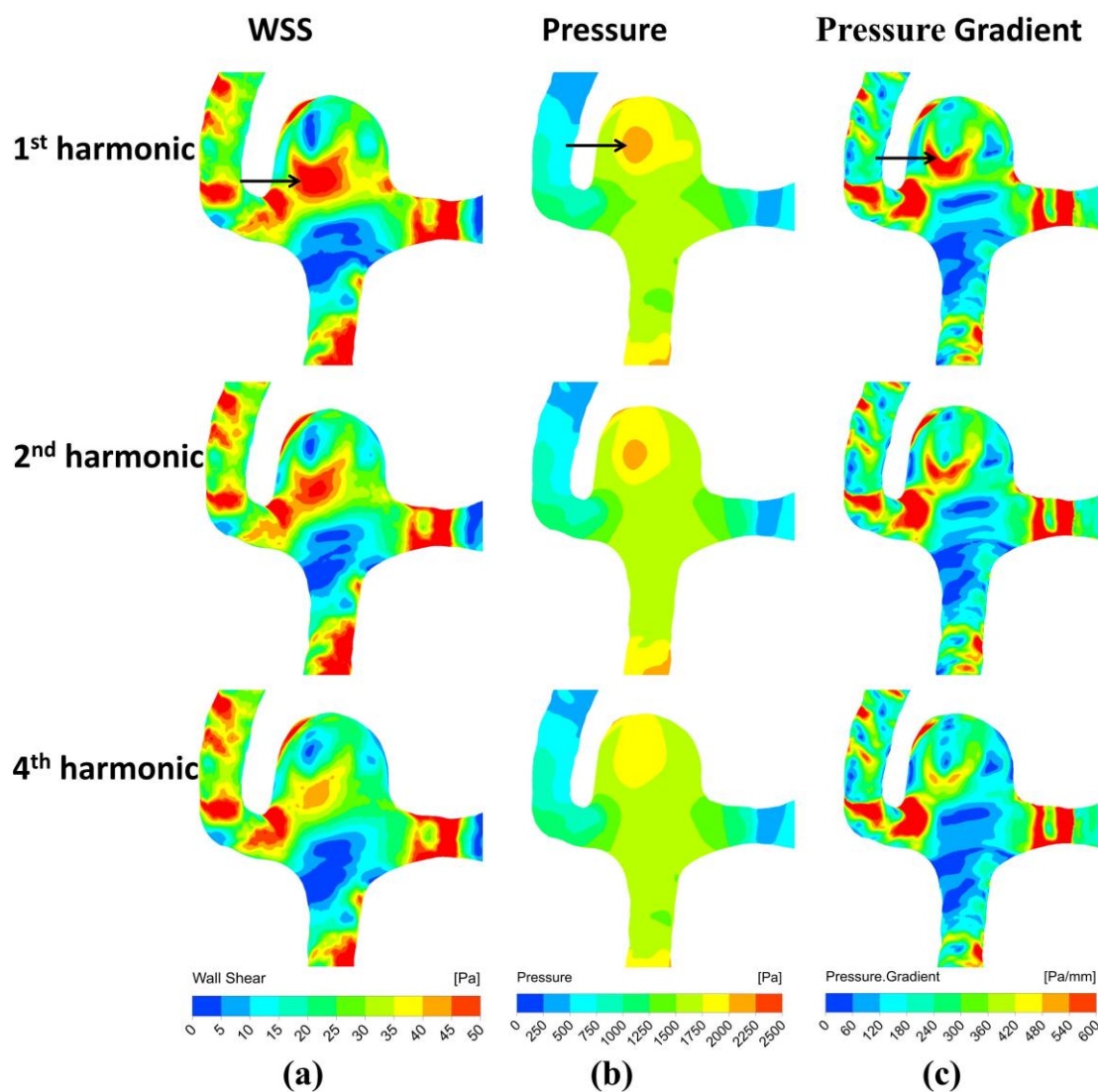


Figure 3-7. Visualization of WSS (a), pressure (b) and pressure gradient distribution (c) at peak systole with the inflow rate of the three harmonics ($n=1, 2$ and 4) (cerebral aneurysm model B, $Re=257$).

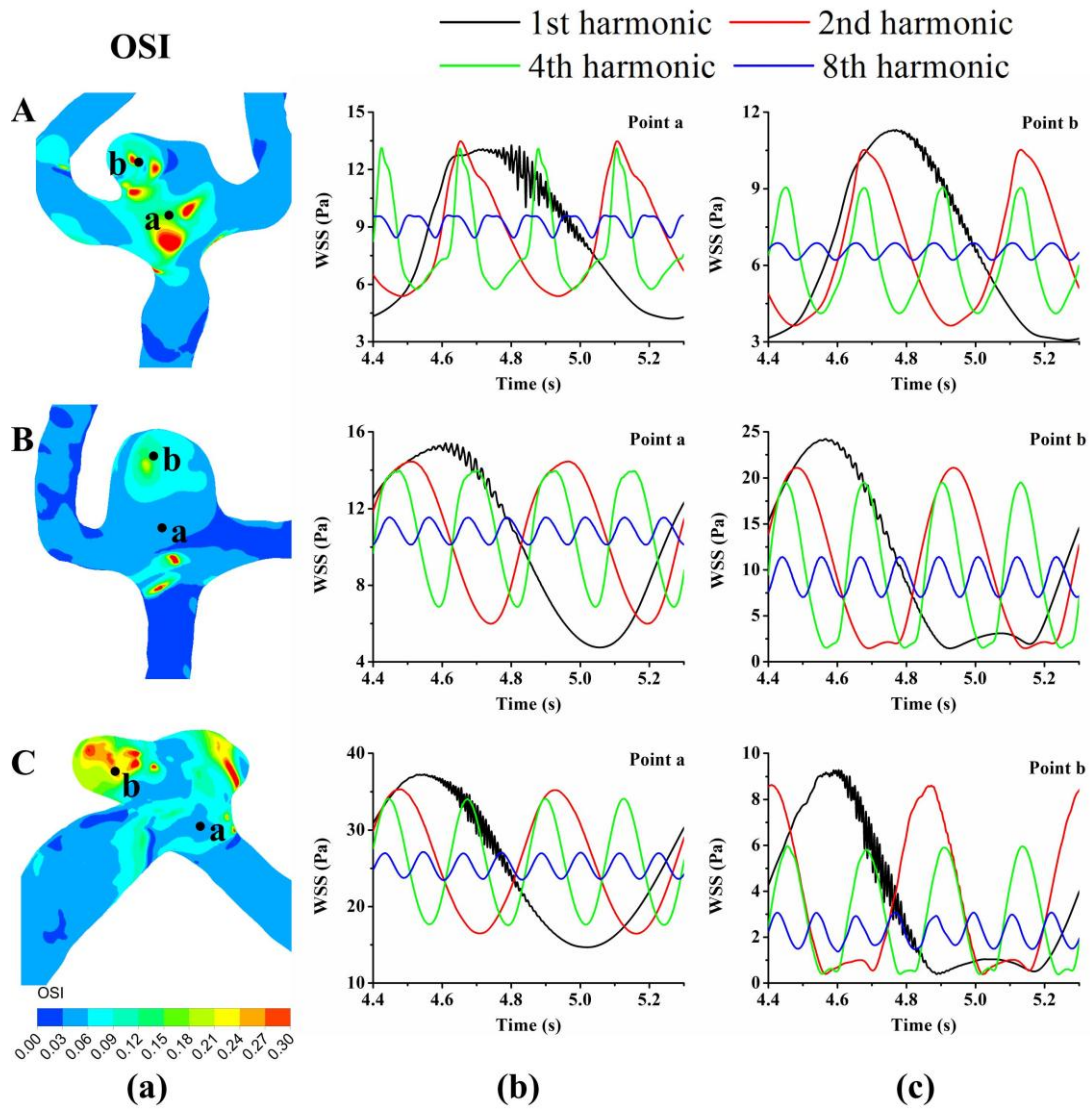


Figure 3-8. Visualization of WSS fluctuations associated with cerebral aneurysm models A-C. Instantaneous OSIs (a) at peak systole and time-varying WSSs at feature points (b)-(c) with the inflow rate of the four harmonics ($n=1$, black line; $n=2$, red line; $n=4$, green line; $n=8$, blue line). For models A-C, the average Reynolds numbers are 203, 257 and 208 respectively. WSS fluctuations are evident during the deceleration phase at the first harmonic ($n=1$), but dramatically become invisible at the higher harmonics ($n=2-8$).

Model	Age	Sex	Location	Status	R (mm)	Aspect ratio	Size ratio	Flow Type
A	36	M	ACA	Ruptured	1.2	0.78	1.61	Unstable
B	74	F	ACA	Ruptured	0.7	0.91	2.42	Unstable
C	50	F	ACA	Ruptured	1.23	2.22	2.48	Unstable
D	67	F	MCA	Ruptured	1.35	2.19	2.20	Stable
E	72	M	MCA	Unruptured	1.38	1.41	4.18	Stable
F	59	F	MCA	Unruptured	1.14	1.29	2.30	Stable
G	65	F	ACA	Unruptured	0.8	1.21	2.74	Stable
H	69	M	ACA	Unruptured	1.2	1.16	3.93	Stable

Table 3-1. Demographic, morphologic parameters and flow characteristics of the eight cerebral aneurysms

4 Elastic wall influence on the hemodynamic factors in cerebral aneurysms

4.1 Introduction

Wall elasticity could provide essential information towards a better understanding the influence of blood flow on the elastic wall. The fully coupled fluid-structure interaction (FSI) is becoming an effective tool for assessing the influence of elastic wall. [Zeng et al., \(2003\)](#) examined the effects of cardiac-induced motion on the hemodynamic factors in the human right coronary arteries and found that the arterial motion had little influence on the general flow patterns and WSS distribution. [Zhao et al., \(2000\)](#) employed a vascular geometry from in vivo angiograms and a computational FSI method to study blood-wall interactions and demonstrated that the WSS magnitude was generally reduced but the general flow patterns did not changed. [Tada and Tarbell \(2005\)](#) studied the elastic wall effects on the common carotid and external carotid arteries with FSI simulations and proposed the elastic wall could greatly influence the simulated results. [Torii et al. \(2007\)](#) performed a FSI study of blood flow to study the flexible wall effects on the flow patterns and found that the aneurysm wall deformation had an important role in the WSS distribution. [Bazilevs et al. \(2010\)](#) performed FSI on four patient-specific aneurysms models and proposed that the elastic wall could be of great importance in predict the accurate WSS and flow patterns. [Lee et al. \(2013\)](#) employed FSI on two ruptured and thee unruptured aneurysms models under normal and high pressure conditions and concluded that the ruptured aneurysms exhibited much larger deformation at the dome and lower WSS compared to unruptured aneurysms.

Several studies have already been carried on to understand the elastic wall effect on the hemodynamics experimentally and numerically, but they mainly focused on the elastic effect on the entire aneurysm. The elastic wall effects on the aneurysm blebs were not fully studied, which are regarded as the specific area at high rupture risk. Not much information is known about the influence of wall elasticity on patient specific cerebral aneurysm blebs during pulsatile flow. In our previous study ([Xu et al. 2016](#)) at anterior cerebral arteries, both the experiment and CFD simulation results show that the average value of WSS in elastic model is 9.44% smaller than that in the rigid model. The elasticity of the aneurysm wall could dampen the change of WSS, which suggests that the rigid model may proliferate the risk of aneurysm rupture. But that research was performed with idealize cerebral aneurysm models that could not represent the realistic aneurysm geometries. To further understand the effect of wall elasticity on the hemodynamics, our study used fluid-structure interaction method to investigate the

hemodynamic factors and flow patterns in two typical cerebral aneurysms with blebs, which are prone to rupture. Great differences of hemodynamic factors and flow patterns were observed at the blebs between the rigid and elastic models. Our simulation suggests that elastic effects should be considered in the flow instability analysis since the influence is significant especially in the impingement and slow flow regions of the aneurysms.

4.2. Material and methods

4.2.1 Imaging and patient data

To get representative aneurysms, cerebral aneurysms with blebs were chosen from open Aneurisk and our database. The first cerebral aneurysm is located in the middle cerebral artery. The depth of the aneurysm is 5.76 mm and the width of neck is 3.73 mm. The diameter of the parent vessel is 1.82 mm. The daughter vessels are 1.24 and 0.96 mm in diameter respectively. We included the geometries of vessels and aneurysms as much as possible create realistic boundary conditions. According to the diameter of the inlet vessel and the inlet velocity, the maximum and minimum Reynolds numbers are 606 and 254 respectively. The Womersley number is 1.72. The second one is placed at the anterior communicating artery, which usually receives blood from the anterior cerebral arteries. Our model consists of the proximal part of the right anterior cerebral artery (RA1&RA2) and the distal left anterior cerebral artery (LA2). The proximal left anterior cerebral artery of this particular patient was neglected since its diameter was very small (hypoplastic or aplastic). The DICOM images of the arteries and the aneurysms were accomplished with 3D digital subtraction angiography (DSA). DSA images with a slice thickness of 0.2 mm intervals were employed for the reconstruction.

4.2.2 CFD simulation

The blood fluid was assumed as an incompressible Newtonian fluid in this research, considering the non-Newtonian effect on the flow was generally negligible in cerebral arteries. The blood density and dynamic kinematic viscosity were defined as 1025 kg/m^3 and $0.0035 \text{ Pa} \cdot \text{s}$ respectively. A uniform elastic wall (thickness 0.25 mm, 10% of the diameter, Poisson ratio 0.4, Young modulus 2 MPa) was applied since it was difficult to measure the distribution of vessel wall elasticity and thickness. 1.25 million finite volume Tetrahedral and Prism elements were generated with ANSYS ICEM (Number of layers 3, Height ratio 1.2). The calculation was performed on 4 CPU, and each cycle cost 14 hours. Due to the computational cost and storage limit, we simulated 5 heartbeats with a time period of 1 second, where the last 4 cycles were used for further statistics. The convergence criteria for iterative errors were set to be of 10^{-4} . The governing equations for the fluid are transient 3D Navier-Stokes equations. [Figure 4-1](#) shows

the boundary conditions obtained from the human cardiovascular system. The pressure wave is used at the inlet boundary condition. The maximum pressure value is 116 mmHg, which stands as the peak systolic pressure. The same flow rate wave is prescribed as the outlet boundary condition of the RA2 and LA2, with a peak flow rate of 2.3 ml/s. These boundary conditions will be talked in the discussion part.

4.2.3 Mesh independence tests

Mesh sensitivity test has been carried out in the steady flow to make sure the obtained results are independent on the mesh density. A series of meshes with increasing number of elements (0.01 to 5 million) were produced as a standard for the mesh resolutions. The assessment of the distinct meshes was according to the average WSS. The average WSS is almost steady when the total elements are larger than 0.5 million. The average WSS difference between our mesh (1.25 million elements) and adjacent mesh (2.29 million elements) was less than 3%.

4.2.4 Validation tests

The methods used in this paper have already been well validated with experiments in our previous research (Xu et al. 2016). Particle imaging velocimetry (PIV) experiments and CFD were carried out on the aneurysm, which was also located at the bifurcation of anterior cerebral artery and the anterior communicating artery. Firstly, we develop both rigid and elastic models of the aneurysm, using PIV. Secondly, the rigid and elastic simulation models using CFD are established to validate the PIV results of the cerebral aneurysm model, in which the fluid is assumed as incompressible, Newtonian laminar flow. Our simulation results show that the average value of WSS in elastic model is 9.44% smaller than that in the rigid model. The PIV results demonstrate that the average value of WSS in elastic model is 10% smaller than that in the rigid model as well. In conclusion, the simulation results of the rigid and elastic model prove to be qualitatively similar to respective PIV results. Moreover, the results of simulation and PIV both show that the elasticity of the aneurysm wall could dampen the change of WSS, which suggests that the rigid model may proliferate the risk of aneurysm rupture. As shown in Figure 4-2, the WSS values of 21 points in the middle plane are obtained at peak systole and diastole. The simulation results prove to be qualitatively similar to respective PIV results.

4.3 Results

Figure 4-3 demonstrated that most of the blood did not flow into the dome, but impinged the neck of the aneurysm strongly, leading to relatively lower WSS value in the dome and higher WSS value in the neck. Figure 4-3(c) show that the WSS distribution at peak systole. The

average WSS is 11.24Pa and 9.93Pa respectively at peak systole in the rigid and elastic models. The WSS distributions were almost the same in the aneurysm between the two models. The WSS in the neck of the elastic model was a little larger than that in the rigid model. These could be explained by the wall deformation of the aneurysm indicated in [Figure 4-3\(d\)](#). Firstly, due to the expansion of the elastic wall while keeping the same total flow rate, the average WSS in elastic model was 11.65% smaller than that in the rigid model, which approximately agreed with our previous research. Secondly, the maximum deformation was about 0.4mm in the middle of the aneurysm. Thirdly, the elastic wall did not obviously affect the WSS distribution in the aneurysm since there was not much interaction between the fluid and the wall for Model A. The maximum WSS occurred in the neck, but the wall deformation is small there. The maximum deformation is large in the body of the aneurysm, while the WSS value is relatively small. No significant difference could be found in the aneurysm including the bleb between the rigid and elastic models.

[Figure 4-4](#) depicts the hemodynamic factors at peak systole of the rigid and elastic models (aneurysm model B). As shown in [Figure 4-4\(a\)](#), the blood flowed into the aneurysm from the parent artery directly, leading to a concentrated inflow jet. The aneurysm was characterized with a centralized inflow jet, small impingement region and compound flow pattern, which suggests a high risk for rupture. The flow patterns between the rigid and elastic models were almost the same in the inlet and outlet vessels. But significant differences could be seen in the dome. More flow was observed in the dome of the flexible model due to the effect of the flexible wall. [Figure 4-4\(b\)](#) depicts the pressure distribution of the rigid and elastic models. This positive pressure gradient caused the blood to move forward. When a region with adverse pressure gradient appeared in the aneurysm, the fluid particles cannot penetrate too far into the region of increased pressure. So the flow separated, moved into the main stream. The separation occurs only in decelerated flow, considering the boundary layer equations. The peak systole pressure was mostly uniform in the aneurysm with an elevation in the dome. There was not much difference of the pressure distribution between the rigid and elastic models. However, a larger region of locally elevated pressure was observed in the dome of the rigid model than that in the elastic model, leading to the even less flow in the dome. [Figure 4-5](#) illustrates the WSS vectors at various flow phases for the model. A region of locally increased WSS was produced due to the concentrated inflow jets. The maximum WSS magnitude could be found in the body and top of the aneurysm in both models. The WSS pattern was quite complex in the whole aneurysm during a heartbeat. The direction and magnitude of WSS changed very quickly near the neck and dome during only 50ms due to the strong impingement of the flow. But the WSS vectors did not change so significant in the elastic model. The different WSS magnitude ranges observed in previous papers are believed to be related to the different Reynolds's numbers. The peak value of WSS in elastic model was much

smaller than that in rigid model, while the average value of WSS in elastic model was 6.9% smaller than that in rigid model, which are consistent with our previous conclusions.

4.4 Discussion

4.4.1 Summary

The previous FSI researches of aneurysms mainly focused on the elastic effect on the entire aneurysm rather than the aneurysm blebs. In the present research, we studied the influence of wall elasticity on the flow patterns and WSS in two patient-specific cerebral aneurysm blebs. Our results showed the flow patterns were not remarkably changed due to the elastic effect, which agrees with the conclusions of other papers ([Tada and Tarbell, 2005](#); [Torii et al. 2007](#); [Bazilevs et al. 2010](#)). However, the elastic wall could have a great influence on the WSS distribution around the dome and the neck of the aneurysm with a bleb. A larger region of locally elevated pressure and even less flow in the dome, strong variation of WSS vectors were observed in the rigid model. In contrast, the WSS vector changes were not so strong in the elastic model. But these results may not be universal due to its dependence on the geometry of the patient specific aneurysm. More aneurysms will be included into the elastic effect analysis in future. Due to the significant differences in the impingement region which may related to the rupture of aneurysm, the fluid structure interaction should be incorporated into the analysis of flow fluctuation.

4.4.2 Limitations

There are potential limitations with this CFD simulation since an accurate and robust FSI simulation will be significantly influenced by the uncertain factors including modeling assumptions, boundary conditions, geometry construction, mesh design and so on. Firstly, for most CFD simulations of rigid models, flow rate measured by MRI or Doppler Ultrasound was performed as inlet boundary conditions, while traction-free boundary conditions were usually employed at outlets. But the pressure wave is required in order to consider the realistic deformation of the aneurysm, while the measurement of pressure is difficult in clinic. Secondly, it is also quite difficult to get the accurate distribution of wall thickness. In our study, we got the pressure wave from the human cardiovascular system. The modeling approximations are always key factors in CFD simulation and they became more complicated in the study of an elastic model since accurate patient-specific pressure wave and wall thicknesses were not available from clinical measurement. We consider these approximations of the elastic model as much as possible, but it still needs further research. FSI have already been performed to consider the interaction between. But it is still challenging since lack knowledge about the accurate pressure wave, wall elasticity and wall thicknesses. The wall elasticity of artery wall has the great effect

that damps the change of WSS especially at the neck of the aneurysm. These studies showed that the primary flow patterns were not remarkably changed by the elastic effect.

4.5 Conclusion

To develop a better understanding of aneurysm wall degradation, we carried out a numerical study of FSI on two typical cerebral aneurysms with blebs. For the second model where the flow impinged the aneurysm wall strongly, the wall elasticity has great effect on the flow patterns and WSS variation in the bleb, which could be importance in understanding the mechanism of the aneurysm rupture.

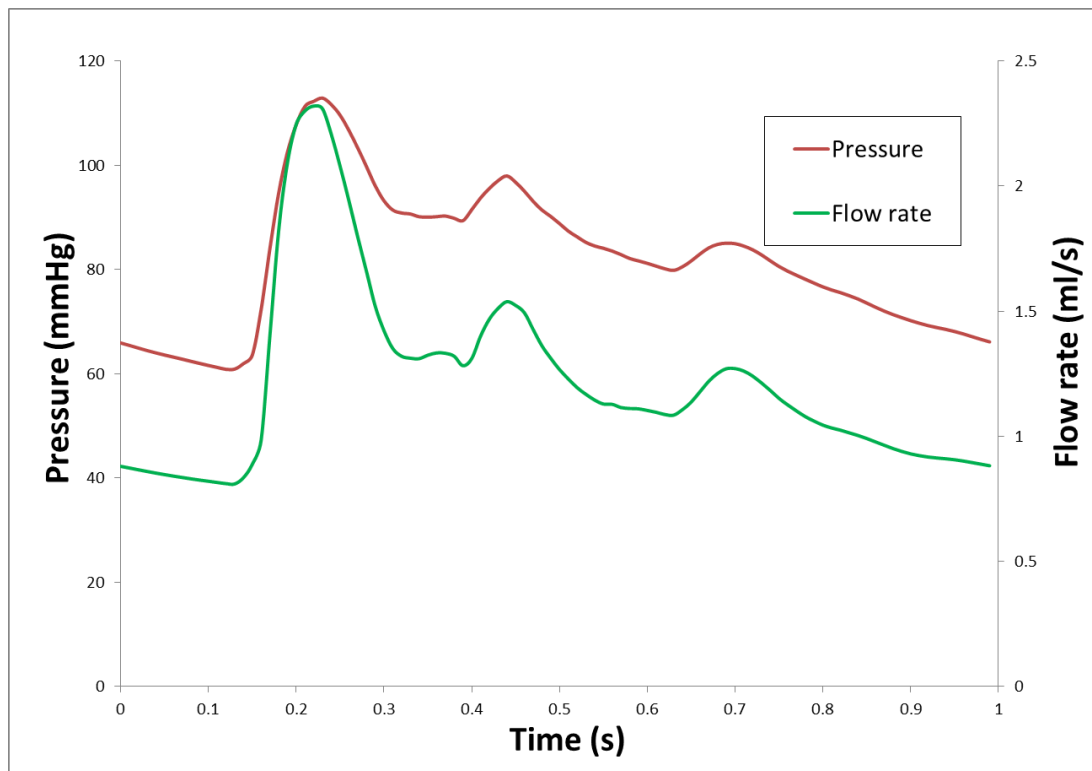


Figure 4-1. Boundary conditions the model. Pressure (Red line) and flow rate (Green line) waveforms at the inlet and outlet are based on our multi-scale modeling of the human cardiovascular system, and then adjusted to fit the mean value measured by MRI.

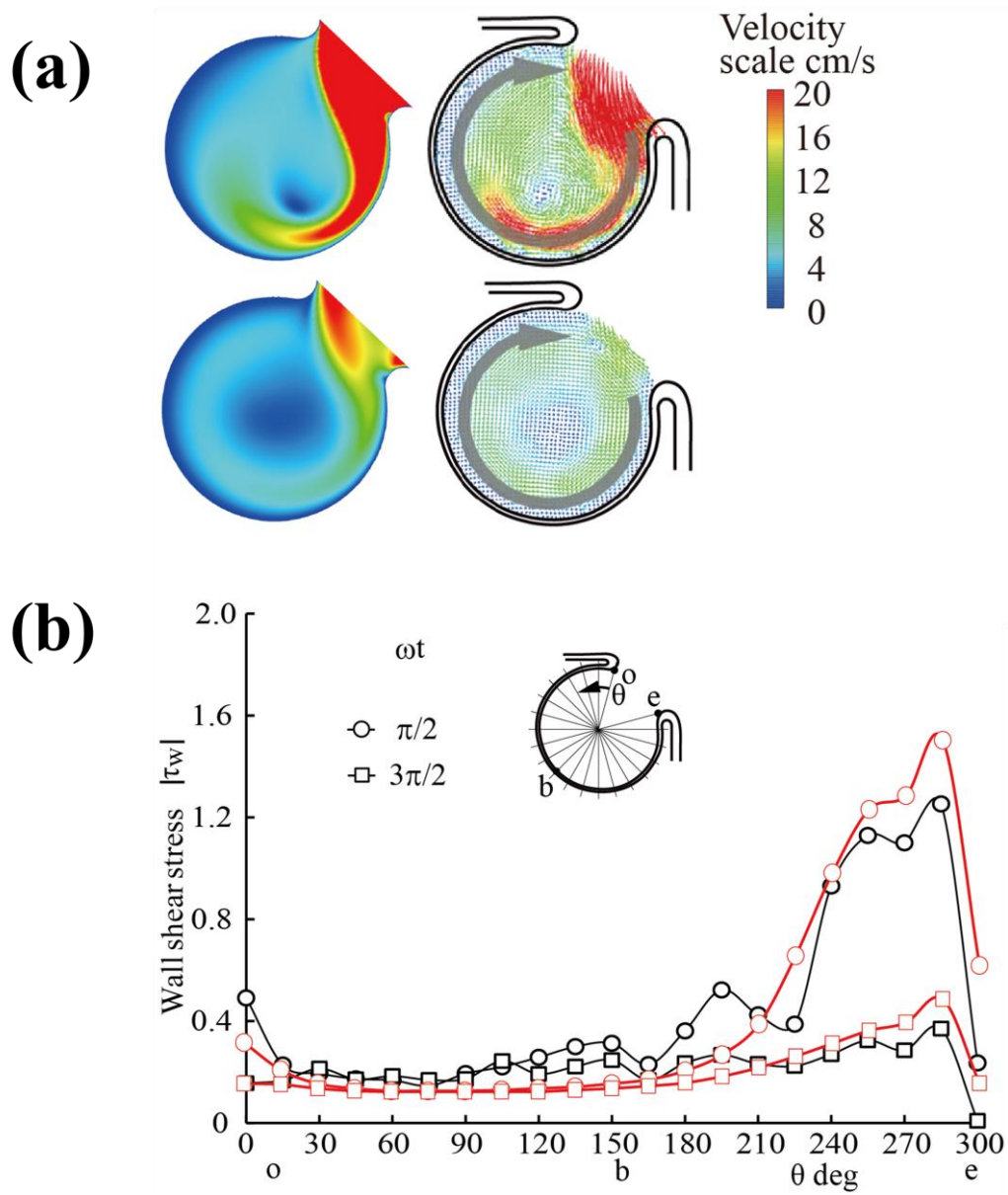


Figure 4-2. (a) The Velocity vector and in the middle plane within the aneurysm ($Re_m = 435$, $\alpha = 4.0$). Top row shows CFD and PIV results at peak systole, and bottom row shows CFD and PIV results at peak diastolic. (b) Wall shear stress along wall inside elastic aneurysm. The red and black lines indicate the CFD and PIV results respectively.

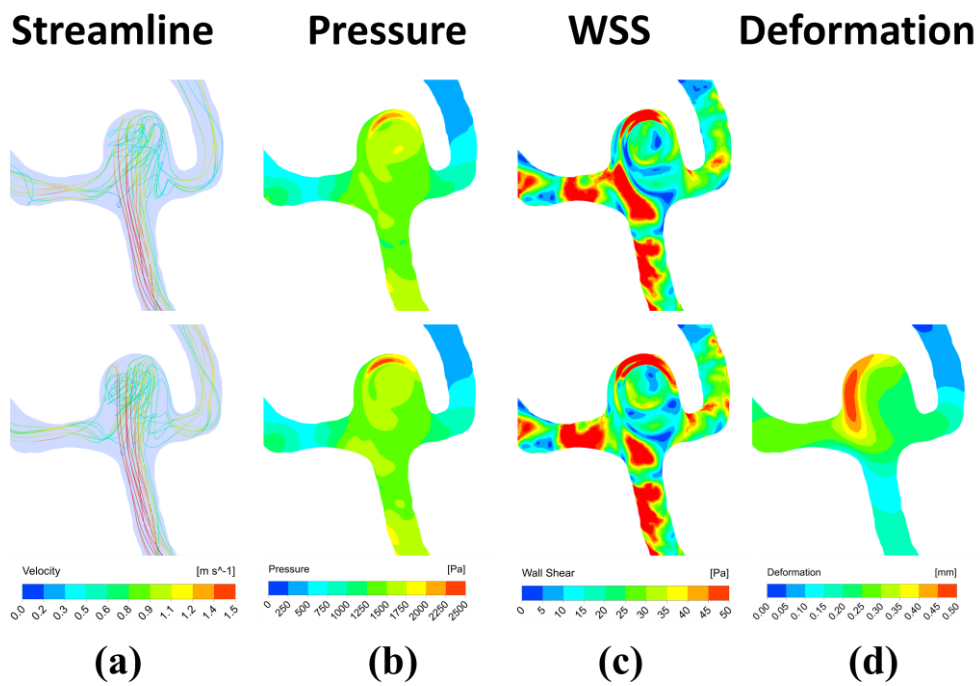


Figure 4-3. Visualization of WSS of the Rigid (Upper) and Elastic model (Lower) in Cerebral Aneurysm Model A. (a) instantaneous Streamline. (b) Pressure. (c) WSS. (d) Deformation at peak systole, respectively.

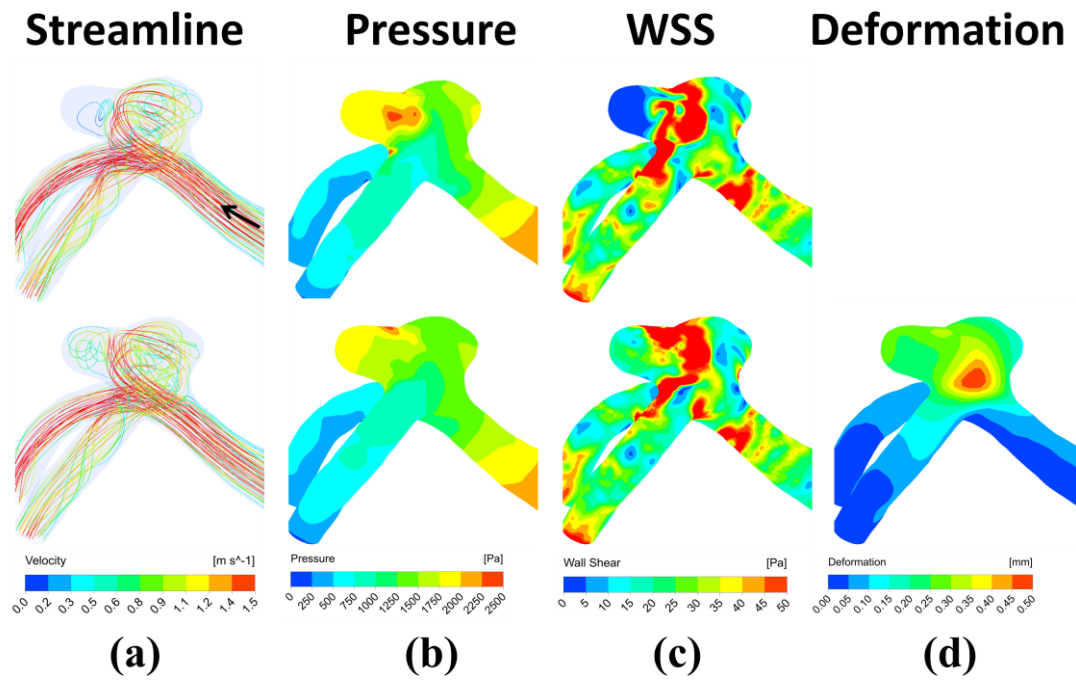


Figure 4-4. Visualization of WSS of the Rigid (Upper) and Elastic model (Lower) in Cerebral Aneurysm Model B. (a) instantaneous Streamline. (b) Pressure. (c) WSS. (d) Deformation at peak systole, respectively.

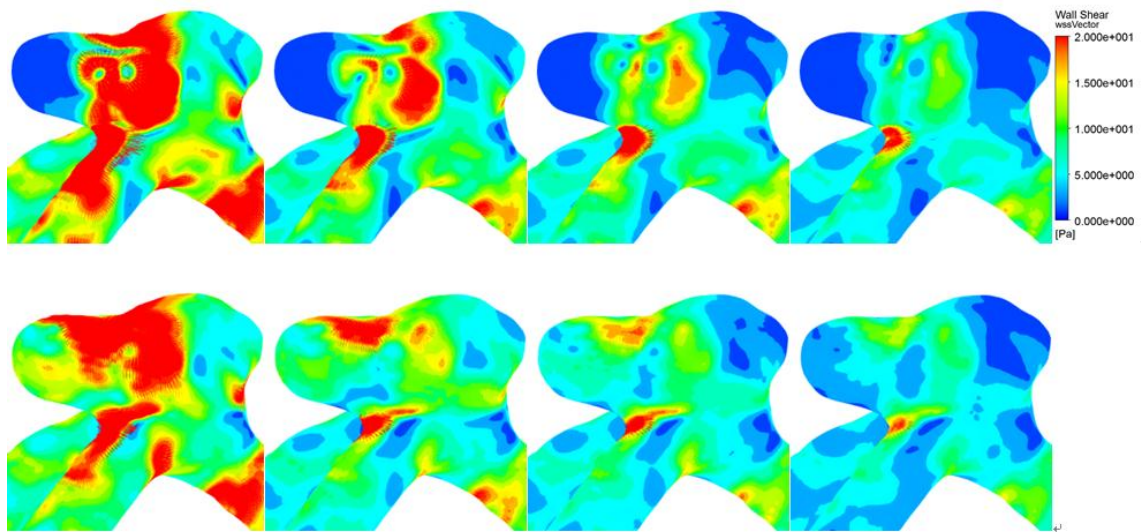


Figure 4-5. WSS vectors of the Rigid (Upper) and Elastic (Lower) model at four phases: (a) peak systole, (b) middle deceleration phase, (c) the second peak systole, (d) diastole.

5 Exploring potential associations between flow instability and rupture in patients with matched-pairs of ruptured-unruptured intracranial aneurysms

5.1 Introduction

A cerebral aneurysm is a protruding sac like a blood-filled balloon in the wall of which developed in specific cerebrovascular sites. The most severe outcome of cerebral aneurysm is the rupture and intracranial subarachnoid hemorrhage (SAH), causing a high mortality rate. Multiple intracranial aneurysms are observed in 15% to 35% of patients with aneurysms who suffered an SAH ([Juvela et al., 2000](#); [Kaminogo et al., 2003](#); [Lu et al., 2013](#)). For SAH patients with multiple aneurysms, it is very important for the medical team to determine which one causes SAH. The misdiagnosis is threatening since the unsolved but ruptured aneurysm could rupture again ([Hino et al., 2000](#); [Suarez et al., 2006](#)). For patients without SAH, it is also vital to predict which aneurysms are prone to rupture and whether an operation is necessary or not. However, prediction of rupture status in patients with multiple cerebral aneurysms remains challenging for clinicians.

Hemodynamic factors, particularly wall shear stress (WSS), could be of great importance in understanding the onset, progress and rupture of aneurysms. The onset of cerebral aneurysms is believed to be associated with the high WSS ([Dolan et al. 2008](#)). However, both high-WSS and low-WSS theories have been proposed to explain the rupture of cerebral aneurysms ([Cebral et al., 2011](#); [Xiang et al., 2011](#)). [Xiang et al. \(2011\)](#) carried out statistical analysis on 38 ruptured and 81 unruptured cerebral aneurysms and proposed that relatively low WSS and high oscillatory shear index (OSI) correlated with aneurysm rupture. On the contrary, [Cebral et al. \(2011\)](#) correlated the Maximum WSS with aneurysm rupture from study of 210 cerebral aneurysms. It is still unclear whether the complicated rupture mechanism or different experiment designs (small sample size, inconsistent parameter definitions and simplified model assumptions) lead to the controversy results. Recently, flow instability-related studies in vessels and aneurysms have been carried out experimentally and numerically for a better understanding of the rupture mechanisms ([Ferguson, 1970](#); [Steiger and Rulén, 1986](#); [Valen-Stenstad et al., 2011](#); [Varble et al., 2016](#); [Yagi et al., 2013](#)). [Baek et al. \(2010\)](#) investigated the flow instabilities and oscillatory behavior of WSS on three patient specific aneurysms of the internal carotid

artery (ICA) and demonstrated the presence of low-frequency-fluctuations were geometry-specific as aneurysm models showed pronounced fluctuations at different Reynolds numbers. [Ford and Piomelli, \(2010\)](#) studied the flow instabilities and found high-frequency-fluctuations in the idealized basilar aneurysm models and two of the four patient specific terminal basilar tip aneurysm models. [Valen-Stenstad et al. \(2011\)](#) reported the high-frequency flow fluctuation in certain terminal aneurysms and it could also take place in the sidewall aneurysms if the siphon is included in the geometry.

Although much progress has been made on unveiling the rupture indicator of aneurysms, how the flow instability associated with the rupture mechanism still remains poorly understood. In this study, computational fluid dynamic (CFD) simulations of two matched-pairs of anatomically realistic ruptured-unruptured cerebral aneurysms were performed under pulsatile flow simulations. We aim to observe the hemodynamic differences between matched pairs of ruptured-unruptured aneurysms and explore whether flow instabilities might be associated with the rupture mechanism.

5.2 Methods

5.2.1 Geometry and mesh

We focused on the multiple cerebral aneurysms with distinct rupture condition in the same patient from the open Aneurisk database. The matched ruptured-unruptured aneurysms in this present study could be a reasonable comparative model for exploring potential indicator for aneurysm rupture since sharing the same inflow rate waveform for the paired aneurysms in one patient could help control the individual differences. All the aneurysm models from the repository were reviewed for minimize selection bias. The informed consent was achieved for the use of diagnosis and clinical purpose from the involved patients. We obtained four cerebral aneurysms from two patients as shown in Figure 1. The first patient developed two aneurysms at the middle cerebral artery. One of them is located in the upstream MCA and the other aneurysm is downstream with a short distance. The second patient developed two aneurysms with one located in the anterior communicating artery (ACA) and the other one in the MCA. The following geometric parameters were computed: maximum diameter of aneurysm sac (D_{max}); average diameter of the ostium plane (D_{ostium}); aspect ratio as the ratio between aneurysm height over ostium diameter; size ratio computed as the sac maximum height over the parent vasculature diameter. The details of demographic and morphological parameters of the four cerebral aneurysms are shown in [Table 1](#). The geometries of the cerebral aneurysms and vessels were extracted using the gradient-based level set segmentation algorithm from the Vascular Modeling Toolkit (VMTK) ([Antigal et al. 2008](#)). The reconstructed model was then smoothened by VMTK's Taubin filter. We included the

vessel geometry features as much as possible and extended the outlets by 10 diameters to decrease the boundary artifacts. Unstructured grids consisted of tetrahedral and prism elements were produced with the minimum element size of 0.025 mm and maximum element size of 0.1 mm in ANSYS ICEM 15.0. The total element numbers ranged from 8 to 16 million elements in the meshes. Three prism layers were used to solve near-wall regions.

5.2.2 Boundary conditions

At the inlet we imposed full developed Womersley velocity profiles based on a flow rate waveform obtained from (Baek et al. 2010) having a cycle-averaged flow rate of 245 ml/s and a period of 0.75s, such as

$$V(r, t) = V_0 \left[1 - \left(\frac{r}{R} \right)^2 \right] \left\{ 1 + A \sum_{n=1}^N (a_n \cos(n\omega t) + b_n \sin(n\omega t)) \right\} \quad (3-1)$$

where the constant term V_0 represents the average velocity, A the amplitude factor ($A=1$), N the number of harmonics ($N=7$), and ω the angular frequency. The pairs of a_n and b_n normalized by V_0 are (-0.152, 0.129), (-0.111, -0.031), (0.043, -0.086), (0.028, 0.028), (0.002, 0.010), (-0.027, 0.012), (-0.0005, -0.026). A heart rate of 80 beats/minute was employed with a cardiac cycle duration of 0.75 s. As shown in Figure 5-2, a mean flow rate of 245 ml/min was imposed at the inlet and scaled with vessel diameter based on a power law model assuming the flow rate scales with cross-sectional area (Valen-Sendstad et al. 2015). The pulsatility index (PI) in the flow rate is 1.435. The Reynolds number is defined as $Re = uD/\nu$, where u denotes the inflow velocity, D the vessel's diameter, and ν the kinematic viscosity of the fluid. The Womersley number is defined by $R\sqrt{\omega/\nu}$, where R represents the vessel's radius and ω the angular frequency. The blood density and kinematic viscosity is 1025 kg/m³ and 3.5×10^{-6} m²/s, respectively. The average Reynolds numbers of patients A and B are 354 and 397 respectively. At outlets the traction-free boundary conditions were imposed. On vessel surfaces we assumed that the compliant wall-induced deformation is negligible and hereby employed the non-slip conditions.

5.2.3 Computational fluid dynamic modeling

The blood fluid is controlled by the unsteady and incompressible three-dimensional Navier-Stokes equations.

$$\frac{\partial u_i}{\partial x_i} = 0 \quad (3-1)$$

$$\frac{\partial u_i}{\partial t} + u_j \frac{\partial u_i}{\partial x_j} = \frac{\partial P}{\partial x_i} + \nu \frac{\partial^2 u_i}{\partial x_j^2} \quad (3-2)$$

Where u_i is the velocity component in the direction x_i ($i, j = 1, 2, 3$), P the pressure. Transient flow simulations were carried out with CFX 15 (ANSYS), which utilizes an element-based finite volume method (FVM) to discretize in space. The convergence criteria for iterative errors were set to be of 10^{-4} . No turbulence model was applied due to the relatively low Reynolds number in this study. The simulations (nine cardiac cycles) required approximately 44 hours of CPU time on a PC with an Intel Xeon (2.9GHz); parallel computing on a cluster with 32 nodes was carried out with Platform Computing. All the simulations were conducted up to nine cardiac cycles and the computed data of the last six cycles were employed for further analysis.

To evaluate whether the flow was correctly resolved, the spatial and temporal resolutions were assessed by computing the viscous length l^+ and time scale t^+ , such as

$$l^+ = \frac{u_* d_x}{\nu} \quad (3-3)$$

$$t^+ = \frac{u_*^2 d_t}{\nu} \quad (3-4)$$

$$u_* = \sqrt{\nu s_{ij}}, \quad s_{ij} = 0.5 \left(\frac{\partial u_i}{\partial x_j} + \frac{\partial u_j}{\partial x_i} \right) \quad (3-5)$$

Where u_* is the friction velocity at the vessel wall, d_x the maximum element size, d_t the time step, s_{ij} the fluctuating component of strain rate. In our simulation, l^+ and t^+ are on the order of 1. We did not try to resolve the all the temporal-spatial scales of the flow, but rather the scales with the primary energies. High-resolution simulations were performed to minimize artificial diffusion and capture the correct flow states.

5.2.4 Shear forces and kinetic energy

Based on the computed spatiotemporal WSS distributions, Oscillatory Shear Index (OSI) was further calculated to describe the oscillatory feature of the WSS vector, such as

$$OSI = 0.5 \left(1 - \frac{\left| \int_0^T \overline{WSS} dt \right|}{\int_0^T |\overline{WSS}| dt} \right) \quad (3-6)$$

where $0 < OSI < 0.5$ with a value of 0 being no variation of the WSS vector, and of 0.5 being 180° deflection of the WSS direction.

An instant velocity $u_i(x, t)$ was decomposed into averaged $\overline{u_i}(x, t)$ and fluctuating $u'_i(x, t)$ components ($i = 1, 2, 3$),

$$u_i(x, t) = \overline{u_i}(x, t) + u'_i(x, t) \quad (3-7)$$

We defined fluctuating kinetic energy (FKE) such as:

$$FKE(x, t) = \frac{1}{2} < u'_i(x, t) \cdot u'_i(x, t) > \quad (3-8)$$

5.3 Results

5.3.1 Flow patterns and hemodynamic factors

Figure 5-3 illustrates the streamline and velocity distributions in two multiple cerebral aneurysm models. It is seen that the blood flows inject into the aneurysm at a specific angle from the parent vessel, leading to one or multiple vortices inside the aneurysm. Models A1&B1 (unruptured) obviously show relatively stable flows with a single vortex whereas models A2&B2 (ruptured) present a complex feature of unstable flow patterns with multiple vortices and one recirculation zone at the blebs (red arrows). **Figure 5-4** shows the pressure distributions around stagnation regions (black arrows) are at a very high level, which leads to adverse local pressure gradients against the flow into the aneurysm. The local stagnation regions inside the aneurysm obviously correspond to low WSSs and high OSIs surrounded by high WSS regions. The ruptured aneurysms A2&B2 are exposed to high OSI and low WSS at the blebs, with high pressures and steep spatial WSS gradients in the stagnation regions.

5.3.2 Flow fluctuations and fluctuating kinetic energy (FKE)

Figure 5-5a-b illustrates the velocity distributions aligning with centerlines at peak systole of cerebral aneurysms. Complicated velocity profiles with multiple inflection points are found at the ICA (Points 1-5). The velocity fluctuations originate from the bends of the ICA siphon and get developed in the upstream regions of aneurysms (Points 5-12). The ruptured aneurysm A2 (Points 11-12) obviously presents more significant velocity fluctuations than the unruptured aneurysm A1 (Points 7-8) as shown in **Figure 5-5d**. On the other hand, model B shows few inflection points and no velocity fluctuations at the ICA (**Figures 5-6a-c**). The flow in the vessels of model B is very likely laminar and stable at the ICA but does exhibit significant fluctuations in the aneurysms. Note that the ruptured aneurysm B2 (Points 11-12) also show more pronounced velocity fluctuations than the unruptured aneurysm B1 (Points 7-8). **Figure 5-7a** demonstrates the highly oscillatory behavior of WSSs in time for models A1&A2. Six feature points were picked up at the entrance of the aneurysm and WSS divergence regions. There exist minor WSS fluctuations at feature points 13-15 in the unruptured aneurysm model A1. However, the time traces of feature points 16-18 apparently demonstrate pronounced WSS fluctuations in the ruptured aneurysm model A2, which are present initially at peak systole when the flow turns to decelerate, being enhanced throughout the late systole. As shown in **Figure 5-7b**, obvious discrepancies of WSS

fluctuations are also observed between model B1 (unruptured) and model B2 (ruptured): model B2 shows much more significant intra-cycle WSS fluctuations than model B1.

Figure 5-8a indicates the instantaneous WSS distributions during the deceleration phase for three consecutive heart cycles of model B2. Cycle-to-cycle differences are visible at peak systole, and substantially turn to be pronounced during the deceleration phase in the aneurysm model B2. Cycle-to-cycle fluctuations are slightly observed in the ruptured aneurysm A2, but no differences are found in the unruptured aneurysms A1&B1. **Figure 5-8b** illustrates the instantaneous velocity fields in two cutting planes of model B2. Different velocity distributions (black arrows) are observed in the aneurysm at late systole when the flow turns to decelerate in the ruptured aneurysm B2. No cycle-to-cycle fluctuations are found in the unruptured aneurysms A1&B1. To quantify the cycle-to-cycle fluctuations, we plot the averaged FKE measured at the feature points inside the aneurysms in **Figure 5-9**. Note that the peak FKE value of model B2 is much larger than that of model A2. We confirm the significant and slight cycle-to-cycle fluctuations in the ruptured model B2 and model A2, respectively. The flow in model A2 remains laminar until flow turns to decelerate and the peak FKE occurs 0.1-0.15s after peak systole (**Figure 5-9a**). **Figure 5-9b** also shows the time delay between the maximum FKE value and the maximum velocity. The peak FKE occurs at late systole in the ruptured aneurysm B2.

5.3.3 Geometry and inflow waveform effects on flow fluctuations

A constant inflow velocity of 0.31m/s was imposed at the inlets of models A&B to investigate the geometry effects on the flow instabilities. Here constant inlet boundary condition was employed but solving the transient Navier-Stokes equations since we aimed to prove the presence of flow instabilities independent of pulsatile flow dynamics ([Valen-Stendstad et al., 2013](#)). **Figure 5-10** illustrates that the initial transients quickly damp out and converge to a single solution for the unruptured aneurysm models A1&B1 (Points 7-8), whereas the ruptured aneurysm models A2&B2 (Points 11-12) demonstrates persistent velocity fluctuations. We further investigate whether the flow fluctuations arising in the upstream parent arteries (**Figures 5-5&5-6**) influences the intra-cycle and inter-cycle flow fluctuations in cerebral aneurysms. An extended CFD simulation was carried out with a truncated inlet instead of the segments of original ICA and almost the same velocity fluctuations were observed in the ruptured aneurysm B2. Next, the number of Fourier modes for the inflow waveform was reduced to examine the effects of the waveform shape on the flow fluctuations. It was found that the geometries of cerebral aneurysms, rather than the flow instabilities initiated in the upstream region of aneurysms or the shape of the inlet waveform, are the determining factors leading to the presence of the intra-aneurysm flow fluctuations in this study.

5.4 Discussion

Both high-WSS and low-WSS theories have been raised to illustrate the growth and rupture of cerebral aneurysms. However, the rupture mechanism is still little known. Our results demonstrated that the two ruptured aneurysms (models A2&B2) present a feature of complex unstable flow patterns with multiple vortices and one recirculation zone at the blebs, while models A1&B1 (unruptured) show relatively simple stable flows with a single vortex. Moreover, temporal WSS fluctuations are observed initially at peak systole when the flow decelerates, which are much more significant in the two ruptured aneurysms. The obvious differences observed between matched-pairs of ruptured-unruptured aneurysms imply that flow instabilities may be correlated with the rupture risk of aneurysms. Besides the intra-cycle fluctuations, it is interesting to find cycle-to-cycle fluctuations in the ruptured aneurysms when the flow turns to decelerate, which were also reported in (Ford et al., 2008; Valen-Stendstad et al., 2011). The flow fields associated with the ruptured aneurysms are likely highly disturbed flows near a transition point, which may be more damaging to the aneurysms than laminar flow. The simplified assumption of taking the hemodynamics of aneurysms as a laminar flow needs to be attentively considered.

A better comprehension of the pathological differences between the ruptured and unruptured cerebral aneurysms could help to explain the rupture mechanism. Kataoka et al. (1999) studied 44 ruptured and 27 unruptured cerebral aneurysms and observed the endothelial cells (ECs) in ruptured aneurysms were most likely damaged with disrupted arrangements, while majority of unruptured aneurysms were covered with regularly shaped arterial ECs. Frösen et al. (2004) also found that the ruptured aneurysms were characterized by loss of ECs. The ruptured aneurysms manifested significant endothelial damage and wall degeneration, which correlated to the oscillatory shear stress. The response of ECs exposed to shear stress has been investigated by varying the frequency, direction and gradient (Chappell et al., 1998; Himburg et al., 2007). Chappell et al. (1998) proposed that the oscillatory shear stress in vitro provided a proinflammatory stimulus to human ECs and suggested the ECs in vivo might be greatly affected by oscillatory shear stress. Himburg et al. (2007) investigated the frequency-dependence of the vascular endothelium to pulsatile shear stress and observed that the proinflammatory response caused by the relatively higher frequency was quite crucial under reversing and oscillatory shear. These studies in the area of cell biology support that the high-frequency WSS oscillations and rapidly changing direction of WSS, not the magnitude of WSSs alone, could have a great important effect on the life-cycle of the aneurysm. In this study, we observed that the ruptured aneurysms apparently present more significant intra-cycle and

inter-cycle WSS fluctuations than unruptured aneurysms in the same patient. WSS fluctuations with significant energy content introduce extra friction and transfer substantial energy to fluctuations. However, WSS fluctuations in the unruptured aneurysms may be present with a small loss of energy, which may not trigger excessive blood damages. [Qian et al. \(2011\)](#) previously also proposed that greater energy loss occurs when flow passes through ruptured aneurysms, compared with unruptured aneurysms. Our results suggest that WSS fluctuations may be of great importance in aneurysm rupture depending on the levels of the fluctuations.

Flow instability occurs under certain circumstances depending on geometrical configurations and inflow waveforms. With Figures 5&6 we look at whether there are flow fluctuations associated with the aneurysm and what is its nature by plotting the temporal velocities along the centerlines. The flow fluctuations of model A initially appear at the ICA siphon, whereas model B exhibit flow fluctuations till the upstream region of MCA, pointing to the importance of the geometry-dependence of the flow instabilities. We then prescribed a uniform inflow velocity with no fluctuating component at the inlets and found that velocity fluctuations still exist in the ruptured aneurysms A2&B2 rather than the unruptured aneurysms A1&B1 (Figure 10). On the other hand, inlet flow rate waveforms could also lead to the flow instability associated with cerebral aneurysms. We furthered investigated whether the flow fluctuations arising in the upstream parent arteries of aneurysms ([Figures 5&6](#)) and the shape of inflow waveform influence the flow fluctuations in cerebral aneurysms and found that they have little influence on the results. A conclusion reached in our previous studies is that the low-frequency harmonics very likely induce and dominate WSS fluctuations associated with the cerebral aneurysms, in particular during the decelerating phase at late systole, which corresponds with a steeper global and local pressure gradient ([Xu et al., 2016](#)). Cerebral aneurysm hemodynamics could be of some robustness, dependent mainly on the primary low-frequency harmonics initiated by heart contraction but insensitive to the unpredictable high-frequency perturbations in the inflow waveforms. Our results suggest that the geometries and low-frequency harmonics of the inlet waveform may be the primary determining factors leading to the presence of the flow fluctuations in cerebral aneurysms.

There are several limitations to this study. Our boundary conditions are not patient specific and the effects of reflections at outlets were not considered. The flow rate measured by MRI or Doppler Ultrasound should be obtained in future. The elastic effects on the flow instability are not considered since accurate pressure wave and wall thicknesses were not available from clinical measurement. However, the wall elasticity may to some extent influence the flow patterns in the cerebral aneurysm models ([Tada and Tarbell, 2005](#); [Lee et al., 2013](#)). Thirdly, the non-Newtonian effect may not be negligible in complex flows, although it is generally negligible in cerebral arteries in laminar flows due to its modest effect on flow patterns ([Lee and](#)

[Steinman, 2007](#); [Perktold et al., 1998](#)). The elastic and non-Newtonian effects on the hemodynamic factors and flow instabilities still need further research.

5.5 Conclusions

The present study investigated the hemodynamic factors and flow instabilities in two patients with multiple intracranial aneurysms. Our results demonstrated highly disturbed flows in the ruptured aneurysms, which are characterized by pronounced velocity and WSS fluctuations at systole when flow decelerates. The two ruptured aneurysms experienced much more significant temporal intra-cycle and inter-cycle WSS fluctuations than the other two unruptured aneurysms of the same patient, which suggests that flow instability may be related to aneurysm rupture.

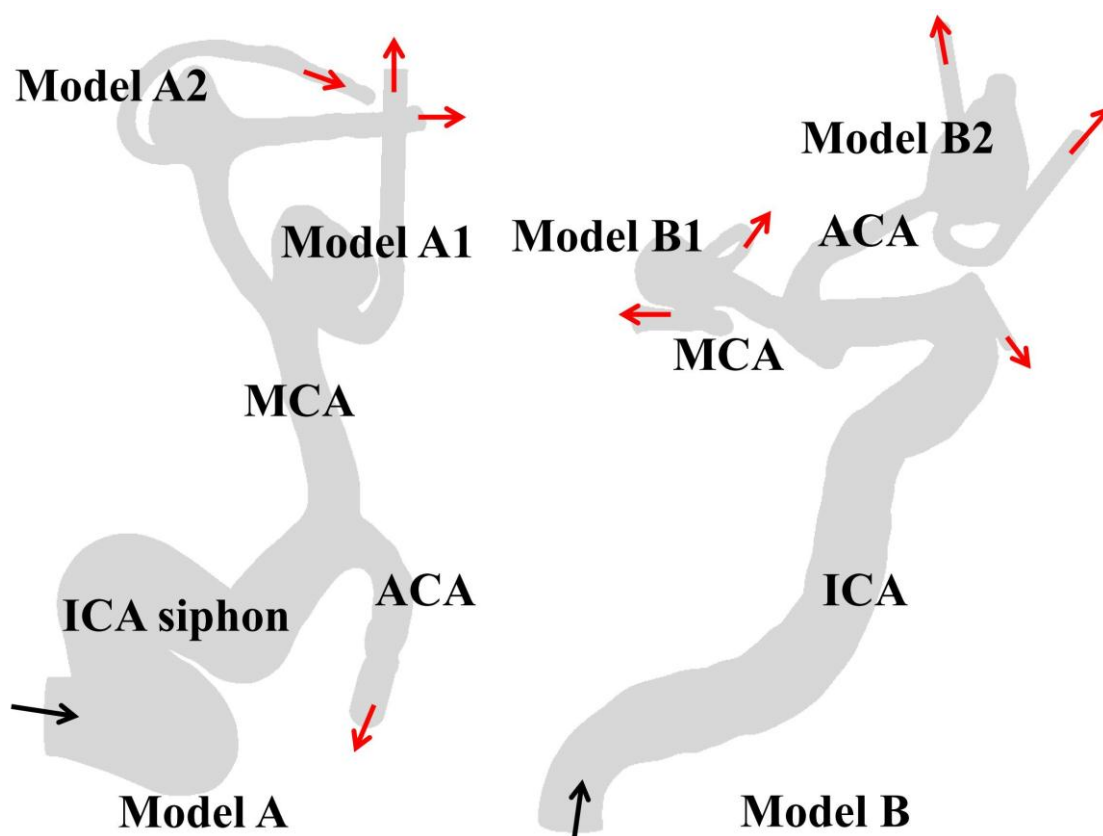


Figure 5-1. Four patient-specific cerebral aneurysm models in two pairs employed in simulations (unruptured aneurysms A1&B1, ruptured aneurysms A2&B2). Black and red arrows point to single inlets and multiple outlets, respectively.

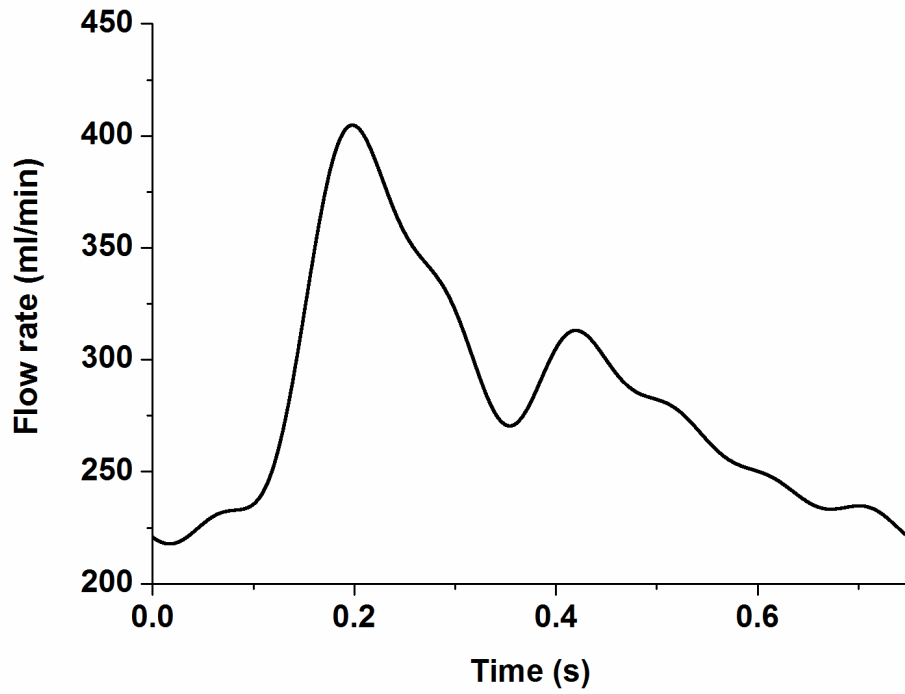


Figure 5-2. The inlet flow rate waveform over a cardiac cycle of model A with a mean velocity of 0.31 m/s.

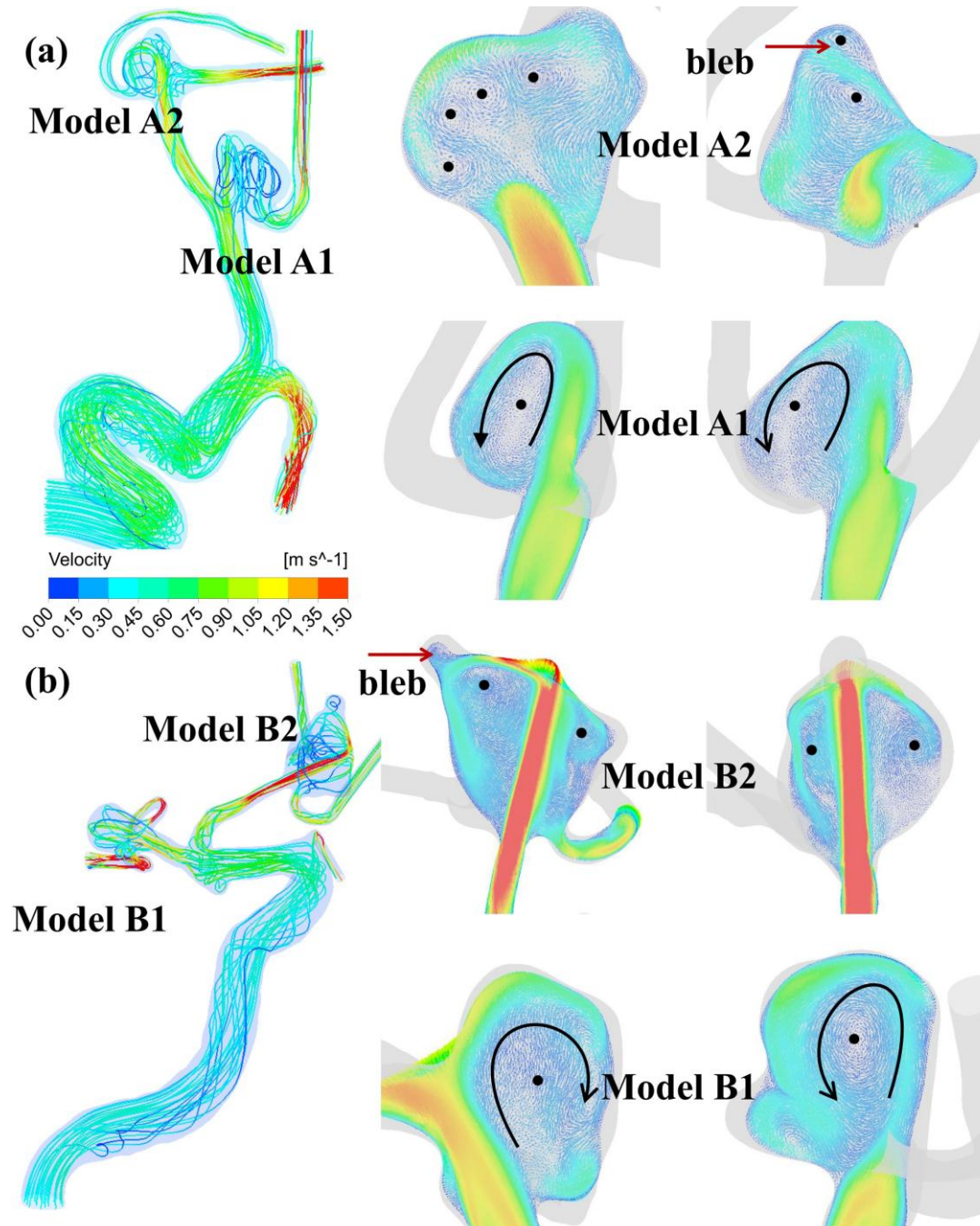


Figure 5-3. Visualized flow patterns at peak systole in two cutting planes for each aneurysm model. The black circles correspond to vortex cores and the red arrows point to the recirculating zones with slow flow due to flow separation at the blebs. Models A2&B2 present a more complex feature of unstable flow patterns with multiple vortices compared to models A1&B1.

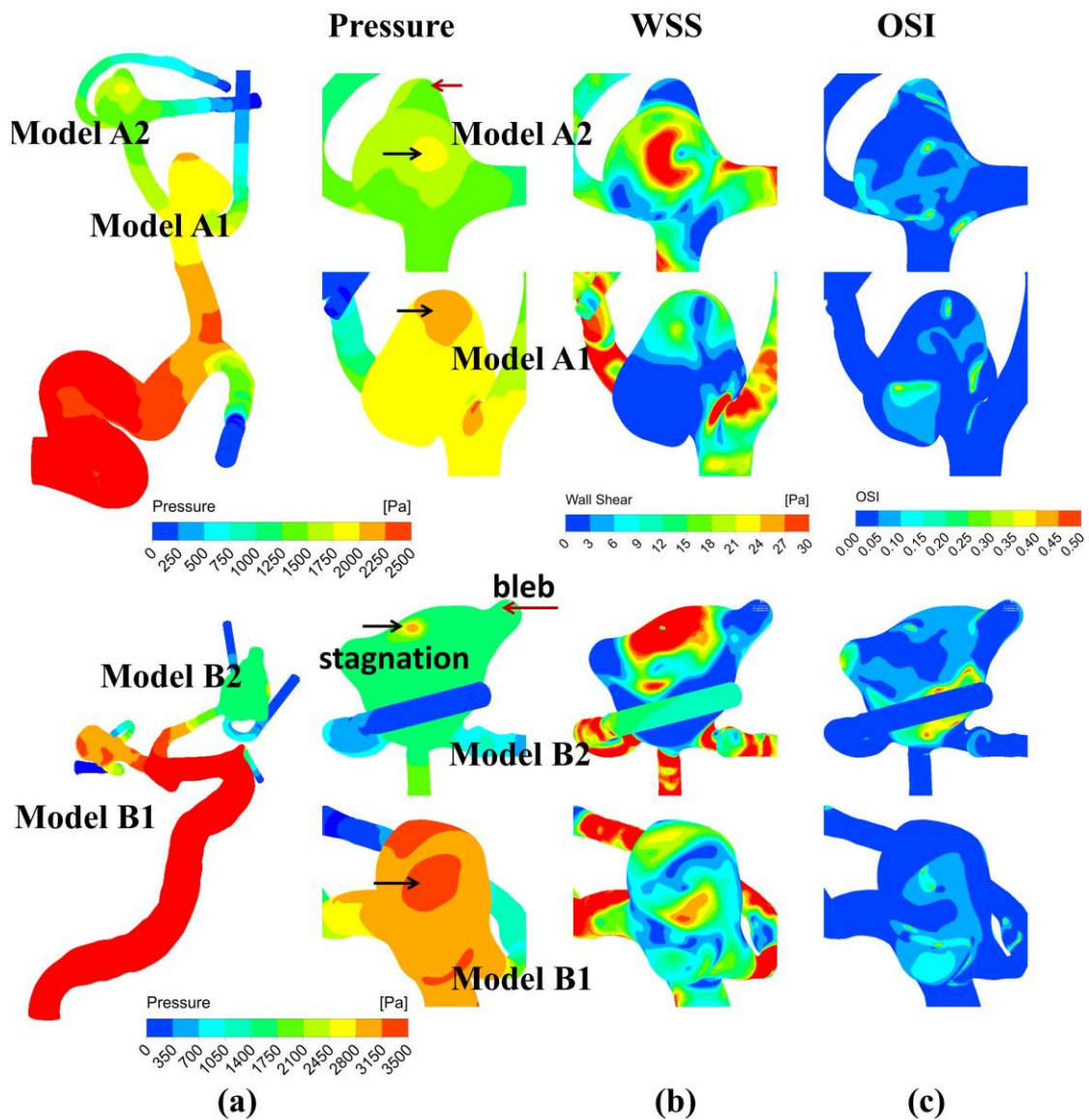


Figure 5-4. Distributions of pressures (a), WSSs (b) and OSIs (c) at peak systole for model A (upper) and model B (lower). Red and black arrows point to the recirculating zones at the blebs and the stagnation regions, respectively. There obviously exists a featured distribution of high OSIs and low WSSs at the blebs, with high pressures and WSS gradients in the two ruptured aneurysms A2&B2.

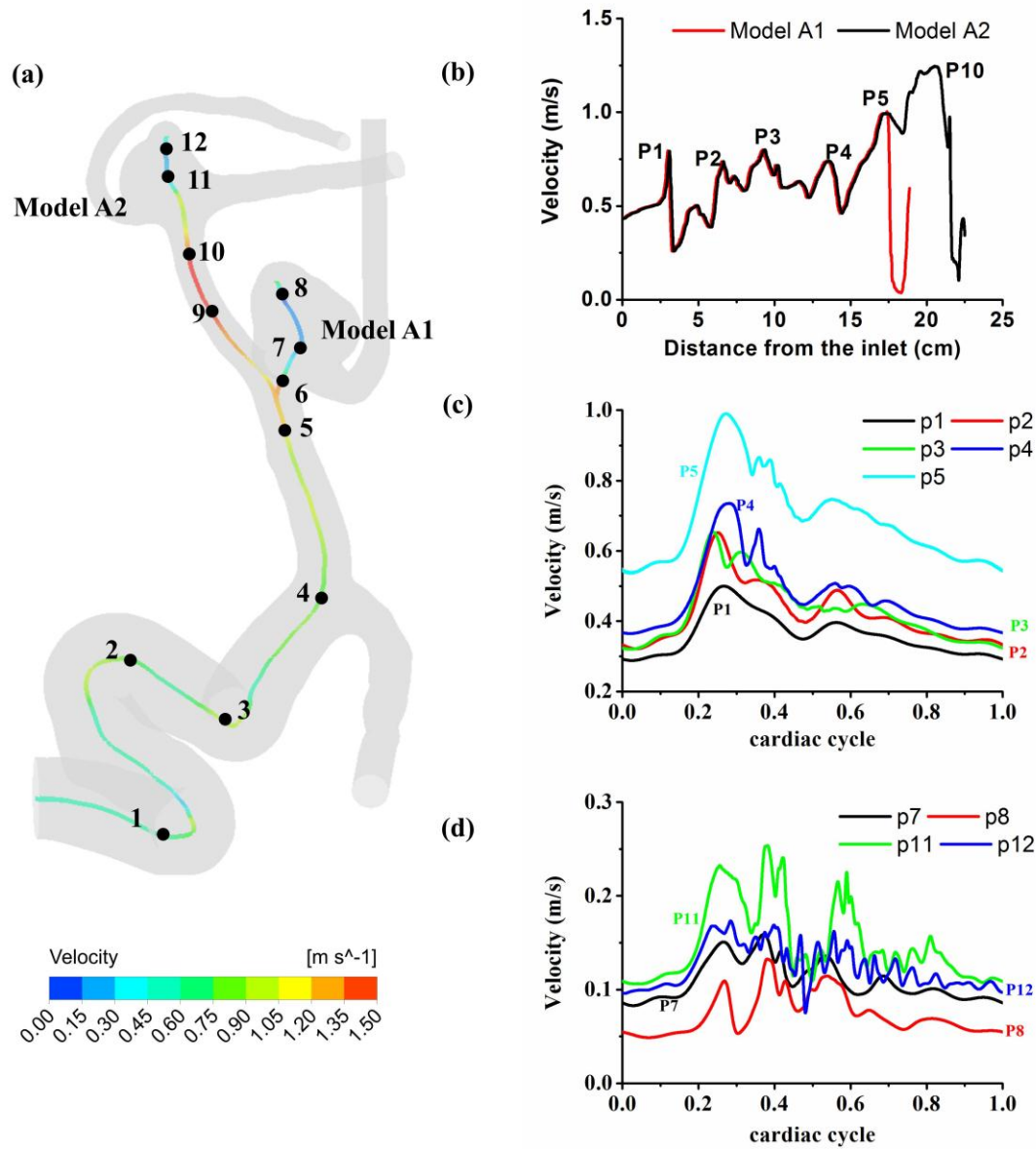


Figure 5-5. Velocity distributions aligning with centerlines at peak systole (a-b) and time-varying velocities at feature points for model A (c-d). Complicated velocity profiles with multiple inflection points are found at the bends of ICA siphon (Points 1-5). Velocity fluctuations are observed in the upstream arteries and aneurysm sacs. Note that the rupture aneurysm A2 (Points 11-12) exhibit more significant velocity fluctuations than unruptured aneurysm A1 (Points 7-8). The peak Reynolds numbers of the upstream parent arteries of aneurysms are calculated to be 627 and 554 for models A1 and A2, respectively.

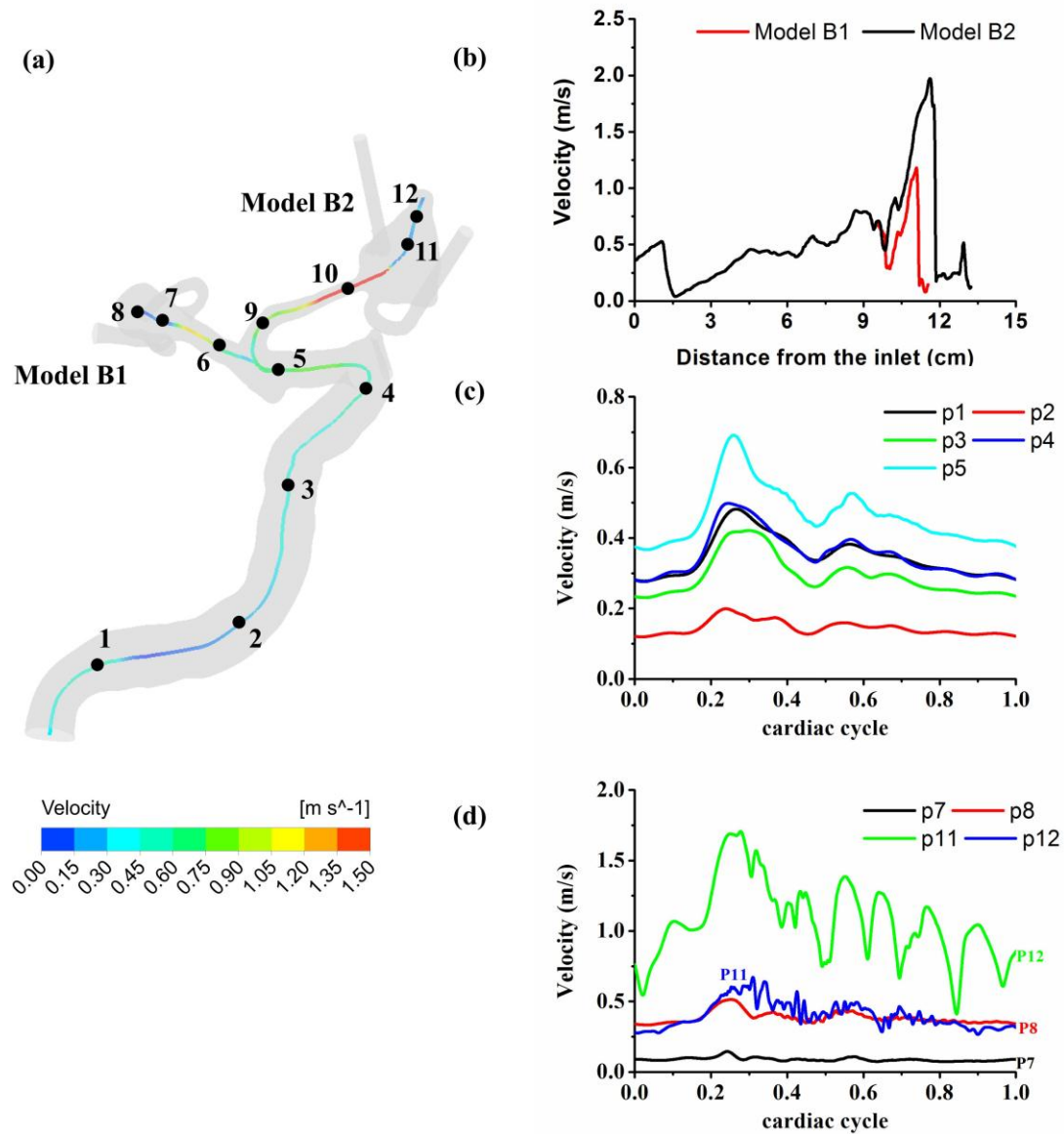


Figure 5-6. Velocity distributions aligning with centerlines at peak systole (a-b) and time-varying velocities at feature points for model B (c-d). Few inflection points and no velocity fluctuations are observed at the ICA siphon. The flow is very likely laminar and stable at ICA but does exhibit significant fluctuations in the aneurysms. Note that the rupture aneurysm B2 (Points 11-12) exhibit more significant velocity fluctuations than unruptured aneurysm B1 (Points 7-8). The peak Reynolds numbers of the upstream parent arteries of aneurysms are calculated to be 718 and 746 for models B1 and B2, respectively.

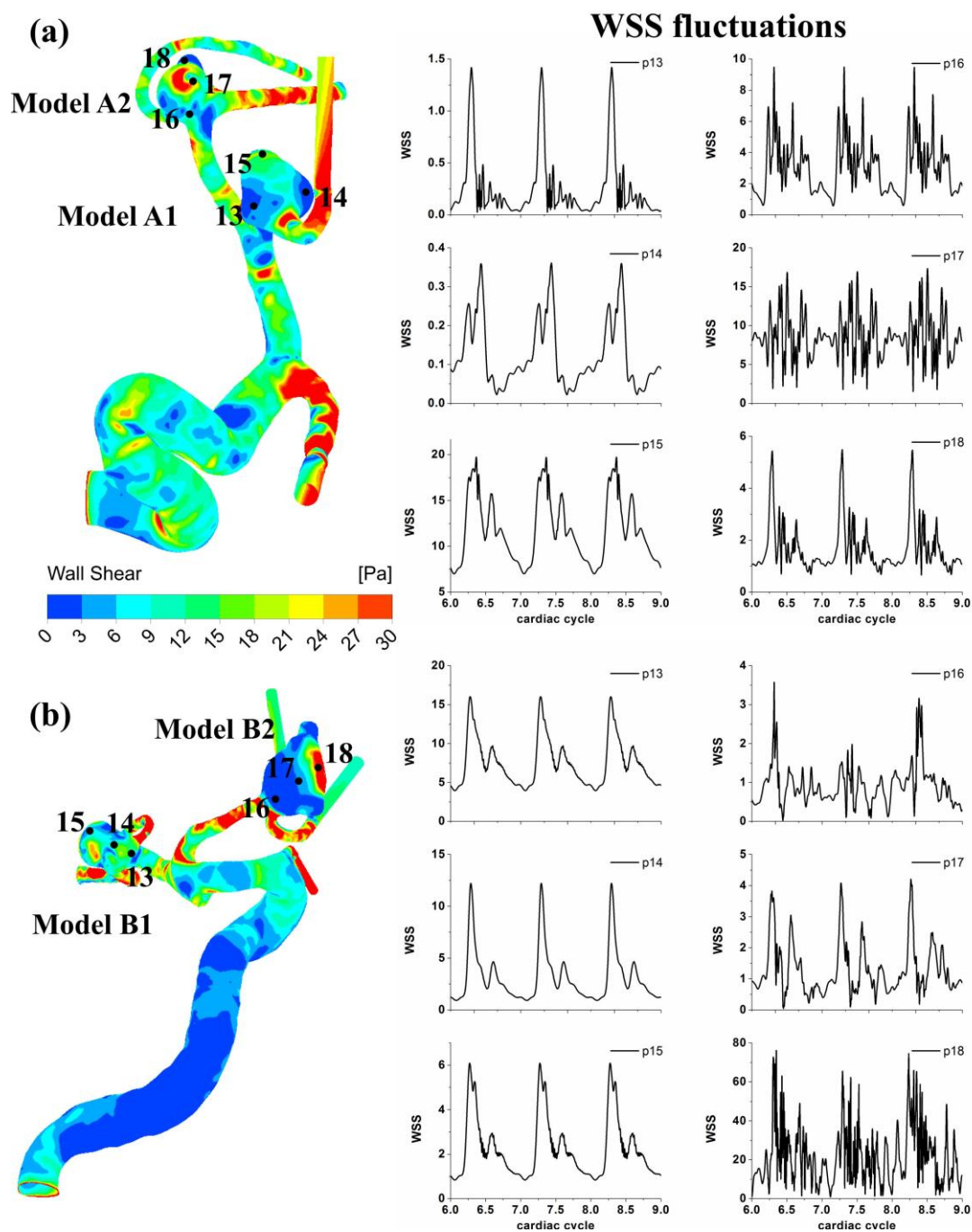


Figure 5-7. Time-varying WSSs at six feature points inside the cerebral aneurysms of model A (a) and model B (b). The ruptured aneurysms A2&B2 apparently present more significant WSS fluctuations rather with the unruptured aneurysms A1&B1 do.

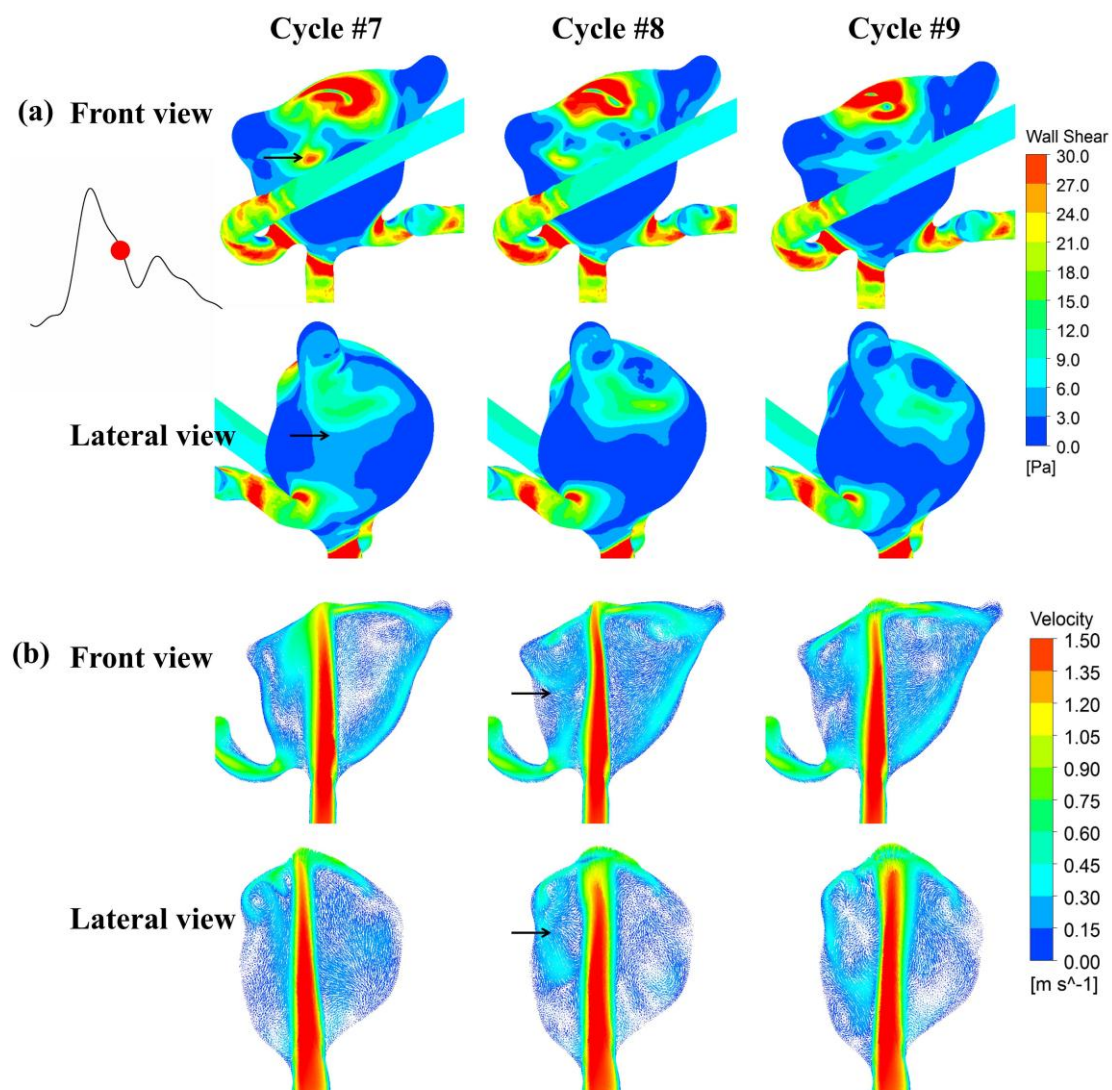


Figure 5-8. WSS distributions (a) and velocity fields in two cutting planes (b) at an instant of deceleration phase for three consecutive heart cycles (model B2). Black arrows point to the cycle-to-cycle differences of the flow patterns and WSS distributions during the deceleration phase.

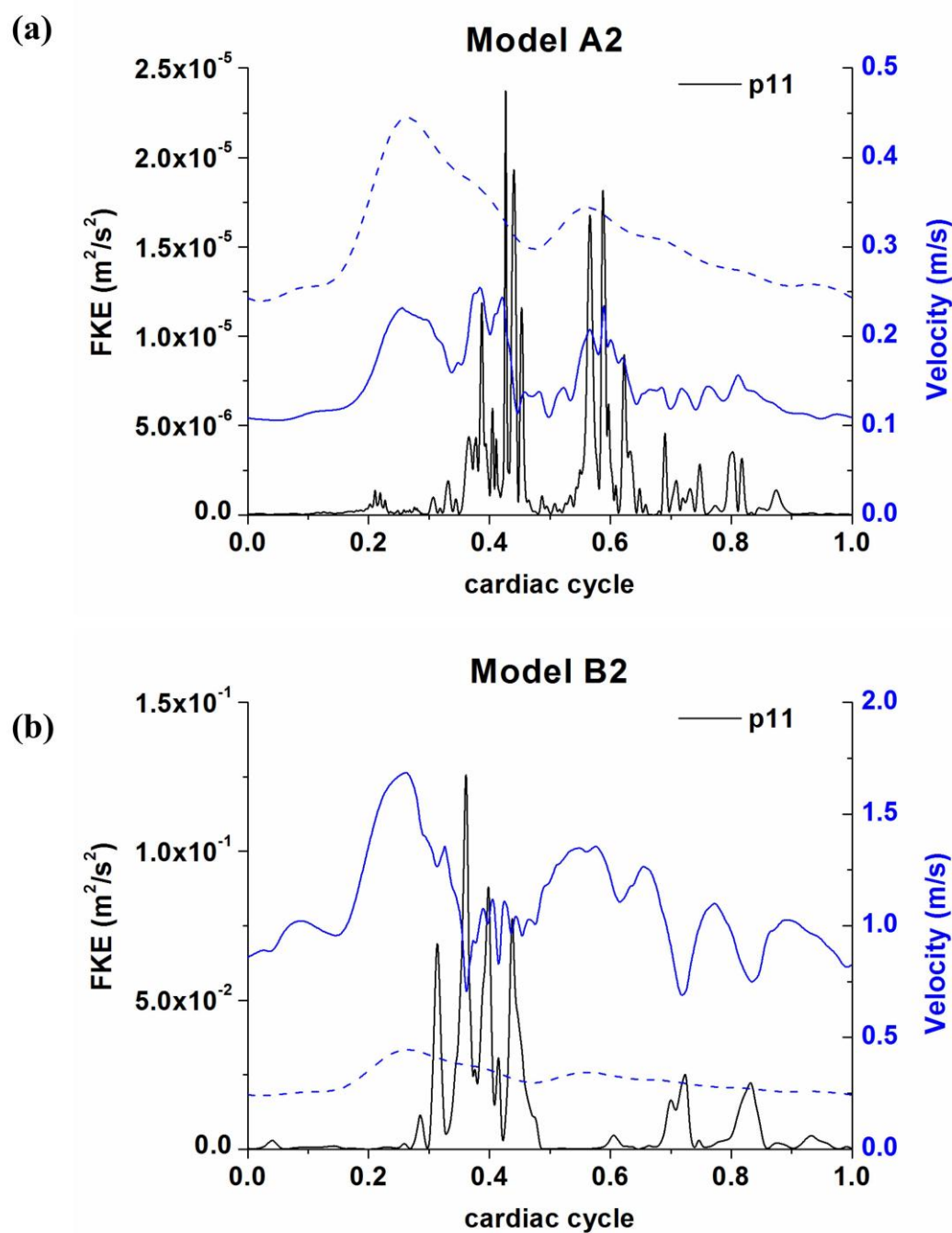


Figure 5-9. Average fluctuating kinetic energy (FKE) in model A2 (a) and model B2 (b). The blue solid and dashed lines show the time varying velocities at feature points inside aneurysms and inlets as reference, respectively. An obvious FKE peak is observed when flow turns to decelerate at late systole.

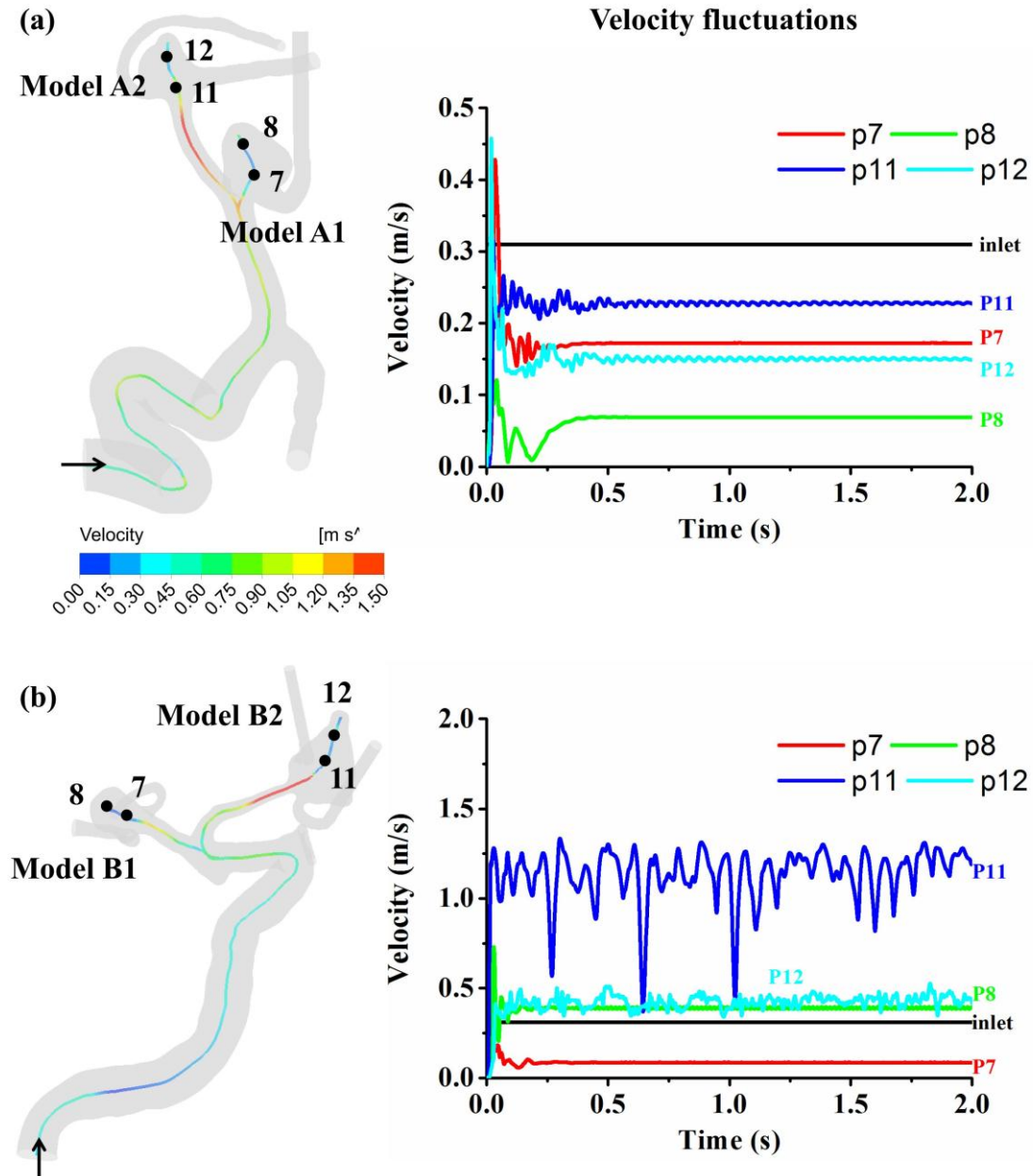


Figure 5-10. Time-varying velocities at feature points for model A (a) and model B (b). A constant inflow velocity of 0.31 m/s with no fluctuating components was employed at the inlets to prove the presence of flow instabilities independent of pulsatile flow dynamics. The ruptured aneurysms A2&B2 (Points 11-12) exhibit consistent velocity fluctuations whereas unruptured aneurysms A1&B1 (Points 7-8) converge to a single solution.

Model	Age	Sex	Location	Status	D_{max} (mm)	D_{ostium} (mm)	Aspect ratio	Size ratio
A1	77	F	MCA	Unruptured	6.43	5.24	0.97	2.57
A2	77	F	MCA	Ruptured	4.80	4.46	0.78	2.38
B1	71	M	MCA	Unruptured	6.81	5.48	0.93	2.92
B2	71	M	ACA	Ruptured	8.69	4.68	1.69	5.93

Table 5-1. Demographic, morphologic parameters and flow characteristics of the four cerebral aneurysms.

6 Statistical analysis of flow instability related to aneurysm rupture on thirty-five aneurysms at the internal carotid artery

6.1 Introduction

Cerebral aneurysms are cerebrovascular protruding sacs like blood-filled balloons that develop in specific cerebrovascular sites. The most severe consequence of cerebral aneurysm is the rupture and intracranial subarachnoid hemorrhage (SAH), causing a high mortality rate. It is vital to predict which aneurysms are prone to rupture and whether an operation is necessary or not. However, prediction of rupture status of cerebral aneurysms remains challenging for clinicians. Hemodynamic factors, particularly wall shear stress (WSS)-related ones, could be of great importance in the onset, progress and rupture of cerebral aneurysms. The onset of cerebral aneurysms is believed to be associated with the high WSS ([Dolan et al. 2008](#)). However, there is still a controversy associated with the reasons of the progress and rupture of aneurysms. Both high-and low-WSS mechanisms have been proposed from different viewpoints to explain the progress and rupture of cerebral aneurysms ([Cebal et al., 2011](#); [Jou et al., 2008](#); [Xiang et al., 2011](#)). [Jou et al. \(2008\)](#) performed a CFD study of eight ruptured and 18 unruptured ICA aneurysms and proposed that LSA could significantly separate the ruptured and unruptured aneurysms. [Xiang et al. \(2011\)](#) carried out statistical analysis on 38 ruptured and 81 unruptured cerebral aneurysms and proposed that low WSS and high oscillatory shear index (OSI) correlated with aneurysm rupture. On the contrary, [Cebal et al. \(2011\)](#) correlated the Maximum WSS with aneurysm rupture from study of 210 cerebral aneurysms. It is still unclear whether the complicated rupture mechanism or different experiment designs (small sample size, inconsistent parameter definitions and simplified model assumptions) lead to the controversy results. Other rupture indicators besides WSSs were also proposed for a better understanding of the rupture mechanisms. [Qian et al. \(2011\)](#) performed CFD on four ruptured and 26 unruptured cerebral aneurysms and proposed that greater energy loss occurs when flow passes through ruptured aneurysms, compared with unruptured aneurysms. [Takao et al. \(2012\)](#) studied 50 sidewall aneurysms at internal carotid posterior communicating artery aneurysms and 50 terminal aneurysms at middle cerebral artery with CFD and demonstrated that pressure loss coefficient may be associated with aneurysm rupture. Recently, flow instability-related studies in vessels and aneurysms have been carried out experimentally and numerically and may also correlate to

aneurysm rupture (Ferguson, 1970; Steiger and Rulen, 1986; Valen-Stenstad et al., 2011; Varble et al., 2016; Yagi et al., 2013).

The rupture mechanism of cerebral aneurysm is still not completely defined. In the present study, computational fluid dynamic (CFD) simulations of 35 ICA cerebral aneurysms were performed under pulsatile flow simulations. We aim to observe the potential links between flow instabilities and aneurysm rupture and explore whether flow instabilities could be associated with the pressure losses and high flows of the aneurysm.

6.2 Methods

6.2.1 Image-based anatomic modeling

We concentrate on the ICA sidewall cerebral aneurysms from the open Aneurisk database. All the ICA aneurysm models from the repository were reviewed for minimize selection bias. The informed consent was achieved for the use of diagnosis and clinical purpose from the involved patients. As shown in Table 1, there were 25 unruptured and 10 ICA ruptured cerebral aneurysms, with their sizes ranging from for unruptured and from for ruptured cerebral aneurysms. The two groups have similar distributions for demographics. The average age is 53.3 ± 13.3 and 60.8 ± 19.9 for the ruptured and unruptured group respectively. The aspect ratio is 1.75 ± 0.86 and 1.66 ± 0.85 for the ruptured and unruptured group respectively. The geometries of the cerebral aneurysms and vessels were extracted using the gradient-based level set segmentation algorithm from the Vascular Modeling Toolkit (VMTK) (Antigal et al. 2008). The reconstructed model was then smoothed by the Taubin filter from VMTK. We included the vessel geometry features as much as possible and extended the outlets by ten diameters to reduce boundary artifacts. Unstructured grids consisted of tetrahedral and prism elements were produced with the minimum element size of 0.025 mm and maximum element size of 0.1 mm in ANSYS ICEM 15.0. The total element numbers ranged from 8 to 16 million elements in the meshes. Three prism layers were used to solve near-wall regions.

6.2.2 Boundary conditions

At the inlets we imposed fully developed Womersley velocity profiles on the basis of a flow rate waveform achieved from (Baek et al. 2010) such as

$$V(r, t) = V_0 \left[1 - \left(\frac{r}{R} \right)^2 \right] \left\{ 1 + A \sum_{n=1}^N (a_n \cos(n\omega t) + b_n \sin(n\omega t)) \right\}$$

where the constant term V_0 represents the average velocity, A the amplitude factor ($A=1$), N the number of harmonics ($N=8$), and ω the angular frequency. The pairs of a_n and b_n normalized by constant value V_0 are $(-0.169, 0.172)$, $(-0.179, -0.083)$, $(-0.037, -0.145)$, $(0.177, 0)$, $(0.010,$

0.095), (-0.060, 0.016), (-0.047, -0.033), (0.031, -0.023). A mean flow rate of 245 ml/min was imposed at the inlet and scaled with vessel diameter based on a general law model (Valen-Stenstad et al. 2015). The Reynolds number is computed as $Re = uD/\nu$, where u denotes the mean velocity of the inlet, D the vessel's diameter, and ν the kinematic viscosity of the fluid. The Womersley number (Wo) is defined by $R\sqrt{\omega/\nu}$, where R represents the radius and ω the angular frequency. The blood density and kinematic viscosity is 1025 kg/m^3 and $3.5 \times 10^{-6} \text{ m}^2/\text{s}$, respectively. On vessel surfaces we assumed that the compliant wall-induced deformation is negligible and hereby employed the non-slip conditions. On vessel surfaces we assumed that the compliant wall-induced deformation is inessential and hereby employed the non-slip conditions.

6.2.3 Computational fluid dynamics modelling

The blood flow is assumed as an incompressible and Newtonian fluid and dominated by the three-dimensional Navier-Stokes equations.

$$\frac{\partial u_i}{\partial x_i} = 0 \quad (4-1)$$

$$\frac{\partial u_i}{\partial t} + u_j \frac{\partial u_i}{\partial x_j} = -\frac{1}{\rho} \frac{\partial P}{\partial x_i} + \nu \frac{\partial^2 u_i}{\partial x_j^2} \quad (4-2)$$

Where u_i is the velocity component in the direction x_i ($i, j = 1, 2, 3$), P the pressure. Transient flow simulations were performed using CFX 15 (ANSYS), which utilizes an element-based finite volume approach to discretize in space, and a high-resolution scheme for the stabilization of the convective term. Time discretization is achieved by the second-order backward Euler scheme. CFX employs an implicit coupled solver, in which all the hydrodynamic equations are solved as a single system. Non-linear equations are linearized, which are then solved by an Algebraic Multigrid (AMG) solver. The convergence criteria for iterative errors were set to be of 10^{-4} . A fixed time step is utilized to facilitate further data analysis. No turbulence model was applied due to the relatively low Reynolds number in this study. The simulations required approximately 38 hours of CPU time on a PC with an Intel Xeon (2.9GHz); parallel computing with a cluster by 32 nodes was carried out with Platform Computing. All the simulations were conducted up to nine cardiac cycles and the computed results of the last six cycles were employed for further data analysis.

Mesh-dependence was studied together with the time increment effect to confirm high spatial and temporal resolutions in predicting flow instability in cerebral aneurysms. Three time increments of 0.1 ms, 0.25 ms, and 0.5 ms were taken for comparison and the results with the

time step of 0.25 ms and 0.1 ms agreed reasonably each other, capable of capturing high-frequency flow instability. Furthermore, the grid refinement was investigated with a minimum mesh size of 0.03 mm, 0.025 mm, and 0.01 mm, and together with the time increment refinement. A mesh system with the minimum element size of 0.025 mm and time step = 0.25 ms was confirmed to be capable to provide sufficiently high resolution of the flow instability in the present cerebral aneurysms models and were substantially employed in all the simulations. To make sure whether the flow was correctly resolved, the spatial and temporal resolutions were assessed by computing the viscous length l^+ and time scale t^+ , such as

$$l^+ = \frac{u_* dx}{\nu}, \quad (4-3)$$

$$t^+ = \frac{u_*^2 dt}{\nu}, \quad (4-4)$$

$$u_* = \sqrt{\nu s_{ij}}, \quad s_{ij} = 0.5 \left(\frac{\partial u_i}{\partial x_j} + \frac{\partial u_j}{\partial x_i} \right), \quad (4-5)$$

6.2.4 Data analysis

Based on the computed spatiotemporal WSS distributions, OSI was further calculated to describe the oscillatory feature of the WSS vector, such as

$$OSI = 0.5 \left(1 - \frac{\left| \int_0^T \overline{WSS} dt \right|}{\int_0^T |\overline{WSS}| dt} \right) \quad (4-6)$$

where $0 < OSI < 0.5$ with a value of 0 being no variation of the WSS vector, and of 0.5 being 180° deflection of the WSS direction. The time averaged WSS was obtained such as

$$MWSS = \frac{1}{T} \left| \int_0^T |WSS| dt \right| \quad (4-7)$$

Low WSS area (LSA) was computed as the area of the aneurysm below 10% of the parent arterial WSS and then normalized by the dome area. Energy Loss indicated the energy expenditure due to the viscous resistance and vortex.

$$EL = \frac{v_{in} A [(0.5 p v_{in}^2 + P_{in}) - (0.5 p v_{out}^2 + P_{out})]}{V_m} \quad (4-8)$$

Pressure Loss Coefficient is defined by

$$PLC = \frac{(0.5pv_{in}^2 + P_{in}) - (0.5pv_{out}^2 + P_{out})}{0.5pv_{in}^2} \quad (4-9)$$

To assess the fluctuating kinetic energy (FKE) we further made decomposition of the instantaneous velocity $u_i(x, t)$ with average $\overline{u_i}(x, t)$ and fluctuating $u'_i(x, t)$ ($i = 1, 2, 3$), so that

$$u_i(x, t) = \overline{u_i}(x, t) + u'_i(x, t). \quad (4-10)$$

Thus the fluctuating kinetic energy (FKE) can be defined as,

$$FKE(x, t) = \frac{1}{2} \langle u'_i(x, t) \cdot u'_i(x, t) \rangle. \quad (4-11)$$

6.3 Results

6.3.1 Flow stabilities

Figure 6-2 demonstrates the mean WSS at aneurysm was obviously smaller than that in the arteries of both the unruptured and ruptured groups with $P < 0.05$. The mean WSS at vessel was 7.62 ± 2.54 Pa, which was 1.4 times higher than that at aneurysm (5.59 ± 3.52) for all cases. The ruptured-unruptured cerebral models shared an obvious characteristic of low WSS at aneurysm compared to the vessel region. **Figure 6-3** illustrates the distribution of the normalized MWSS for 10 ruptured and 25 unruptured aneurysms. The ruptured aneurysms R1&R7 exhibit comparable WSSs in the dome with the vessel region, while the other eight ruptured aneurysms show lower WSSs. In the unruptured group, seven aneurysms manifest high WSS while the other 18 show lower WSSs. **Figure 6-4** illustrates the volumetric rendering of energy fluctuations of the aneurysms. 12 cases exhibited fluctuating kinetic energies above $10^{-4} \text{ m}^2/\text{s}^2$ and thus were defined as unstable whereas the other cases were classified as stable. Note that the two rupture aneurysms exhibit profound fluctuation energies compared to the other aneurysms, although energy fluctuation appears in both the rupture and unruptured groups. **Figure 6-5** illustrates the time-varying velocities at feature points inside the cerebral aneurysms. It is seen that the initial transient feature in velocity rapidly damps out in the stable aneurysms, whereas the unstable aneurysms demonstrate persistent velocity fluctuations. The two cases (R1&R7) obviously exhibit more significant velocity fluctuations compared to the others. **Figure 6-6** displays the scatter plot of MWSS versus pressure loss coefficient for ruptured-unruptured aneurysms. Most of the unstable aneurysms are exposed to relatively higher PLC and MWSS, whereas the stable aneurysms were more likely to present lower PLC and MWSS.

6.3.2 Statistics results

Table 2 illustrates the statistical differences of the variables of the ruptured-unruptured aneurysms. The mean WSS at the artery are comparable: $8.1 \pm 3.3\text{Pa}$ for the ruptured and $7.4 \pm 2.2\text{ Pa}$ for the unruptured group. Significant differences were observed between ruptured and unruptured cerebral aneurysms for three parameters. The Maximum WSS at aneurysm in the ruptured group ($15.66 \pm 14.19\text{Pa}$) was clearly lower than the value in the unruptured group ($33.95 \pm 18.09\text{Pa}$). The ruptured cerebral aneurysms exhibit significantly higher ratio of low shear area ($21 \pm 25.3\%$) compared to the unruptured cerebral aneurysms (6.1 ± 16.5). The ruptured cerebral aneurysms exhibit significantly lower PLC (1.27 ± 0.57) than unruptured cerebral aneurysms (2.20 ± 1.15).

6.4 Discussion

In this study, CFD of 10 ruptured and 25 unruptured ICA aneurysms were carried out for potential associations between flow instability and aneurysm rupture. We define the aneurysms experienced significant flow instabilities as unstable and the others as stable. It is difficult to simply correlate the unstable aneurysms as ruptured since they appear in both the ruptured and unruptured cohorts. However, the two ruptured aneurysms obviously exhibits profound flow instability compared to the other aneurysms, suggesting that flow instability might be a potential source associated with the aneurysm rupture. Moreover, the statistics results illustrated that the ruptured aneurysms exhibit significantly higher ratio of low shear area, lower Maximum WSS and PLC compared to the unruptured aneurysms. The Maximum WSS tends to be low, while the area exposed to abnormal WSS is likely to be large in ruptured aneurysms. Both the flow instability and WSS-related factors could not separate the ruptured and unruptured aneurysms personally, but it is seen that the stable status with low-WSSs were more commonly seen in ruptured aneurysms, while unstable status with high-WSSs were likely to observe with unruptured aneurysms.

Our results reveal that both stable and unstable aneurysms could be associated with the risk of rupture. When the aneurysm is initialized, the aneurysm sac expansion is inclining to continuously stabilize the flow with lower WSS, making inflammation to control the rest of evolution. However, some aneurysms could be still governed by unstable flow accompanied with high WSS and pressure loss due to their geometry; As a result, their evolution and rupture could be promoted by unstable flow through the noninflammatory way. Our two ruptured aneurysms have relatively higher WSS compared with the unruptured aneurysms and present obvious low WSS at the tip or bleb with high WSS in the body of aneurysm. It is possible that both high and low WSS could cause the growth and rupture of cerebral aneurysms with

independent pathways. We guess that this local excessively low WSS may be responsible for the fragile variation of the aneurysm and lead to ultimate aneurysm rupture.

[Shojima et al. \(2004\)](#) reported that three ruptured cerebral aneurysms presented relatively higher WSS at aneurysm region than unruptured aneurysms and distinctly low WSS at the top or bleb with high WSS in the body or fundus of aneurysm. Some aneurysms are facilitated by low WSS and high OSI at growing phase, while some aneurysms could also be facilitated by remarked WSS fluctuations and high pressure losses. The flow fields associated with the ruptured aneurysms are likely highly disturbed flows, which could more damaging to the ECs than laminar flow. Local excessively low WSS values at the top or the bleb may trigger the rupture. [Valen-Sendstad et al. \(2013\)](#) reported the high-frequency flow instabilities in 12 MCA aneurysms and suggest that the flow instability may be correlated to the aneurysm rupture. [Varble et al. \(2016\)](#) in 56 MCA aneurysms and conclude that the flow instability could not differentiate ruptured from unruptured aneurysms. Significant controversy results were found from statistics of large series of cerebral aneurysms. It was not easy to distinguish between the ruptured and unruptured aneurysms with WSS-related factors since both high- and low- flow were observed in the two groups. The hemodynamic characteristics observed here are qualitatively similar with previous researches of low-flow theory.

There are several limitations to this study. Our boundary conditions are not patient specific. The effects of reflections at outlets were not considered. Although sharing the same inflow boundary conditions for the two aneurysms in one patient may help control the individual differences, the flow rate measured by MRI or Doppler Ultrasound should be obtained in future. The elastic effects on the flow instability are not considered since accurate pressure wave and wall thicknesses were not available from clinical measurement. However, the wall elasticity may to some extent influence the flow patterns in the cerebral aneurysm models ([Tada and Tarbell, 2005](#); [Lee et al., 2013](#)). Thirdly, the non-Newtonian effect may not be negligible in complex flows, although it is generally negligible in cerebral arteries in laminar flows due to its modest effect on flow patterns ([Lee and Steinman, 2007](#); [Perktold et al., 1998](#)). The elastic and non-Newtonian effects on the hemodynamic factors and flow instabilities still need further research.

6.5 Conclusion

Our simulation results demonstrated that the ruptured aneurysms present significantly higher ratio of low shear area, lower pressure loss coefficient and stable status compared to unruptured aneurysms. However, unstable statuses were also observed in two of ten ruptured aneurysms, characterized by remarked WSS fluctuations, higher pressure and energy losses. The results suggest that flow instability may be a potential source correlating to aneurysm rupture, inherently associated with high pressure loss in cerebral aneurysms.

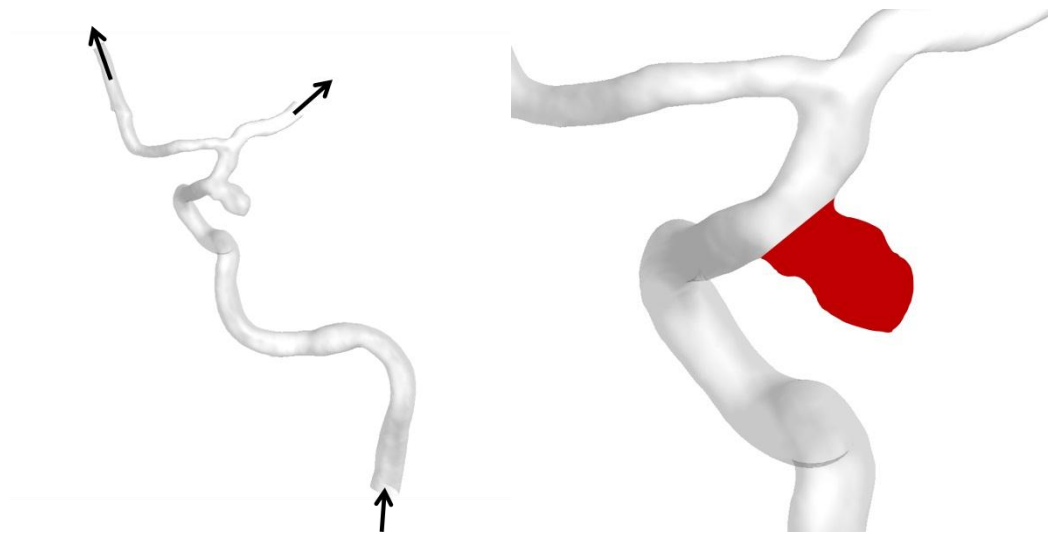


Figure 6-1. The typical patient-specific internal carotid aneurysm model. The aneurysm area is marked as red color.

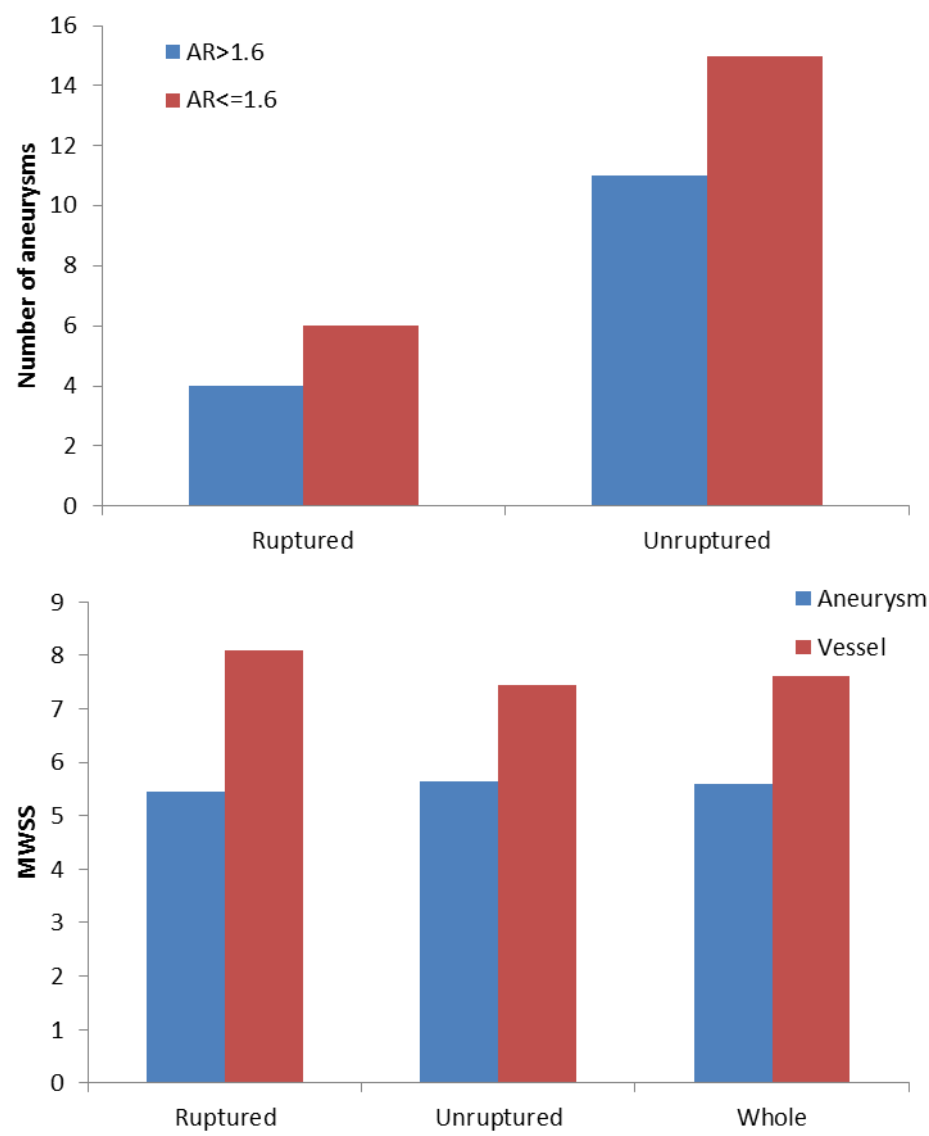


Figure 6-2. Aspect ratio distributions of aneurysms.

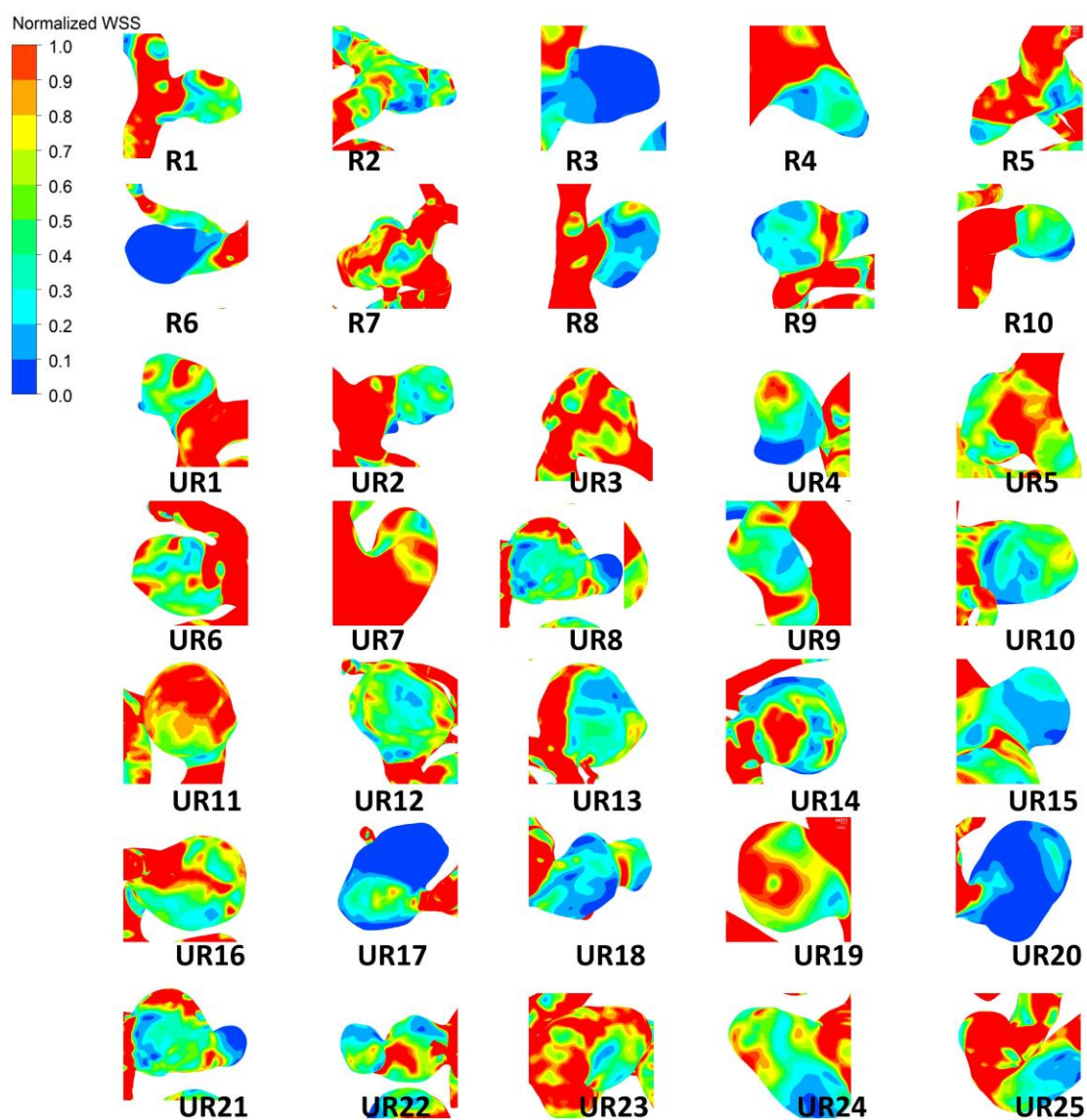


Figure 6-3. Normalized WSS distribution for ruptured-unruptured ICA aneurysms. The top two rows are ruptured aneurysms. There are no significant differences between aneurysms. Both low and high WSS are observed at the aneurysm.

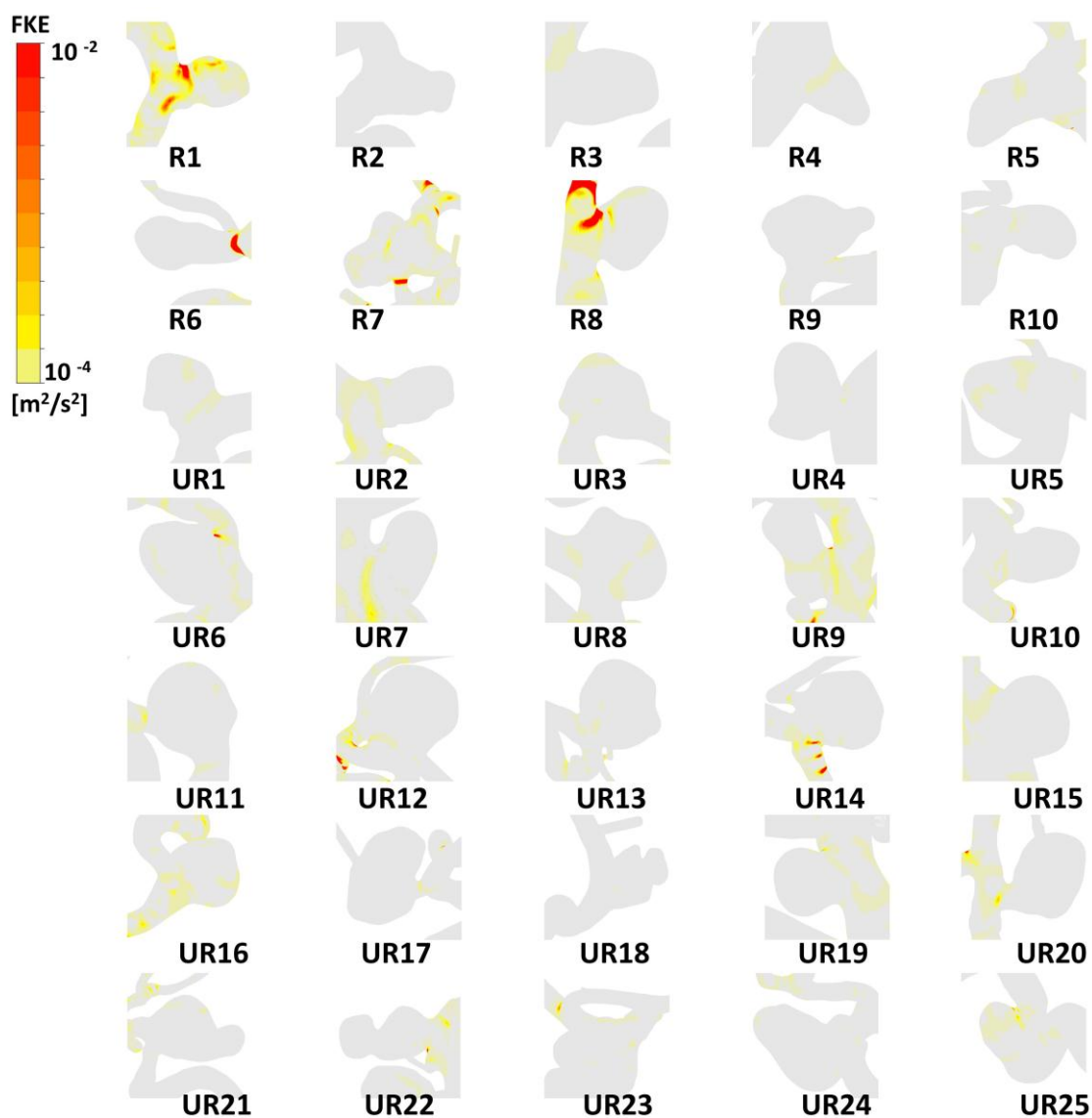


Figure 6-4. Volumetric rendering of energy fluctuations (FKE) of thirty-five ruptured-unruptured aneurysms. The cases without fluctuations appear empty.

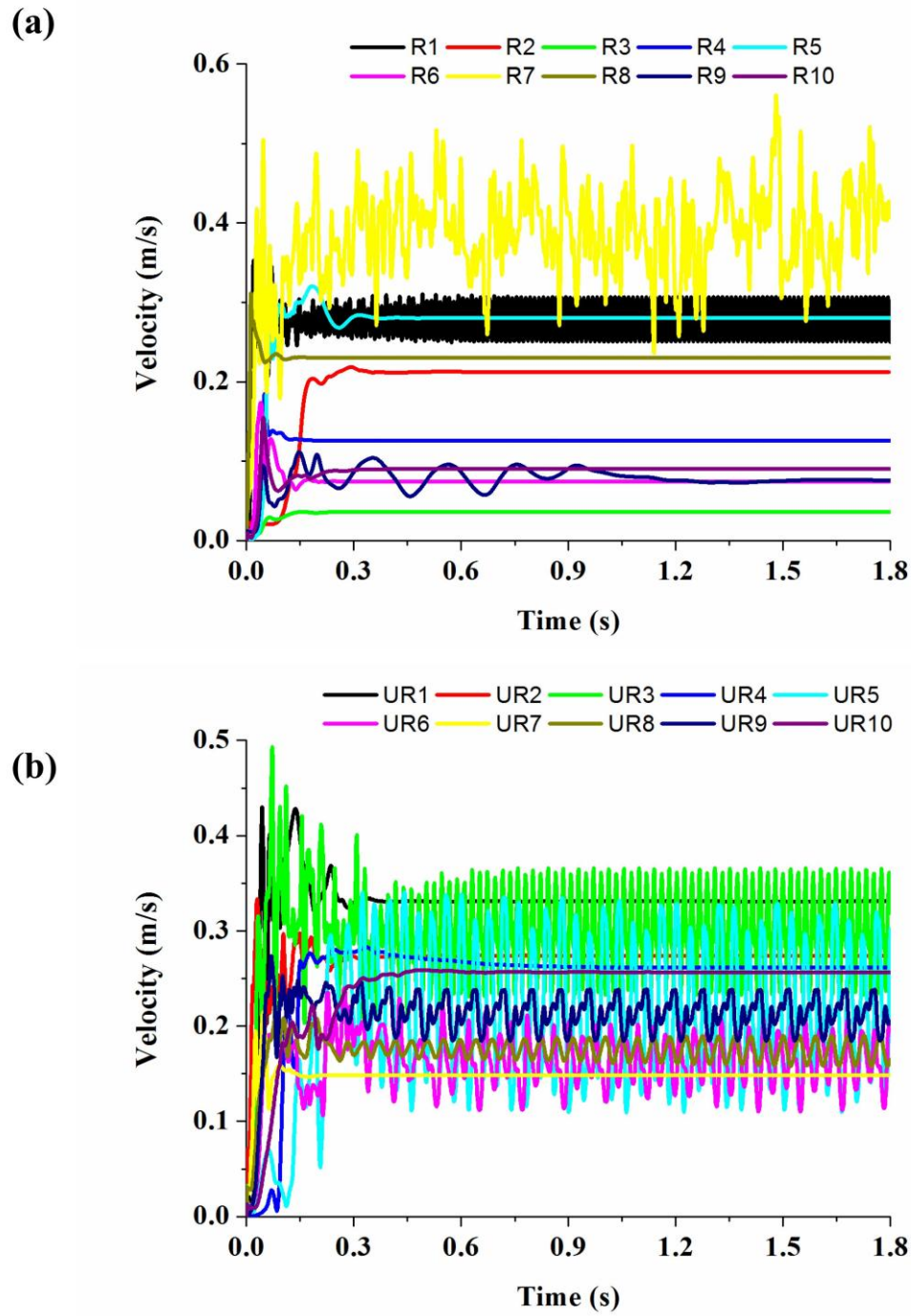


Figure 6-5. Time-varying velocities at feature points inside the ruptured (a) and unruptured (b) cerebral aneurysm models.

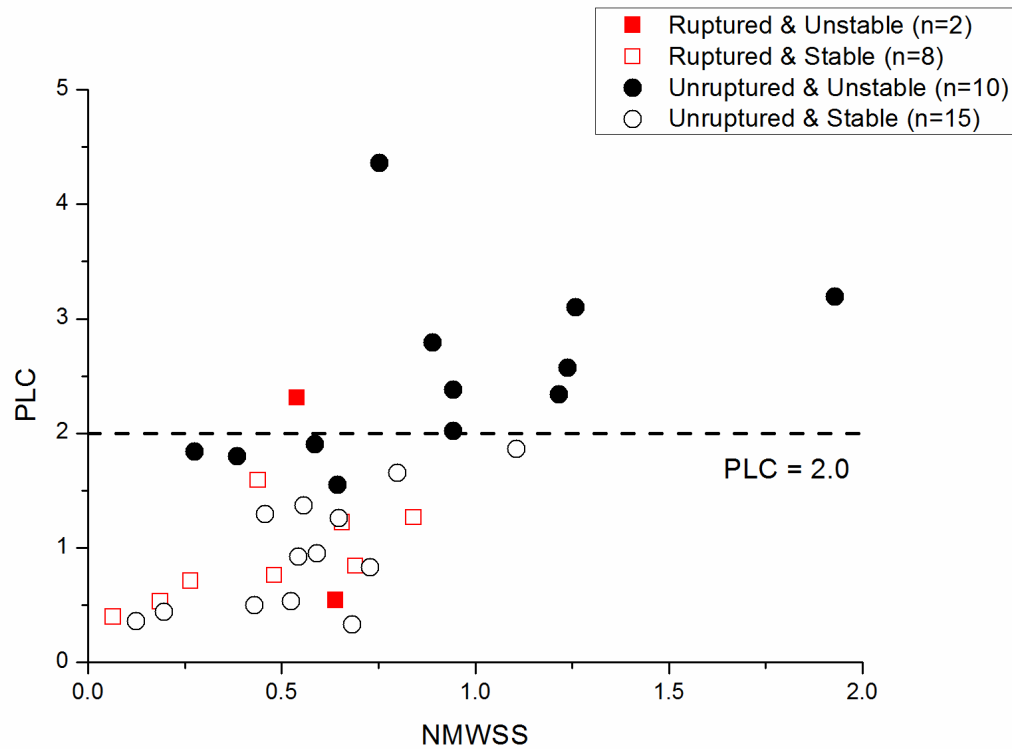


Figure 6-6. Scatter plot of Normalized Mean WSS (NMWSS) versus pressure loss coefficient (PLC) for ruptured and unruptured ICA aneurysms. The red solid open squares represent the unstable and stable ruptured aneurysms, whereas the black solid open circles represent the unstable and stable unruptured aneurysms, respectively.

	Ruptured (n=10)	Unruptured (n=25)	P Value
Age	60.8±19.9	53.3±13.3	0.2
Gender (F/M)	9/1	21/4	
Mean Parent Vessel Radius (mm)	1.76±0.3	1.91±0.2	0.1
Aspect ratio	1.75±0.86	1.66±0.85	0.80

Table 6-1. Statistics of the demographic, morphologic parameters for the thirty-five cerebral aneurysms

	Ruptured (n=10)	Unruptured (n=25)	P Value
Maximum WSS (Pa)	15.66±14.19	33.95±18.09	0.007
Minimum WSS (Pa)	0.5±0.5	0.59±0.4	0.57
Mean WSS (Pa)	5.4±5.1	5.64±2.9	0.89
NMWSS	0.61±0.37	0.78±0.52	0.35
LSA	21±25.3	6.1±16.5	0.049
Mean OSI	0.11±0.025	0.1±0.023	0.46
Maximum OSI	0.46±0.03	0.47±0.03	0.4
EL	7944±8094	4213±4425	0.08
PLC	1.27±0.57	2.20±1.15	0.02

Table 6-2. Statistics of the hemodynamic variables for the thirty-five cerebral aneurysms

7 Conclusion remarks and future works

Many researches have been carried out to study the association between hemodynamics and aneurysm rupture. However, the mechanism of cerebral aneurysms is still not completely defined. Contradictory high-WSS and low-WSS theories were proposed to explain the rupture mechanism. It is unclear whether the simplified assumptions or the complicated pathological mechanisms lead to the different results. In this study, we developed high-resolution CFD models of anatomically patient-specific cerebral aneurysms to investigate how the geometries and inlet flow rate waveforms contribute to the flow instability with an ultimate goal to unveil its correlation with aneurysm rupture mechanisms. In general, the novel contributions of this study are the following:

Flow instabilities in patient-specific cerebral aneurysms are numerically resolved with high-resolution schemes. We used a CFD model of anatomically realistic cerebral aneurysms combining with Fourier series and PSD analysis to investigate the association between inflow waveform's harmonic frequencies and flow fluctuations in terminal cerebral aneurysms. Our simulated results demonstrated that there exists a harmonic frequency dependency in inlet flow rate waveforms inherently associated with flow instabilities in cerebral aneurysms: low-frequency harmonics play a crucial role in causing significant WSS fluctuations. This is partly explained by that the low-frequency harmonics govern a primary local adverse pressure gradient at late systole during flow deceleration, which induces flow instabilities while giving it sufficient time to develop into flow instabilities whereas high-frequency harmonics do not but decay rapidly. This implies that flow fluctuations in cerebral aneurysms may be of some robustness, dependent mainly on the primary harmonic frequency initiated by heart contraction but against unpredictable high-frequency perturbations in the inflow waveforms.

In order to study the elastic wall effect on the flow instability and hemodynamic factors, we performed fluid-structure interaction on two patient-specific representative cerebral aneurysms. Both CFD simulations and PIV experiments have been carried out for more accurate prediction and validation. The results demonstrated that significant differences of hemodynamic factors and flow patterns were observed at the blebs between the rigid and elastic models. The elasticity of the aneurysm wall could dampen the change of WSS, which suggests that the rigid model may proliferate the risk of aneurysm rupture.

CFD simulations of two matched-pairs of ruptured-unruptured cerebral aneurysms were then performed to investigate the potential links between flow instability and aneurysm rupture. The four cerebral aneurysms from two patients are located in the MCA and the ACA respectively. There exists a combination of high OSI and low WSS at the bleb, with complex disturbed flow

patterns and small impingement regions of the ruptured aneurysms. Our results demonstrated a highly disturbed state of the blood flow in the ruptured aneurysms, which features rapid velocity and WSS fluctuations at late systolic when flow decelerates. The ruptured aneurysms exhibit much more significant temporal WSS fluctuations than the unruptured aneurysms of the same patient. Specifically, cycle-to-cycle fluctuations are observed when the flow turns to decelerate in the ruptured aneurysms. These observed differences between matched ruptured-unruptured cerebral aneurysms imply that it could be a comparable model to study the potential association between the flow instability and rupture mechanism.

CFD simulations of thirty-five cerebral aneurysms located at the internal carotid artery (ICA) were performed to investigate whether fluctuation kinetic energy quantifying the flow instability might be an effective indicator to evaluate aneurysm rupture, and whether pressure loss might be associated to such flow instability. The results demonstrated that eight ruptured aneurysms present significantly higher ratio of low WSS area and lower pressure loss coefficient, whereas two ruptured aneurysms manifests remarked flow fluctuations and higher pressure losses compared to unruptured aneurysms. Our results suggest that flow instability could be associated with the risk of aneurysm rupture, which is inherently correlated with the high pressure loss for cerebral aneurysms.

In numerical simulation of cerebral aneurysms, there are many issues need to be further investigated. Firstly, a more accurate and effective transition model needs be developed. Since fully developed turbulence has not been detected yet in the cerebral aneurysms, it is natural to think that the flow fields associated with the aneurysm is more likely a highly disturbed flow near a transition point. It would be beneficial to further determine at what point the flow transitions from the disturbed flow we observe here to fully transitional in future. Secondly, the boundary conditions are not patient specific. The effects of reflections at outlets were not considered. Although sharing the same inflow boundary conditions for the two aneurysms in one patient may help control the individual differences, the flow rate measured by MRI or Doppler Ultrasound should be obtained in future. In addition, wall elasticity could provide essential information towards understanding the effect of blood flow on the vascular wall. Although elastic effects have been considered in this study, we assumed a unified wall thickness. However, intra-operations have already observed that the cerebral aneurysms are exposed to different wall structures, which could to some extent influence the flow characteristics of the cerebral aneurysm. In future, the pathology and CFD simulation should be combined to unveil the onset, progress and rupture of cerebral aneurysms.

Bibliography

AneuriskWeb, “The Aneurisk Dataset Repository,” <http://ecm2.mathcs.emory.edu/aneurisk>

Antiga, L., Piccinelli, M., Botti, L., Ene-Iordache, B., Remuzzi, A. and Steinman, D. A, An image-based modeling framework for patient-specific computational hemodynamics, *Medical and Biological Engineering and Computing*, Vol.46, No.11 (2008), pp.1097–1112.

Antiga, L. and Steinman, D. A, Rethinking turbulence in blood, *Biorheology*, Vol.46, No.2 (2009), pp.77–81.

Attinger, E. O., Anné, A. and McDonald, D. A, Use of Fourier series for the analysis of biological systems, *Biophysical Journal*, Vol.6, No.3 (1966), pp.291–304.

Bazilevs, Y., Hsu, M. C., Zhang, Y., Wang, W., Kvamsdal, T., Hentschel, S. and Isaksen, J. G.. Computational vascular fluid–structure interaction: methodology and application to cerebral aneurysms. *Biomechanics and modeling in mechanobiology*, Vol.9, No.4 (2010), pp.481–498.

Baek, H., Jayaraman, M. V., Richardson, P. D. and Karniadakis, G. E. (2009). Flow instability and wall shear stress variation in intracranial aneurysms. *Journal of the Royal Society Interface*, Vol.7, No.47 (2010), pp. 967–988.

Chappell, D. C., Varner, S. E., Nerem, R. M., Medford, R. M. and Alexander, R. W, Oscillatory Shear Stress Stimulates Adhesion Molecule Expression in Cultured Human Endothelium, *Circulation Research*, Vol.82, No.5 (1998), pp. 532–539.

Crow, S. C. and Champagne, F. H, Orderly structure in jet turbulence, *Journal of Fluid Mechanics*, Vol.48, No.3 (2006), pp.547. Castro, M. A., Putman, C. M. and Cebal, J. R, Computational fluid dynamics modeling of intracranial aneurysms: effects of parent artery segmentation on intra-aneurysmal hemodynamics, *American Journal of Neuroradiology*, Vol.27, No.8 (2006), pp.1703–1709.

- Cebral, J. R., Castro, M. A., Burgess, J. E., Pergolizzi, R. S., Sheridan, M. J. and Putman, C. M, Characterization of cerebral aneurysms for assessing risk of rupture by using patient-specific computational hemodynamics models. *American Journal of Neuroradiology*, Vol.26, No.10 (2005), pp.2550–2559.
- Cebral, J. R., Mut, F., Weir, J. and Putman, C, Quantitative characterization of the hemodynamic environment in ruptured and unruptured brain aneurysms, *American Journal of Neuroradiology*, Vol.32, No.1(2011), pp.145–151.
- Davies, P. F., Remuzzitt, A., Gordon, E. J., Dewey, C. F. and Gimbrone, M. A, Turbulent fluid shear stress induces vascular endothelial cell turnover in vitro. *Proceedings of the National Academy of Sciences of the United States of America* (1986), pp.2114–2117.
- Dhar, S., Tremmel, M., Mocco, J., Kim, M., Yamamoto, J., Siddiqui, A. H. and Meng, H, Morphology parameters for intracranial aneurysm rupture risk assessment. *Neurosurgery*, Vol.63, No.2 (2008), pp.185–196.
- Dolan, J. M., Kolega, J. and Meng, H, High wall shear stress and spatial gradients in vascular pathology: a review, *Annals of Biomedical Engineering*, Vol.41, No.7 (2013), pp.1411–1427.
- Ferguson, G. G, Turbulence in human intracranial saccular aneurysms, *Journal of Neurosurgery*, Vol.33, No.5 (1970), pp.485–497.
- Ford, M. D. and Piomelli, U, Exploring high frequency temporal fluctuations in the terminal aneurysm of the basilar bifurcation, *Journal of Biomechanical Engineering*, Vol.134, No. 9 (2012).
- Frösen, J., Piippo, A., Paetau, A., Kangasniemi, M., Niemelä, M., Hernesniemi, J., Jääskeläinen, J, Remodeling of saccular cerebral artery aneurysm wall is associated with rupture histological analysis of 24 unruptured and 42 ruptured cases. *Stroke*, Vol.35, No.10 (2004): pp. 2287-2293.
- Frösen, J., Tulamo, R., Paetau, A., Laaksamo, E., Korja, M., Laakso, A., Hernesniemi, J,

- Saccular intracranial aneurysm: pathology and mechanisms. *Acta neuropathologica*, Vol.123, No.6 (2012), pp. 773-786.
- Himburg, H. A., Dowd, S. E. and Friedman, M. H, Frequency-dependent response of the vascular endothelium to pulsatile shear stress, *American Journal of Physiology. Heart and Circulatory Physiology*, Vol.293, No.1 (2007), pp.645–653.
- Jou, L. D., Lee, D. H., Morsi, H., Mawad, M. E, Wall shear stress on ruptured and unruptured intracranial aneurysms at the internal carotid artery. *American Journal of Neuroradiology*, Vol.29, No.9 (2008), pp.1761-1767.
- Jiang, J. and Strother, C, Computational fluid dynamics simulations of intracranial aneurysms at varying heart rates: a “patient-specific” study. *Journal of biomechanical engineering*, Vol.131, No.9 (2009), pp.091001.
- Khan, M. O., Valen-Sendstad, K., Biswas, D., Casey, D. M., Loth, F. and Steinman, D. A, CFD Simulation of Transition to Turbulence for Newtonian vs. Non-Newtonian Flow Through a Stenosis. SB3C2015-363.
- Kawaguchi, T., Nishimura, S., Kanamori, M., Takazawa, H., Omodaka, S., Sato, K., Nishijima, M, Distinctive flow pattern of wall shear stress and oscillatory shear index: similarity and dissimilarity in ruptured and unruptured cerebral aneurysm blebs: clinical article. *Journal of neurosurgery*, Vol.117, No.4 (2012), pp.774-780.
- Kataoka, K., Taneda, M., Asai, T., Kinoshita, A., Ito, M., Kuroda, R, Structural fragility and inflammatory response of ruptured cerebral aneurysms A comparative study between ruptured and unruptured cerebral aneurysms. *Stroke*, Vol.30, No.7 (1999), pp.1396-1401.
- Li, Y. S. J., Haga, J. H., Chien, S, Molecular basis of the effects of shear stress on vascular endothelial cells. *Journal of Biomechanics*, Vol.38 (2005), pp.1949–71.
- Lee, C. J., Zhang, Y., Takao, H., Murayama, Y. and Qian, Y, A fluid–structure interaction study

- using patient-specific ruptured and unruptured aneurysm: The effect of aneurysm morphology, hypertension and elasticity, *Journal of biomechanics*, Vol.46, No.14 (2013), pp.2402-2410.
- Lee, S. W. and Steinman, D. A, On the relative importance of rheology for image-based CFD models of the carotid bifurcation, *Journal of Biomechanical Engineering*, Vol.129, No.2 (2007), pp.273–278.
- Li, Y. S. J., Haga, J. H. and Chien, S, Molecular basis of the effects of shear stress on vascular endothelial cells, *Journal of Biomechanics*, Vol.38, No.10 (2005), pp.1949–1971.
- Liang, F., Takagi, S., Himeno, R. and Liu, H, Multi-scale modeling of the human cardiovascular system with applications to aortic valvular and arterial stenoses, *Medical & Biological Engineering & Computing*, Vol.47, No.7 (2009), pp.743–755.
- Liu, H. and Yamaguchi, T, Waveform dependence of pulsatile flow in a stenosed channel. *Journal of Biomechanical Engineering*, Vol.123, No.1 (2001), pp.88–96.
- Marzo, A., Singh, P., Reymond, P., Stergiopulos, N., Patel, U. and Hose, R, Influence of inlet boundary conditions on the local haemodynamics of intracranial aneurysms. *Computer methods in biomechanics and biomedical engineering*, Vol.12, No.4 (2009), pp.431-444.
- Meng, H., Tutino, V. M., Xiang, J. and Siddiqui, A, High WSS or Low WSS? Complex interactions of hemodynamics with intracranial aneurysm initiation, growth, and rupture: Toward a unifying hypothesis, *American Journal of Neuroradiology*. American Society of Neuroradiology, Vol.35, No.7 (2014), pp.1254-1262.
- Njemanze, P. C., Beck, O. J., Gomez, C. R. and Horenstein, S, Fourier analysis of the cerebrovascular system, *Stroke*, Vol.22, No.6 (1991), pp.721–726.
- Poelma, C., Watton, P. N. and Ventikos, Y, Transitional flow in aneurysms and the computation of haemodynamic parameters. *Journal of The Royal Society Interface*, Vol. 12, No.105 (2015), 20141394.

- Perktold, K., Peter, R., and Resch, M, Pulsatile non-Newtonian blood flow simulation through a bifurcation with an aneurysm, *Biorheology*, Vol.26, No.6 (1988), pp.1011–1030.
- Qian, Y., Takao, H., Umezu, M., Murayama, Y, Risk analysis of unruptured aneurysms using computational fluid dynamics technology: preliminary results. *American Journal of Neuroradiology*, Vol.32, No.10 (2011), pp.1948-1955.
- Sforza, D., Putman, C. and Cebal, J, Hemodynamics of Cerebral Aneurysms, *Annual Review of Fluid Mechanics*, Vol.41 (2009), pp.91–107.
- Steiger, H. J. and Reulen, H. J, Low frequency flow fluctuations in saccular aneurysms. *Acta Neurochirurgica*, Vol.83, No.3-4 (1986), pp.131–137.
- Shojima M, Oshima M, Takagi K, Torii R, Hayakawa M, Katada K, Kirino T. Magnitude and role of wall shear stress on cerebral aneurysm computational fluid dynamic study of 20 middle cerebral artery aneurysms. *Stroke*. 2004; 35(11): 2500-2505.
- Torii, R., Oshima, M., Kobayashi, T., Takagi, K. and Tezduyar, T. E, Influence of wall elasticity in patient-specific hemodynamic simulations. *Computers & Fluids*, Vol.36, No.1 (2007), pp. 160-168.
- Takao, H., Murayama, Y., Otsuka, S., Qian, Y., Mohamed, A., Masuda, S. and Abe, T, Hemodynamic differences between unruptured and ruptured intracranial aneurysms during observation, *Stroke; a Journal of Cerebral Circulation*, Vol.43, No.5 (2012), pp.1436–1439.
- Tada, S. and Tarbell, J. M, A computational study of flow in a compliant carotid bifurcation—stress phase angle correlation with shear stress, *Annals of biomedical engineering*, Vol.33, No.9(2005), pp.1202-1212.
- Valen-Sendstad, K., Mardal, K. A., Mortensen, M., Reif, B. A. P. and Langtangen, H. P, Direct numerical simulation of transitional flow in a patient-specific intracranial aneurysm, *Journal of Biomechanics*, Vol.44, No.16 (2011), pp.2826–2832.

- Valen-Sendstad, K., Mardal, K. A. and Steinman, D. A, High-resolution CFD detects high-frequency velocity fluctuations in bifurcation, but not sidewall, aneurysms, *Journal of Biomechanics*, Vol.46, No.2 (2013), pp.402–407.
- Valen-Sendstad, K., Piccinelli, M., KrishnankuttyRema, R. and Steinman, D. A, Estimation of Inlet Flow Rates for Image-Based Aneurysm CFD Models: Where and How to Begin? *Annals of Biomedical Engineering*, Vol.43, No.6 (2015), pp.1422-1431.
- Valen-Sendstad, K., Piccinelli, M. and Steinman, D. A, High-resolution computational fluid dynamics detects flow instabilities in the carotid siphon: Implications for aneurysm initiation and rupture? *Journal of Biomechanics*, Vol.47, No.12 (2014), pp.3210–3216.
- Varble N, Xiang J, Lin N, Levy E, Meng H. Flow Instability Detected by High-Resolution Computational Fluid Dynamics in Fifty-Six Middle Cerebral Artery Aneurysms. *Journal of biomechanical engineering*, Vol. 138, No.6 (2016): 061009.
- Xiang, J., Natarajan, S. K., Tremmel, M., Ma, D., Mocco, J., Hopkins, L. N. and Meng, H, Hemodynamic-morphologic discriminants for intracranial aneurysm rupture, *Stroke; a Journal of Cerebral Circulation*, Vol.42, No.1 (2011), pp.144–152.
- Xiang, J., Siddiqui, A. H. and Meng, H, The effect of inlet waveforms on computational hemodynamics of patient-specific intracranial aneurysms. *Journal of biomechanics*, Vol.47, No.16 (2014), pp.3882-3890.
- Xu, L., Saito, A., Yokoyama, Y., Sato, K., Sasaki, T., Yamaguchi, R., Sugawara. M. and Liu, H, Low-frequency harmonics in inlet flow rate play a crucial role in inducing flow instabilities in terminal cerebral aneurysms, *Journal of Biomechanical Science and Engineering*, April, 2016
- Xu, L., Sugawara, M., Tanaka, G., Ohta, M., Liu, H. and Yamaguchi, R, Effect of elasticity on wall shear stress inside cerebral aneurysm at anterior cerebral artery. *Technology and Health*

Care, Vol.24, No.3 (2016), pp.349-357.

Yagi, T., Sato, A., Shinke, M., Takahashi, S., Tobe, Y., Takao, H. and Umezu, M, Experimental insights into flow impingement in cerebral aneurysm by stereoscopic particle image velocimetry: transition from a laminar regime, *Journal of the Royal Society Interface* , Vol.10, No.82 (2013).

Zeng, D., Ding, Z., Friedman, M. H., & Ethier, C. R, Effects of cardiac motion on right coronary artery hemodynamics. *Annals of biomedical engineering*, Vol.31, No.4 (2003), pp.420-429.

Zhao, S. Z., Xu, X. Y., Hughes, A. D., Thom, S. A., Stanton, A. V., Ariff, B., & Long, Q, Blood flow and vessel mechanics in a physiologically realistic model of a human carotid arterial bifurcation, *Journal of biomechanics*, Vol.33, No.8 (2000), pp.975-984.